

UNIVERSITY OF OKLAHOMA

GRADUATE COLLEGE

THERMAL TRANSPORT IN POLYMERS, POLYMER NANOCOMPOSITES AND
SEMICONDUCTORS USING MOLECULAR DYNAMICS SIMULATION AND FIRST
PRINCIPLES STUDY

A DISSERTATION

SUBMITTED TO THE GRADUATE FACULTY

in partial fulfillment of the requirements for the

Degree of

DOCTOR OF PHILOSOPHY

By

RAJMOHAN MUTHAIAH

Norman, Oklahoma

2021

THERMAL TRANSPORT IN POLYMERS, POLYMER NANOCOMPOSITES AND
SEMICONDUCTORS USING MOLECULAR DYNAMICS SIMULATION AND FIRST
PRINCIPLES STUDY

A DISSERTATION APPROVED FOR THE SCHOOL OF AEROSPACE AND
MECHANICAL ENGINEERING

BY THE COMMITTEE CONSISTING OF

Dr. Jivtesh Garg, Chair

Dr. Wilson Merchan-Merchan

Dr. Yingtao Liu

Dr. Hamidreza Shabgard

Dr. Liangliang Huang

© Copyright RAJMOHAN MUTHAIAH 2021
All Rights Reserved.

Acknowledgements

I sincerely thank and express my deep sense of gratitude to my academic advisor and committee chair Dr. Jivtesh Garg for his continuous support, motivation and remarkable guidance throughout my PhD program. He always believed in my potential and open for discussion in all of my research projects which brought the best out of me in my academic and research life. I am indebted to his patience while correcting my writing samples and reports and support in getting various awards from Gallogly College of Engineering and School of Aerospace and Mechanical Engineering. I thank Dr. Jivtesh Garg for sharing his professional and personal life experiences with me that would enable me taking wiser decisions at various stages of my life.

I thank my dissertation committee members Dr. Wilson Merchan-Merchan, Dr. Yingtao Liu, Dr. Hamidreza Shabgard and Dr. Liangliang Huang for their belief in my ability to do an independent dissertation work. I value their commitment, time and constructive comments throughout my PhD program that improved the quality of my work. I would also like to dedicate a special mention to Professor Farrokh Mistree for pushing me in improving my leadership skills and providing opportunities to showcase my leadership skills by actively participating in Graduate Student Community services. I am also indebted for his guidance in my personal life and support without any time constraints.

I extend my humble regards to the School of Aerospace and Mechanical Engineering (AME) at the University of Oklahoma for providing me financial assistance in the form of graduate teaching and research assistantships, travel support for conferences and awarded me with Jim Bee Close Engineering scholarship and Dolese teaching fellowship. These scholarships from AME helped me to concentrate on my research work without having to think much about my financial burdens and inspired me to progress with additional momentum. I also thank Gallogly College of

Engineering for assistance and felicitating me with awards such as pursue of excellence award, Merlgar dissertation fellowship and Dissertation excellence fellowship for my research accomplishment.

I thank Dr. Lucas Lindsay (Material Scientist at Oak Ridge National Lab), Dr. Tribhuwan Pandey (Postdoc at University of Antwerp) and Dr. Carlos Polanco (Postdoc at Oak Ridge National Lab) for their support during my internship at Oak Ridge National Lab during summer 2019. I also thank Fatema Tarannum for her support and discussions on writing manuscripts and valuable inputs during my presentation.

I thank various student associations such as AME - Graduate student community (GSC) and Indian Student Association. I also thank my past and present roommates for making my life in Norman pleasant. I feel indebted for their love and support that always helped me overcoming my challenges.

I could not find words to express my deep sense of gratitude to my parents (Muthaiah Kamatchi and Easwari Muthaiah), brother (Nagaraj Muthaiah) and wife (Jeyashree Venkateshkumar) for their unconditional love and sacrifices to provide me the best in my life. I thank my sister (Murugalakshmi Vairusamy) and maternal uncle (Vairusamy Surulivel) who has always been a mental and moral support throughout my life. A special mention to my daughter (Ivanshika Jeyaraj) who born in the middle of my PhD program and COVID-19 pandemic. Finally, I dedicate this dissertation to my family, relatives, friends and well-wishers who always strive for a pleasant smile on my face.

Thank you!

Abstract

Thermal conductivity(k) is an important property of a material which is critical for applications in thermal management applications as well as thermoelectric energy conversion devices. In this work, we study the thermal transport in various materials such as polymers, polymer nanocomposites and semiconductors with different applications. Thermal conductivity (k) of polymers is significantly lower than metals. As an example, k of bulk polyethylene is $\sim 0.5 \text{ Wm}^{-1}\text{K}^{-1}$ while k of aluminum is $200 \text{ Wm}^{-1}\text{K}^{-1}$. This limits their applications in thermal management systems. Polymers, however, offer many potential advantages such as low cost, low weight, corrosion resistance and ease of processability which makes them attractive for heat transfer applications. Enhancement in thermal conductivity of polymers would enable materials to replace metals in heat transfer applications, allowing these unique advantages to be realized in commercial thermal management technologies. Similarly, accurate understanding of thermal conduction in semiconductor materials is of vital importance for designing thermal management solutions for electronics systems. The goals of this work are to enhance k of polymers through– a) alignment of polymer lamellae and embedded graphene nanoplatelets. It has been reported that, an almost 30-fold increase in thermal conductivity of aligned polyethylene was achieved demonstrating the large potential of alignment effects. Our group also achieved a 12-fold increase in thermal conductivity of simultaneously aligned polymer lamellae and graphene nanoplatelets (GnPs), and b) enhancement of interface thermal conductance between polymer and graphene through the novel effect of edge-bonding. Recently edge-bonding was shown to nearly 2-fold enable superior interface thermal conductance relative to basal-plane bonding. These effects will be studied using molecular dynamics (MD) simulations. C) thermal conductivity modulation (both increase and decrease) of semiconductors through biaxial strain for applications in thermal management and

thermoelectric energy conversion d) semiconductor materials with ultra-high thermal conductivity e) 2D semiconductors. We employed density functional perturbation theory (DFPT) coupled with exact solution of phonon Boltzmann transport equation (PBTE) for predicting the k of semiconductors.

Keywords: Thermal conductivity, Polymers, Polymer composites, Molecular Dynamics Simulation, semiconductors, first-principles computations, density-functional theory

CONTENTS

1. Introduction	1
2. Thermal conductivity enhancement in aligned polyethylene- Molecular dynamics simulation	7
2.1 Methods – Molecular dynamics simulation	8
2.2 Results	10
2.2.1 Thermal conductivity with strain	10
2.2.2 Temperature dependence thermal conductivity with strain	11
2.2.3 Role of disorder and anharmonicity	11
2.3 Conclusions	15
3. Superior effect on edge relative to basal plane functionalization of graphene in enhancing polymer-graphene nanocomposite thermal conductivity	17
3.1 Methods	18
3.1.1 Molecular dynamics simulation	19
3.2 Results	19
3.2.1 Overall composite comparison	19
3.2.2 Effect of number of sheets on interface conductance	21
3.2.3 Single Nanoplatelet	22
3.2.4 Power density spectrum	23
3.2.5 Thermal conductivity of individual graphene sheets	23
3.3 Conclusions	25
4. Biaxial strain induced thermal conductivity enhancement in boron phosphide (BP)- A first principles study	26
4.1 Density functional theory	27
4.2 Computational methods	28
4.3 Results	29
4.3.1 Phonon dispersion and density of states	30
4.3.2 Lattice thermal conductivity	30
4.4 Conclusions	36
5. Strain tuned thermal conductivity reduction in indium arsenide – A first principles	

study	37
5.1 Computational methods	38
5.2 Results	39
5.2.1 Phonon dispersion	39
5.2.2 Lattice thermal conductivity	39
5.3 Conclusions	41
6. Strain tuned low thermal conductivity in indium antimonide through increase in anharmonic scattering – A first principles study	43
6.1 Computational details	44
6.2 Results	45
6.2.1 Lattice parameter and thermal conductivity	45
6.2.2 Increase in LA phonon scattering	46
6.2.3 Increase in TA phonon scattering	49
6.3 Conclusions	50
7. First principles investigation of ultra-high thermal conductivity in hexagonal germanium carbide	51
7.1 Computational details	52
7.2 Results	53
7.2.1 Phonon dispersion and elastic constants	53
7.2.2 Lattice thermal conductivity	54
7.3 Results	56
8. Ultrahigh thermal conductivity in hexagonal BC ₆ N- An efficient material for nanoscale thermal management- A first principles study	57
8.1 Computational details	57
8.2 Results	59
8.2.1 Phonon dispersion and lattice constants	59
8.2.2 Lattice thermal conductivity	60
8.3 Conclusions	62
9. Ultrahard BC ₅ – An efficient nanoscale heat conductor through dominant contribution of optical phonons	63
9.1 Computational details	63

9.2 Results	64
9.2.1 Lattice thermal conductivity	64
9.3 Conclusions	70
10. Thermal conductivity of <i>h</i> -BC2P – A first principles study	72
10.1 Computational details	73
10.2 Results	74
10.2.1 Phonon dispersion and lattice constants	74
10.2.2 Lattice thermal conductivity	75
10.3 Conclusions	76
11. Thermal conductivity of magnesium selenide (MgSe)- A first principles study	77
11.1 Computational details	78
1.2 Results	79
11.2.1 Phonon dispersion and Lattice constants	79
11.2.2 Lattice thermal conductivity	80
11.3 Conclusions	85
12. Thermal conductivity of magnesium Telluride (MgTe)- A first principles study	86
12.1 Computational details	87
12.2 Results	88
12.2.1 Phonon dispersion and Lattice constants	89
12.2.2 Lattice thermal conductivity	89
12.3 Conclusions	92
13. Equi-biaxial strain tuned high thermal conductivity in monolayer germanium carbide(2D-GeC) - A first principles study	93
13.1 Computational details	94
13.2 Results	95
13.2.1 Phonon dispersion and density of states	95
13.2.2 Lattice thermal conductivity	97
13.3 Conclusions	100

LIST OF FIGURES

1.1 a) Randomly oriented polymer b) Aligned polymer	2
1.2 a) Randomly oriented amorphous polyethylene b) Aligned polyethylene	2
1.3 Inplane and through plane thermal conductivity of graphene nanoplatelets (GnPs)	3
2.1 Structure preparation of amorphous polyethylene and its alignment through applications of strain	8
2.2 Temperature profile from NEMD simulations	9
2.3 Variation of thermal conductivity of amorphous polyethylene with temperature at different strains	10
2.4 Increase in orientation parameter with strain at different temperature	10
2.5 Dihedral energy for original COMPASS potential and for modified dihedral parameters	12
2.6 Distribution of dihedral angles for modified and original dihedral parameters for strains of a) 400% and b) 100%	13
2.7 Temperature dependence thermal conductivity of amorphous polyethylene with modified and original dihedral parameters for strains of 100% and 400%.	14
3.1 a) EFGNP c) BFGNP b and d) Temperature profiles in PE/EFGNP and PE/BFGNP nanocomposites respectively, e) Energy transferred as a function of time for edge and basal plane f) Heat flux ratio for different nanoplatelet thickness	19
3.2 a-g). Vibrational power spectra across different layers in EFGNP and BFGNP	20
3.3 Temperature dependence thermal conductivity of pristine, edge functionalized and basal plane functionalized graphene at a) 20 nm b) 30 nm c) 40nm	22
3.4 Temperature distribution along the simulation box in pristine, edge and basal plane functionalized graphene	22
3.5 a) and b) Relaxed atomic configurations for edge and basal plane functionalization	22
3.6 a) Heat flux b) overall phonon transmission c) in-plane phonon transmission d) out-of-plane phonon transmission e) interface thermal conductance and f) relaxed structures of single sheet edge and basal plane functionalization	24
4.1 a) Cubic Boron phosphide crystal structure with lattice constant as 8.44 Å. b) Boron	

Phosphide after 4% compression in x and y direction and relaxed in z direction.	27
4.2 Phonon dispersion and density of states for the 0 %, 2 % and 4% strained BP	28
4.3 In-plane thermal conductivity of 0%, 2% and 4% strained boron phosphide using SMA relaxation method and iterative exact solution method	29
4.4 In-plane thermal conductivity of 0%, 2% and 4% strained boron phosphide using SMA relaxation method and iterative exact solution method	30
4.5 Phonon linewidth with strain at different temperature and phonon group velocity of TA and LA phonons	32
4.6 Dominant scattering mechanisms in boron phosphide of LA phonon mode b) TA phonon mode modes for different strain rate along Γ -X direction. c and d): Total scattering rate due to all possible scattering for LA and TA phonon mode respectively for different strain rate. e): Scattering due to $a + a \rightarrow o$ for LA phonon modes for different strain rates. f) Scattering due to $a + a \rightarrow o$ for TA_1 phonon modes with different strain rate	33
4.7 a) Spectral dependence of thermal conductivity in strained Boron Phosphide at 300 K b) b) Phonon mean freepath of BP with strain	34
5.1 Indium Arsenide with a) 0% and b) 3% strain c) Phonon dispersion and density of states for unstrained and 3% biaxially compressed InAs.	37
5.2 a) In-plane and out-of-plane thermal conductivity of 0%, 3% biaxially compressed InAs b) TA, LA and optical phonon mode contribution to overall thermal conductivity	38
5.3 a) Phonon linewidth (inverse of lifetime) and b) average phonon group velocity of InAs with 0% and 3% strain	40
5.4 a) and b) Total scattering rate of TA and LA phonon modes, respectively, c) and d) dominant scattering channels of TA and LA phonon modes, respectively, e) and f) scattering of TA phonon modes due to $a+a \rightarrow a$ and $a+ a \rightarrow o$, respectively, g) and h) scattering of LA phonons due to $a \rightarrow a+a$ and $a+a \rightarrow o$ respectively for the 0% and 3% biaxial compressive strained InAs	41
6.1 Indium Antimonide with a)0% and b) 5% strain c) Phonon dispersion and density of state for unstrained and biaxial compressive strained InSb	43
6.2 Computed in-plane and out-of-plane thermal conductivity of unstrained and 5% biaxially compressed InSb	44

6.3 Comparison between unstrained and strained InSb of a) Phonon linewidths at 300 K b) mean velocity in in-plane x -direction and c) mean velocity in out-of-plane z -direction	44
6.4 Comparison of unstrained and strained InSb in terms of total scattering rate at 300 K along Γ -X of a) LA and b) TA phonon modes. Contribution of dominant scattering channels at 300 K in unstrained InSb for c) LA and d) TA phonons. Comparison between unstrained and strained InSb of e) $a_{LA} \rightarrow a + a$ channel, f) $a_{TA} + a \rightarrow a$ channel and g) $a_{TA} + o \rightarrow o$ channel at 300 K	45
6.5 Phase space for scattering of LA phonons in strained and unstrained InSb b) phase space for scattering of LA at different frequencies and c) Comparison of three-phonon coupling elements in strained and unstrained InSb	46
7.1 Atomic structure of 2H-GeC	51
7.2 Phonon dispersion and phonon density of state for the 2H-GeC with lattice constants $a=3.188 \text{ \AA}$ and $c/a=1.646$	52
7.3 Temperature dependent lattice thermal conductivity of the isotopically pure and natural 2H-GeC along a and c axis. 3b) Length dependent lattice thermal conductivity of 2H-GeC along a and c axis	53
7.4 Phonon group velocity and b) phonon linewidth (inverse of lifetime) for a hexagonal germanium carbide(2H-GeC)	54
7.5 Thermal conductivity contribution from TA_1 , TA_2 , LA and optical phonon modes	54
7.6 Phonon meanfreepaths(nm) of TA_1 , TA_2 , LA and acoustic phonon modes for 2H-GeC at room temperature	55
8.1 h -BC ₆ N crystal structure with lattice parameters $a= 2.4802 \text{ \AA}$ and $c/a=3.3438$	57
8.2 Phonon dispersion and phonon density of states for the hexagonal BC ₆ N with lattice constants $a= 2.4802 \text{ \AA}$ and $c/a=3.3438$	58
8.3 Temperature dependent lattice thermal conductivity along a and c axis for pure and naturally occurring h -BC ₆ N. b) Room temperature size dependence thermal conductivity of pure h -BC ₆ N	59
8.4 Phonon group velocity of TA_1 , TA_2 , LA and Optical phonon modes of h -BC ₆ N	60
8.5 Phonon linewidths of TA_1 , TA_2 , LA and optical phonons for h -BC ₆ N	60
8.6 Phonon mean free path of TA_1 , TA_2 , LA and Optical phonons for h -BC ₆ N	61
9.1 Atomic arrangements of BC ₅ with space group P3m1	63

9.2 Thermal conductivity of BC ₅ along a-axis and c-axis at different temperatures	
b) Length dependence of thermal conductivity (300 K) of BC ₅ between 10 nm and 10000 nm	64
9.3 Phonon dispersion along the high symmetry points of tetragonal BC ₅ and phonon density of states	65
9.4 Phonon meanfreepath dependence thermal conductivity of BC ₅ and Silicon	66
9.5 Spectral distribution of k with frequency at 100 K, 300 K and 500 K. b and c) Percentage contribution by transverse acoustic (TA ₁ and TA ₂), longitudinal acoustic (LA) and optical phonon modes	66
9.6 Phonon linewidths of transverse acoustic, longitudinal acoustic and optical phonon modes at a) 100 K b) 300 K c) 500 K. d) Phonon group velocity of all phonon modes	67
9.7 a) Scattering Phase space and b) Bose-Einstein population of phonons in BC ₅	68
9.8 Phonon meanfreepaths in BC ₅ at a) 100 K b) 300 K and 500 K	69
9.9 Phonon linewidths of BC ₅ and Diamond	70
10.1 a) Atomic arrangements of h -BC ₂ P with 3 x 3 x 3 supercell with lattice constants $a=5.2686$ bohr and $c/a=1.686$ b) front view c) top view d) side view	72
10.2 Phonon dispersion curve and phonon density of states for the h -BC ₂ P	73
10.3 Temperature dependence and b) Length dependence of thermal conductivity along and perpendicular to c-axis of h -BC ₂ P	74
10.4 Phonon group velocity and b) phonon linewidth of TA, LA and optical phonon modes of h -BC ₂ P at 300 K	75
11.1 Crystal structure of MgSe with crystalline phases; NiAs ($a=7.216$ bohr, $c/a=1.6672$), wurtzite ($a=7.924$ bohr, $c/a=1.6149$), rocksalt ($a=10.2617$ bohr) and zinblende ($a=11.16$ bohr) respectively	77
11.2 Phonon dispersion and phonon density of states (PDOS) of MgSe with crystalline phase; a) zinblende b) wurtzite c) rocksalt and d) nickel arsenic	78
11.3 Temperature dependent lattice thermal conductivity of MgSe with different crystalline phase with a) iterative solution of BTE c) Length dependent thermal conductivity of MgSe at room temperature(300K)	80
11.4 a) and b) Temperature and length dependent (300 K) thermal conductivity of	

natural MgSe with isotopic scattering for different crystalline phase	81
11.5 Mode contribution thermal conductivity of MgSe at 300K for different crystalline phase	81
11.6 Phonon group velocity and scattering of MgSe with crystalline phase; a) zinblende b) wurtzite c) rocksalt and d) nickel arsenic	82
11.7 Phonon scattering of MgSe with crystalline phase; a) zinblende b) wurtzite c) rocksalt and d) nickel arsenic	83
12.1 a-d): Crystal structure of MgTe with crystalline phases; NiAs (a=7.8585 bohr, c/a=1.6281), wurtzite (a=8.5287 bohr, c/a=1.6286), rocksalt (a=11.0985 bohr) and zinblende (a=12.073 bohr) respectively	86
12.2 Phonon dispersion and phonon density of states for the MgTe with crystal phase a) nickel arsenic b) rocksalt c) wurtzite and d) zinblende	87
12.3 a) Temperature dependent lattice thermal conductivity by solving the PBTE iteratively b) at single mode relaxation time approximation (SMA) c) Length dependence thermal conductivity at room temperature (300 K) for MgTe with different crystalline phase	88
12.4 Thermal conductivity contribution from TA_1 , TA_2 , LA and optical phonon modes of MgTe with different crystalline phase along different directions	89
12.5 Spectral distributions of thermal conductivity in MgTe with different crystalline phase	90
12.6 Phonon group velocity of MgTe with crystalline phase a) nickel arsenic (NiAs) b) rocksalt (RS) b) wurtzite (WZ) d) zinblende (ZB) at 300K	90
12.7 Phonon linewidth of MgTe with crystalline phase a) nickel arsenic (NiAs) b) rocksalt (RS) b) wurtzite (WZ) d) zinblende (ZB) at 300K	91
13.1 Atomic configuration of monolayer germanium carbide	94
13.2 Phonon dispersion and phonon density of states for the monolayer germanium carbide with strain between 0% and 8%	95
13.3 Elastic constants of monolayer germanium carbide with strain	96
13.4 a and b) Temperature dependent lattice thermal conductivity along arm-chair and zig-zag direction with strain for a pure monolayer germanium carbide c) Lattice thermal conductivity of monolayer germanium carbide with strain	97

13.5 Lattice thermal conductivity of monolayer germanium carbide(2D-GeC) with isotopic scattering for strain between 0% and 8%	98
13.6 Phonon group velocity of monolayer germanium carbide with strain	98
13.7 Phonon linewidth of monolayer germanium carbide with strain	99
13.8 Phonon bandgap for a monolayer germanium carbide with strain	100

LIST OF TABLES

7.1 Elastic constants of 2H-GeC	53
8.1 Elastic constants (in GPa) of <i>h</i> -BC ₆ N, <i>h</i> -Diamond and <i>h</i> -BC ₂ N	59
9.1 Elastic constants of BC ₅ , Silicon and Diamond	65
11.1 Lattice constants, Bulk modulus(B), Youngs modulus(E), Shear modulus(G) and poisson's(ν) ratio of MgSe with different crystal phase	80
12.1 Lattice constants, Bulk modulus(B), Youngs modulus(E), Shear modulus(G) and poisson's(ν) ratio of MgTe with different crystal phase	89
13.1 Elastic constants, Young's modulus, Shear modulus and phonon bandgap with equibiaxial tensile strain for 2D-GeC	96

CHAPTER 1: INTRODUCTION

Thermal management has become a challenging problem in modern electronics industry since electronic devices have become more integrated, functionalized and miniaturized^{1, 2}. If the heat cannot be dissipated efficiently, the lifetime, efficiency and reliability of the system can be reduced. Materials with high thermal conductivity are urgently needed to dissipate generated heat. Moreover, at nanometer length scales, Fourier law of heat conduction breaks down, decreasing effective thermal conductivity below bulk value, exacerbating heat dissipation in the process. The effect has been shown to lead to overheating, reducing reliability and performance in nanoelectronics applications. To improve thermal management at nanoscale, there is a strong need for materials with high nanoscale thermal conductivity. Thermoelectric devices with higher energy conversion efficiency, on the other hand, require materials with ultra-low thermal conductivity. This research work investigates a) enhancement of thermal conductivity in polymers and polymer nanocomposites, b) thermal conductivity enhancement in semiconductors, and c) ultralow thermal conductivity semiconductors for thermoelectric applications. Molecular dynamics simulations utilizing LAMMPS (Large Scale Atomic/Molecular Massively Parallel Simulator) are used to investigate polymers and polymer nanocomposites and first principles calculations are used for semiconductors.

Thermal conductivity is a basic material property and is a measure of the ease with which heat is transmitted through a material. For steady and one-dimensional flow, the heat conduction according to Fourier law³ is given by

$$Q = -kA \frac{dT}{dx} \quad (1.1)$$

where Q is the rate of heat transfer (W), k is thermal conductivity ($\text{Wm}^{-1}\text{K}^{-1}$), A is cross sectional heat transfer area (m^2), dT = Temperature difference ($^{\circ}\text{C}$) and dx = conduction path length (m). Materials with high thermal conductivity are called conductors. Metals having a thermal conductivity in the range of 20 to 400 $\text{Wm}^{-1}\text{K}^{-1}$ are treated as conductors. Materials with low conductivity are called insulators. Polymers and glasses have thermal conductivity in the range of 0.1 – 0.5 $\text{Wm}^{-1}\text{K}^{-1}$ and are therefore considered as insulators. The heat transfer mechanism is dominated by different carriers in different materials. For examples, in solids the heat is transported by either electrons and holes (charge carriers) or by phonons (atomic lattice vibrations). In metals the heat transfer by electron dominates while in insulators and semiconductors the heat transfer is dominated by phonons.

The first goal of this study is to study thermal conductivity in aligned polymers using MD simulations and is discussed in chapter 2. Polymers offer several advantages over metals such as low cost, corrosion resistance, easy of moldability, lower weight and are widely used in thermal management applications such as automotive control units⁴, batteries⁵, electronic packaging⁶, solar panels⁷,

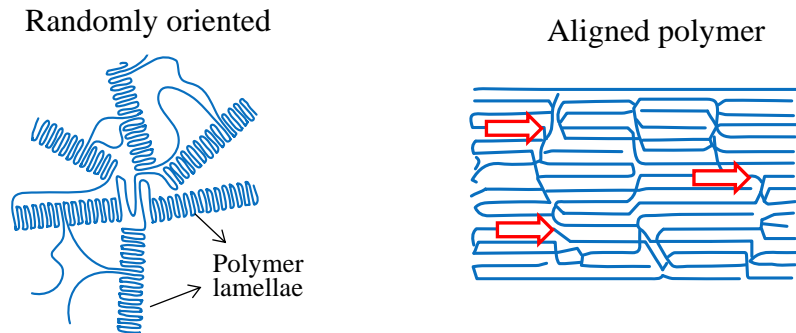


Figure 1.1(a). Randomly Oriented polymer 1b). Aligned polymer

solar water heating⁸ and water desalinations⁹. Polymers are comprised of ordered crystalline regions called lamellae¹⁰. Thermal conductivity along these lamellae can be very high, even exceeding that of metals. Random orientation of lamellae however, leads to overall poor thermal conductivity of the polymer matrix. Aligning these lamellae (Fig. 1) through techniques¹¹ such as mechanical stretching can enhance thermal conductivity by two orders of magnitude. To achieve this, structures of amorphous polymers were created (Figure 1.2a) and subjected to strain to align polymer lamellae (Figure 1.2b) using Molecular Dynamics (MD). Molecular dynamics (MD) simulations are used to study the thermal conductivity. MD involves simulating the motion of atoms in a molecular system based on knowledge of interatomic forces and use of Newtonian dynamics¹². Initial structure of a single polymer chain will be modeled using Nanoengineering-1

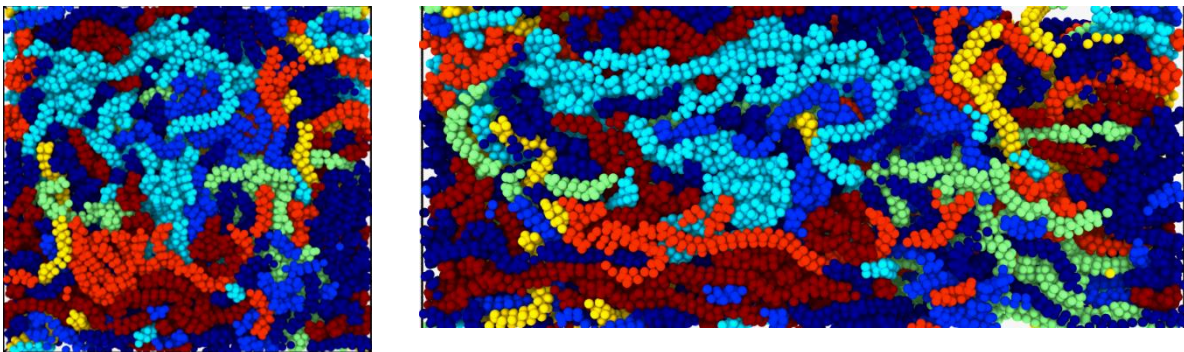


Figure 1.2(a). Randomly Oriented amorphous polyethylene b). Aligned Polyethylene

software. PACKMOL¹³ software is used to create a random configuration of hundreds of polymer chains in a defined region of space. System is relaxed, and material properties are simulated using

LAMMPS¹⁴ (Large-scale Atomic/Molecular Massively Parallel Simulator) MD simulator. Interatomic force interactions to compute atomic motions are modeled using existing force fields such as COMPASS¹⁵. Thermal conductivity of aligned polymers with varying degrees of alignment are simulated using non-equilibrium molecular dynamics based on Mueller-Plathe scheme¹⁶.

As another novel aspect of this research, change in temperature dependence of thermal conductivity is investigated as the polymer matrix is progressively aligned. In a recent publication¹⁷, we demonstrated that temperature dependence of thermal conductivity varies significantly as the polymer is strained. A peak in k is observed with respect to temperature shifting to lower temperatures upon aligning the system. Understanding of this temperature dependence was achieved in terms of a crossover from disorder to anharmonicity driven phonon transport, by varying the dihedral coefficients of polymer chain structure.

To increase the thermal conductivity further, I studied thermal transport in polymer nanocomposites by embedding the high thermal conductivity fillers. Nanomaterials like graphene nanoplatelets have ultra-high in plane thermal conductivity (k) of ~ 2000 W/mK¹⁸ and are thus attractive for enhancing k of polymers. Effectiveness of graphene in enhancing polymer thermal conductivity is, however, limited by large interface thermal resistance between polymer and graphene. Mismatch in phonon vibrational spectra of polymer and graphene and weak force interactions mediated by weak van der Waals interactions between polymer and graphene (in the absence of covalent bonding) lead to large interface thermal resistance at graphene/polymer interface which diminishes overall thermal conductivity enhancement in polymer-graphene nanocomposites. Functionalization of graphene¹⁹ with polymer chains can dramatically enhance force interactions between polymer and graphene leading to two orders of magnitude enhancement in interface conductance. Mingchao Wang²⁰ *et al.* reported 156% enhancement in thermal conductivity

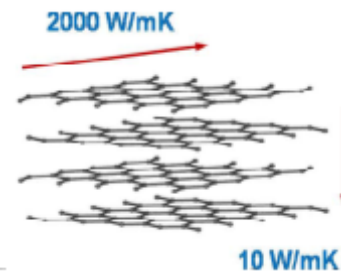


Figure 1.3. In plane and through plane k of GnPs

through grafting of polymer chains. To achieve even higher k -values it is critically important to identify bonding schemes with superior interface thermal conductance between polymer and graphene. Garg recently showed using first-principles Green's function calculations that edge-functionalization can lead to nearly 75%²¹ superior interface thermal conductance compared to

functionalization on the basal-plane. In chapter 3, I systematically investigated the superior effect of edge-functionalization on polymer-composite thermal conductivity through use of MD simulations. Our study shows that edge bonding can lead to significant enhancement in thermal transport over basal plane functionalization in polymer/graphene nanocomposites.

Phononic band gap in group III-V semiconductors can lead to a large increase in thermal conductivity of these materials²². Phonon band gap suppresses anharmonic scattering of phonons leading to a large increase in phonon lifetimes, with a corresponding increase in thermal conductivity. This effect was recently predicted to lead to the thermal conductivity of Boron-Arsenide exceeding even that of diamond. Strain can increase phononic band gap further suppressing scattering of phonons, thus increasing thermal conductivity. I used first-principles methods to study the effect of strain on thermal conductivity enhancement of boron phosphide (BP) semiconductor. I reported a high thermal conductivity (k) of 802.5 W/mK in 4% biaxially compressed Boron Phosphide at 300K and discussed in chapter 4. This value is 35.8% higher than thermal conductivity of unstrained boron phosphide (BP) and is almost 5-fold the thermal conductivity of silicon (Si). 4% strained BP is also found to be more efficient nanoscale heat conductor. At length scale of 200 nm and at 300 K, k of biaxially strained BP is estimated to be 150.4 W/mK, almost 25% higher, compared to the value of 120 W/mK for unstrained BP.

Likewise, thermoelectric materials require a low thermal conductivity to improve their figure of merit. Indium based semiconductors are promising materials for thermoelectric devices. In chapter 5, we report ~ 20% reduction in in-plane thermal conductivity of Indium arsenide (InAs) with 3% biaxial compressive strain. At 300 K, the bulk thermal conductivity of 33.85 $\text{Wm}^{-1}\text{K}^{-1}$ computed for unstrained indium arsenide (InAs) is reduced to 27 $\text{Wm}^{-1}\text{K}^{-1}$ for 3% biaxially strained InAs. Similarly, in chapter 6, we report a 29% decrease in k of InSb through biaxial strain. k value decreases from 18.8 W/mK for unstrained InSb to 13.4 W/mK for 5% biaxially compressed InSb at 300 K.

In Chapter 7-10, I report advanced material with high thermal conductivity in both bulk and nanoscale systems. In chapter 7, we report high thermal conductivities of 1350 $\text{Wm}^{-1}\text{K}^{-1}$ and 1050 $\text{Wm}^{-1}\text{K}^{-1}$ along a-axis and c-axis for pure 2H-GeC (Germanium Carbide). These values are 130% higher than the thermal conductivity of 2H-silicon carbide and 20% lower than cubic germanium carbide (c-GeC). We also studied the thermal conductivity of nanostructured 2H-GeC for heat dissipation in nanoelectronics. At room temperature, thermal conductivity of 2H-GeC at

nanometer length scale (L) of 100 nm is computed to be $70 \text{ Wm}^{-1}\text{K}^{-1}$, almost 100% higher than that of c-GeC (cubic-Germanium Carbide). In chapter 8, I report an ultra-high thermal conductivity of $2090 \text{ Wm}^{-1}\text{K}^{-1}$ ($1395 \text{ Wm}^{-1}\text{K}^{-1}$) for hexagonal pure (natural) BC_6N ($h\text{-BC}_6\text{N}$). This is the 3rd highest reported thermal conductivity of a bulk material after diamond and cubic boron arsenide. This ultra-high lattice thermal conductivity (k) is mainly attributed to high phonon group velocities of both acoustic and optical phonons arising from strong C-C and B-N bonds as well as the light atomic mass of the constituent elements such as boron(B), carbon(C) and nitrogen(N). At room temperature (300 K) and at nanoscale length (L) of 100 nm, k value of $175 \text{ Wm}^{-1}\text{K}^{-1}$ is observed. In chapter 9, I studied the thermal conductivity (k) of BC_5 , an ultra-hard diamondlike semiconductor material, using first-principles computations and analyzed the effect of isotopic disorder as well as length scale dependence. k of isotopically pure BC_5 is computed to be $169 \text{ Wm}^{-1}\text{K}^{-1}$ (along a-axis) at 300K. In chapter 10, I report a high thermal conductivity (k) of $162 \text{ Wm}^{-1}\text{K}^{-1}$ and $52 \text{ Wm}^{-1}\text{K}^{-1}$ at room temperature, along directions perpendicular and parallel to c-axis of bulk hexagonal BC_2P ($h\text{-BC}_2\text{P}$) respectively, using first principles calculations. BC_2P is also found to exhibit high thermal conductivity at nanometer length scales. At 300 K, a high k value of $\sim 47 \text{ Wm}^{-1}\text{K}^{-1}$ is computed for $h\text{-BC}_2\text{P}$ at nanometer length scale of 50 nm, providing avenues for achieving efficient nanoscale heat transfer. Interestingly, in $h\text{-BC}_2\text{P}$ optical phonons are found to make a large contribution of 30% to overall k along a direction perpendicular to c-axis at 300 K. These advanced materials discussed in chapter 7-9 can lead to improved thermal management at nanoscale.

Thermoelectric energy conversion requires low cost materials with ultra-low thermal conductivity. Magnesium chalcogenides-based semiconductors have attracted both scientific interest and technological applications. Among these, magnesium selenide and magnesium telluride are promising thermoelectric materials due to their ultrawide bandgap and high electron mobility. In chapter 11 and 12, I discussed the thermal conductivity of magnesium selenide magnesium telluride with different crystal structure such as; zincblende, rocksalt, wurtzite and nickel arsenic. We investigated the phonon bandgap and its effect on lattice thermal conductivity.

2D materials has unique properties and becomes as a prominent research interest after the invention of graphene. In chapter 13, We discuss the lattice thermal conductivity of graphene like germanium carbide(2D-GeC) for the first time and with 6% equi-biaxial tensile strain, we report $\sim 700\%$

enhancement in lattice thermal conductivity. We investigated the elastic constants, phonon group velocity and linewidth for the enhancement of thermal conductivity.

CHAPTER 2: THERMAL CONDUCTIVITY ENHANCEMENT IN ALIGNED POLYETHYLENE – MOLECULAR DYNAMICS STUDY

High thermal conductivity polymers play a key role in thermal management in wide array of applications including water desalination²³, solar energy harvesting²⁴, automotive control units²⁵, and micro-electronics²⁶. Polymers offer several advantages relative to metals such as low weight, low cost and lower fabrication energy²⁷. Alignment of polymer chains has emerged as a promising approach to enhance thermal conductivity of polymers^{28, 29}. Recently k of a single PE nanofiber with highly aligned PE chains was measured to be $104 \text{ Wm}^{-1}\text{K}^{-1}$ almost 200 times²⁸ larger than k of bulk PE ($\sim 0.5 \text{ Wm}^{-1}\text{K}^{-1}$). Aligned polymer chains also yielded a high thermal conductivity of $\sim 16 \text{ Wm}^{-1}\text{K}^{-1}$ in polyethylene films drawn to large ratios approaching ~ 100 ³⁰. More recently k of aligned polyethylene-graphene nanocomposites was measured to be significantly higher compared to k of aligned PE²⁹. While these studies shed light on k -enhancement through alignment effects at room temperature, experimental studies have also been performed to understand temperature dependence of k in aligned polymers. Choy *et al.*³¹ measured k of aligned semi-crystalline polymers such as polypropylene and low-density polyethylene. k along alignment direction was found to increase monotonically with temperature up to the highest studied temperature of 300 K. More recently Singh *et al.*³² measured k of chain-oriented amorphous polythiophene and found it again to be a weakly increasing function of T . In this work, we use non-equilibrium molecular dynamics (MD) simulations^{33, 34} to study temperature dependence of k of aligned amorphous PE. Alignment is achieved through application of strain.

Molecular dynamics (MD) simulations have been used in the past to study thermal transport in polymers. Zhang *et al.*³⁵ used MD simulations to study temperature dependence of thermal conductivity of un-oriented amorphous PE, and found it to reach maximum at a temperature of 350 K. This peak in k of un-oriented amorphous PE was explained through morphological considerations by describing the increase in k below 350 K in terms of increase in radius of gyration and decrease in k above 350 K in terms of reduced inter-chain interaction. Liu *et al.*³⁶ used MD to investigate role of strain rate on k of aligned amorphous PE at room temperature. Higher k -values were achieved for slower strain rates. Algaer *et al.*³⁷ used MD simulations to study temperature dependence of k of strained amorphous polystyrene, however, only small applied strains of up to 21% were considered in this study.

Aligned amorphous PE, focus of study in this work, differs in several aspects compared to polymer systems discussed above, providing novel avenues to understand thermal transport in chain-oriented polymers. Firstly, compared to semi-crystalline polymers, where two different phases exist (crystalline and amorphous), no such phase separation occurs in amorphous PE. Uniform morphology causes strain to uniformly impact the entire polymer structure. Absence of different phases can also eliminate phonon scattering that exists at the interface between crystalline and amorphous regions in semi-crystalline polymers, leading to potentially new features in temperature dependence of k . Furthermore, while previous MD simulations of k of amorphous polystyrene³⁷ considered strains of only up to 21%, in this work, we investigate much larger strains of 400%. At the small applied strains considered earlier, change in polymer structure was small, leading to small change in temperature dependence of k with respect to the unstrained case. Much larger strain used in this work^{17, 38}, will lead to significant structural changes, enabling associated larger changes in temperature dependence of k . Understanding of temperature dependence is of interest, both for gaining fundamental insights in to the underlying thermal transport processes in strained polymers, as well as for addressing low temperature applications of polymer based heat exchangers^{39, 40}.

2.1 METHODS - MOLECULAR DYNAMICS SIMULATION

To perform MD simulations of thermal transport, we use the LAMMPS⁴¹ simulation package. Interatomic force interactions needed to compute atomic motion are modeled using the COMPASS force field⁴². COMPASS is an *ab initio* force field and has been used widely to simulate polymer systems. To study thermal transport in amorphous PE, the structure of amorphous polymer is carefully constructed³⁵ (Fig. 2.1) by first equilibrating a single extended polyethylene chain of length 1000 C atoms at 300 K for 1 ns to form a compact relaxed chain. Choice of 1000 C atoms chain length leads to a good representation of the bulk behavior. 40 of these relaxed chains are

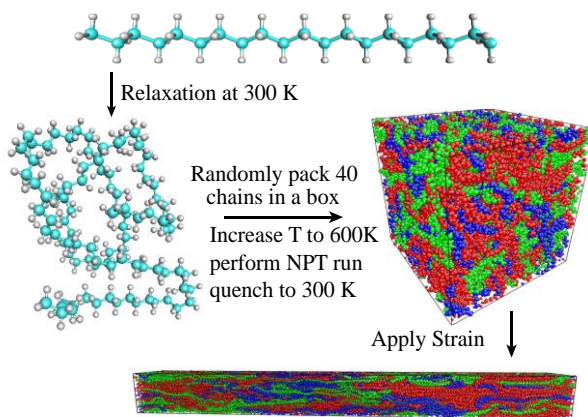


Fig. 2.1 Structure preparation of amorphous polyethylene and its alignment through application of strain.

then randomly packed into a cell leading to a total system size of 1.2×10^5 atoms. To achieve the final amorphous structure, the energy of the entire system is minimized followed by increasing the system temperature to 600 K at a rate of 50 K/ns using NPT (constant number of particles, pressure and temperature) ensemble, a further NPT run at 600 K for 4 ns to generate polyethylene system with relaxed and amorphous structure, then quenching the system to 300K and finally an NPT run for 4 ns to equilibrate the structure at 300K (Fig. 2.1).

After achieving the amorphous PE structure, deformation simulations were performed at 300 K to stretch the polymer. Strain was applied uniaxially along the x-axis of the periodic simulation cell to align the polymer chains along this direction (Fig. 2.1). Later thermal conductivity is reported along the same direction in this work. Pressure was kept constant at 1 atm for all other boundaries during deformation using NPT ensemble (Fig. 2.1). Strained polymer samples were further relaxed using NPT to obtain stable structures. Outlined procedure enabled polymer structures with strains of up to 400% to be achieved. The drawing process was performed at 300 K. To study the temperature dependence of k , temperature of the strained polymer was varied between 50 – 400 K again using NPT ensemble.

Thermal conductivity at different temperatures was computed using reverse non-equilibrium molecular dynamics (RNEMD) simulations based on the Muller-Plathe scheme⁴³ by imposing a heat flux j_x across a simulation cell and estimating the resulting average temperature gradient, $\langle \partial T / \partial x \rangle$. Fourier's law of heat conduction, $k_x = -j_x / \langle \partial T / \partial x \rangle$ was then used to compute the thermal conductivity k_x along stretch direction. Through the Muller Plathe scheme, system is divided in to bins, and heat flux is imposed by exchanging energies between the hot and the cold bins located at the center and edge of the system respectively. To achieve a reliable estimate of ensuing temperature gradient, RNEMD simulations were run for time period of 1 ns, long enough to yield the steady state. Simulation was then run for another 0.2 ns, during which the time-averaged temperature profile was estimated (typical profile for unstretched polymer at 300 K is shown in Fig. 2.2). Linear section of this profile was used to compute the temperature gradient.

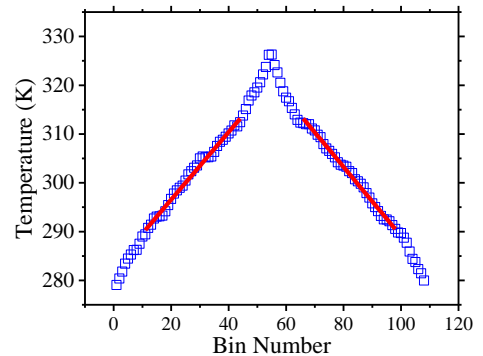


Fig. 2.2 Typical temperature profile obtained from NEMD simulations.

2.2 RESULTS

2.2.1 Thermal conductivity with strain

The results of thermal conductivity simulation at different strains and temperatures are provided in Fig. 2.3 (error bars are estimated by repeating simulations with different starting configurations). First, we notice that increasing the strain from 0% (unstrained) to 400% causes monotonic increase in thermal conductivity at each temperature. This enhancement in k with increasing strain is well understood in terms of increasing alignment of the dominant heat conducting C-C covalent bonds in each polymer chain with the direction of heat transfer. Such polymer chain alignment, typically characterized through calculation of an average orientational order parameter³⁶ (P_2) is shown in Fig. 2.4 for different temperatures. P_2 is estimated by describing the local chain direction at each atom by a unit vector, \mathbf{e}_i , computed from the chord vectors connecting the atom to its nearest neighbors: $\mathbf{e}_i = (\mathbf{r}_{i+1} - \mathbf{r}_{i-1})/|\mathbf{r}_{i+1} - \mathbf{r}_{i-1}|$ and taking the projection of \mathbf{e}_i along the alignment direction (x-direction) through the equation, $P_2 = 1.5\langle(\mathbf{e}_i \cdot \mathbf{e}_x)^2\rangle - 0.5$, where, \mathbf{e}_x is the unit vector in the direction of applied strain. The values of P_2 of the polymer samples after they are strained by different strains varying from 0% (unstretched) to 400% are shown in Fig 2.4. For the unstretched case, the value of P_2 is close to 0 indicating randomly oriented chains. As the strain is increased, the value of P_2 increases, suggesting increasingly aligned chains. P_2 is also only weakly dependent on temperature, indicating that alignment is mostly a function of strain. Increase in P_2 leads to the observed increase in k at each temperature.

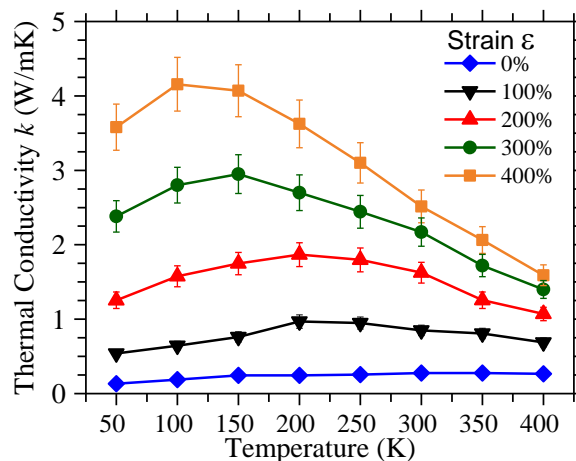


Fig. 2.3 Variation of thermal conductivity of amorphous polyethylene with temperature at different strains.

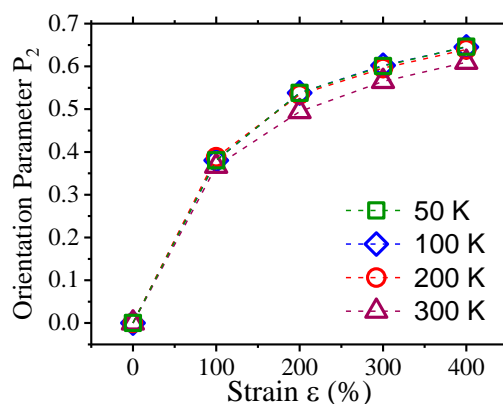


Fig. 2.4 Increase in orientation parameter P_2 with strain at different temperatures.

2.2.2 Temperature dependence thermal conductivity with strain

We next investigate the effect of temperature on thermal conductivity. Fig. 2.3 shows that the thermal conductivity for each strain reaches a maximum with temperature. For the unstretched polymer, thermal conductivity reaches a maximum at 350 K; this has been explained previously through morphological considerations³⁵. The focus in this work is on studying the change in temperature dependence as the polymer is strained. Fig. 2.3 shows that as the strain is increased, the temperature corresponding to maximum thermal conductivity (T_{peak}) shifts to lower values. For strain of 100%, maximum thermal conductivity is reached at a temperature of 200 K. As the strain is further increased to 400%, the temperature corresponding to peak thermal conductivity decreases to 100 K. This temperature corresponding to peak k for strain of 400% is lower compared to that for unstretched polymer by almost 250 K. Above results, suggest that strained amorphous PE can be even more effective for thermal management at lower temperatures. This is seen by noticing that while at a temperature of 350 K, drawing the polymer to a strain of 400% leads to an increase in thermal conductivity from 0.30 W/mK (unstrained case) to 2.0 W/mK representing an enhancement of ~6.5-fold in k , at the lower temperature of 200 K, a much larger enhancement in k of 18-fold is achieved from 0.24 W/mK to 4.43 W/mK, as the polymer is strained from 0% to 400%. We also studied size effects by using a smaller system size of 0.6×10^5 atoms. k was found to be higher for the larger system size of 1.2×10^5 atoms by 10-15%, however, peak k (focus of this study) occurred at the same temperature for both these systems.

2.2.3 ROLE OF DISORDER AND ANHARMONICITY

The large shift in T_{peak} with increasing strain can be understood in terms of an interplay between disorder and anharmonic phonon scattering. Heat in polymer systems is mainly conducted by lattice vibrations (phonons). Contribution of a phonon mode λ to overall thermal conductivity is described by⁴⁴, $k_{\lambda} \propto C_{\lambda} v_{\lambda}^2 \tau_{\lambda}$ where C_{λ} , v_{λ} and τ_{λ} are the specific heat, group velocity and lifetime, respectively, of the phonon mode λ . Lifetime of a phonon mode is determined by the total scattering rate ($1/\tau_{\lambda}$), equal to the sum of scattering due to both disorder $(1/\tau_{\lambda})^{disorder}$ and the anharmonicity $(1/\tau_{\lambda})^{anharmonicity}$ of polymer chains⁴⁴, $1/\tau_{\lambda} = (1/\tau_{\lambda})^{disorder} + (1/\tau_{\lambda})^{anharmonicity}$. Disorder scattering involves scattering of phonons from abrupt changes in chain orientation and across polymer chains^{45, 46}. Disorder scattering rates are mostly temperature (T) independent, while

anharmonic scattering rates increase linearly with temperature⁴⁴, being weak at low T and increasing at higher T . At low T , weak anharmonic effects result in disorder being the dominant scattering mechanism while at higher T anharmonic scattering increases in magnitude and begins to determine phonon lifetimes. T_{peak} corresponds to this transition from disorder to anharmonic phonon transport. This is seen by observing that at low T , the dominant disorder scattering is independent of temperature⁴⁴, causing τ_λ to become constant. Specific heat (C), however, has been known to increase with T even in classical MD simulations due to anharmonic effects⁴⁷, causing k_λ to also increase with T in the disorder dominated regime. At high T , in the anharmonicity dominated regime, however, anharmonic scattering rates increase with increasing T causing phonon lifetimes, τ_λ , to decrease as T is increased, now causing the thermal conductivity (k) to decrease with increasing T . Increasing k with increasing T in the disorder dominated regime, followed by the opposite trend in the anharmonic regime, causes k to reach a peak at the temperature corresponding to transition from disorder to anharmonicity dominated phonon transport.

As the strain increases, transition from disorder to anharmonic regime shifts to lower T causing T_{peak} to also shift to lower values. This can be understood by noticing that at the low alignment levels achieved at low strains, polymer chains still have large number of abrupt turns and bends, leading to large disorder which causes disorder scattering rates to be large⁴⁸. It requires a large increase in anharmonic scattering, to exceed these large disorder scattering rates, in turn requiring high temperatures, thus causing the peak k to occur at high T . As the applied strain is increased, the polymer structure becomes more aligned, causing the level of disorder to decrease. Relatively smaller increases in anharmonic scattering (requiring low T) can now cause it to overcome disorder scattering. Transition from disorder to anharmonic regime thus occurs at progressively lower T at higher strains, explaining the shift in peak k to lower T with increasing strain observed in Fig. 2.3.

We provide evidence supporting the above presented mechanism for shift in T_{peak} with increasing strain, by modifying system disorder and observing the

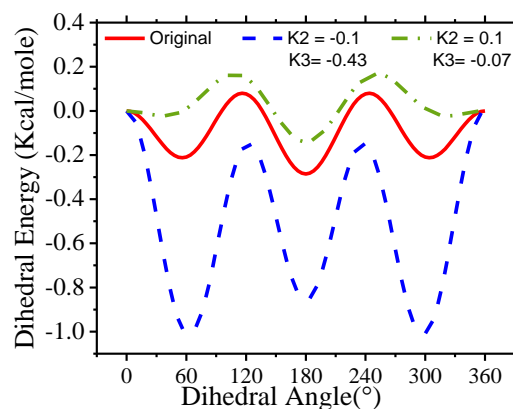


Fig. 2.5 Dihedral energy for original COMPASS potential and for modified dihedral parameters.

resulting changes in T_{peak} . According to the presented mechanism, increasing the system disorder should shift T_{peak} to higher values. At higher disorder, transition from disorder to anharmonicity dominated phonon transport would require higher anharmonic scattering rates, in turn requiring higher temperatures, causing T_{peak} to shift to higher values. Vice versa, a decrease in disorder should shift T_{peak} to lower values. Both anharmonicity and disorder can be changed by modifying the potential parameters. Effect of change in disorder can, however, be studied in isolation without impacting other parameters such as phonon frequencies. This can be achieved by changing the dihedral energy parameters. Dihedral energy parameters control torsion angles, thus enabling control of the structure of the polymer chain, and therefore disorder. Since dihedral energies are much smaller than bond energies (as seen by noticing that the largest coefficients in energy terms for bond energy are of the order of 345 Kcal/mole while those for dihedral energies are ~ 0.1 Kcal/mole), changing dihedral terms does not significantly impact vibrational frequencies (which are instead determined by bond energies), enabling understanding of the effect of change in disorder alone. Changing anharmonicity, however, requires a change in bond energy parameters (since bond energy terms are the largest contributors to anharmonicity), which also leads to a change in vibrational frequencies, precluding a study of the effect of change in anharmonicity alone. We therefore choose to study the effect of change in disorder through a change in dihedral energy parameters of the C-C-C-C dihedral, as these are most relevant for controlling polymer backbone chain structure.

Through COMPASS⁴² potential, dihedral energy is computed using the expression $E_{dihedral} = K1(1 - \cos\phi) + K2(1 - \cos(2\phi)) + K3(1 - \cos(3\phi))$. For the C-C-C-C dihedral, the parameters $K1$, $K2$, $K3$ are given by $K1 = 0$, $K2 = 0.054$ and $K3 = -0.143$ Kcal/mole. The energy for these parameters is shown in Fig. 2.5 (solid red line) and the distribution of the dihedral angles for this case is shown in Fig. 2.6 (labeled ‘Original’ in the figure). The

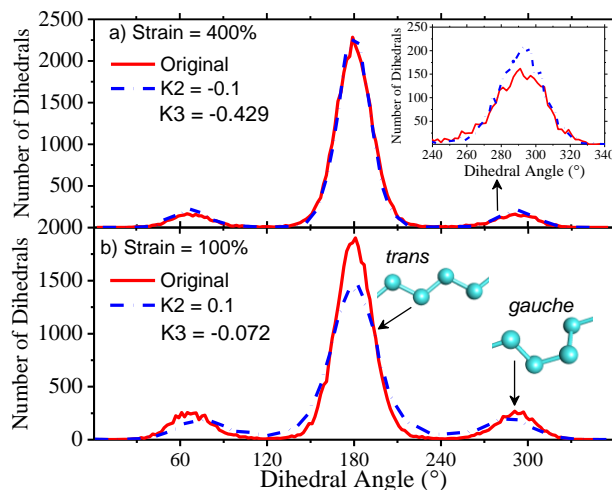


Fig. 2.6 Distribution of dihedral angles for modified and original dihedral parameters for strains of a) 400% and b) 100%.

dihedral angle of 180° corresponds to *trans* conformation, while dihedral angles of 60° and 300° correspond to *gauche* transformation. *Trans* conformations lead to stiff straight chains, while *gauche* transformations allow change in orientation, introducing disorder. By manipulating the parameters, $K1$, $K2$ and $K3$, the relative distribution of *trans* and *gauche* conformations can be modified, changing disorder.

As a first effect, we increase disorder by changing the parameters to $K1 = 0$, $K2 = -0.1$, and $K3 = -0.43$ Kcal/mole for the polymer with 400% strain. This corresponds to the energy profile shown by dashed blue line in Fig. 2.5. By lowering the energy corresponding to *gauche* state, number of *gauche* transformations is increased (Fig. 2.6a), thereby increasing disorder. To compute k for the new set of parameters, polymer matrix was prepared with these modified dihedral coefficients, strained by 400%, and finally relaxed to different temperatures to compute k as a function of temperature. The results are shown in Fig. 2.7 (values for original and modified dihedral parameters are shown by solid and open squares respectively). First it is noticed that compared to k computed using original dihedral parameters (solid squares in Fig. 2.3), the k computed using modified parameters is lower, as expected for a system with increased disorder. Secondly, while k through the original parameters reached peak at 100 K (Fig. 2.3 and 2.7), the k using modified parameters (leading to higher disorder) reaches maximum at higher temperature of 150 K (Fig. 2.7). This is in agreement with the presented mechanism.

Next, we also decrease disorder by manipulating dihedral energy parameters and study its impact on k of polymer with strain of 100%. A decrease in disorder should cause anharmonicity to become dominant at lower temperatures, shifting the peak k to lower temperatures. To achieve lower disorder, we decrease the number of *gauche* transformations by using the parameters of $K1=0$, $K2=0.1$ and $K3=-0.072$ Kcal/mole. These parameters cause the energy corresponding to *gauche* state to increase (dashed-dotted line in Fig. 2.5), causing the number of *gauche* transformations to decrease

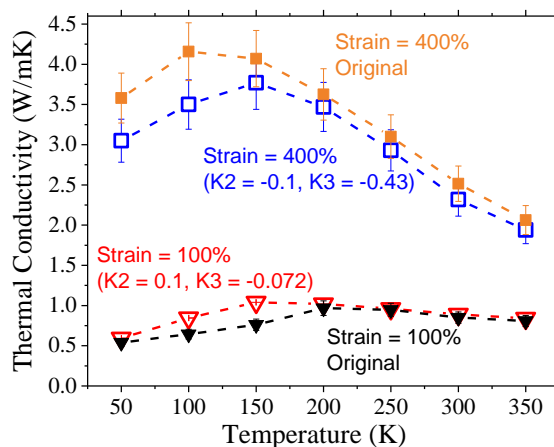


Fig. 2.7 Temperature dependence of k of amorphous PE with modified and original dihedral parameters for strains of 100% and 400%.

(Fig. 2.6b) thus lowering disorder. The thermal conductivity of strained polymer with strain of 100% and prepared with these new dihedral parameters is shown in Fig. 2.7 (as open triangles). The k value for the new set of parameters is found to be higher compared to the original COMPASS potential, as expected for a system with lower disorder. Again, while k through the original parameters reached peak at 200 K, the k using modified parameters (leading to lower disorder) reaches maximum at lower temperature of 150 K, again in agreement with the presented mechanism.

Above results validate the presented mechanism for shift in T_{peak} to lower values with increasing strain. Presented results for strained amorphous PE differ from measurements on strained amorphous polythiophene, where for the strained case, k was found to be a weakly increasing function of T even at higher temperatures³². This was explained in terms of presence of only short-range order in strained polythiophene, leading to phonon transport being dominated by disorder even in strained system. The opposite trend of decreasing k with increasing T in strained amorphous PE at higher T (\sim 200-300 K) suggests longer range order which causes phonon transport to be anharmonicity dominated at higher T . Above results, showing a transition of peak k to lower temperatures, suggest that strained polymers can be even more effective for thermal management at lower temperatures.

2.3 CONCLUSION

In summary, we have studied the temperature dependence (in the range of 50-400 K) of thermal conductivity of amorphous polyethylene drawn to strains of up to 400% using molecular dynamics simulations. Results demonstrate that thermal conductivity (k) peaks with respect to temperature for all strains; this temperature corresponding to peak thermal conductivity shifts to lower values as the applied strain increases. While k of unstretched polymer is maximum at 350 K, k of polymer with strain of 100% peaks at 200 K. This values further decreases to 100 K for strain of 400%. The effect is explained in terms of a cross-over from disorder to anharmonicity dominated phonon scattering regime. Increasing strain decreases disorder, allowing anharmonic scattering to become dominant at progressively lower temperatures, causing the peak k temperature to shift to lower values. The effect is validated by modifying disorder through a change in dihedral energy parameters. Increasing the disorder is found to shift the temperature related to peak k to higher

values; vice versa, decreasing the disorder lowers that temperature. Both these results agree with the presented mechanism. Shift in peak k to lower temperatures at higher strains leads to significant enhancement in k of aligned amorphous PE at lower temperatures. These results can lead to new avenues for use of aligned polymers for thermal management at sub-ambient temperatures.

CHAPTER 3: SUPERIOR EFFECT OF EDGE RELATIVE TO BASAL PLANE FUNCTIONALIZATION OF GRAPHENE IN ENHANCING POLYMER-GRAPHENE NANOCOMPOSITE THERMAL CONDUCTIVITY

Thermal conductivity of polymers can also be enhanced further by blending of polymers with high thermal conductive fillers⁴⁹⁻⁵¹ and crosslinking of polymers. Graphene^{49, 50} is widely used as a filler because of its superior k of 2000-5000 $\text{Wm}^{-1}\text{K}^{-1}$. However, enhancement of nanocomposite thermal conductivity through addition of graphene nanoplatelets is limited due to large interface thermal resistance between polymer and graphene⁵². The large interfacial thermal resistance is due to the mismatch in phonon vibrational spectra between polymer and graphene. Interfacial thermal conductance can be significantly increased by functionalizing graphene with chemical groups that are compatible with surrounding polymer⁵³. Two orders of magnitude increase in interface conductance was obtained through functionalization of graphene with polymer chains⁵⁴. 156% enhancement in thermal conductivity was achieved through grafting of polymer chains on to graphene²⁰. To achieve largest enhancement in thermal conductivity, it is essential to achieve understanding of functionalization schemes that lead to largest enhancement in thermal conductivity.

Konatham *et al.*⁵⁵ demonstrated almost 50% reduction in the interfacial thermal resistance between functionalized graphene and octane using molecular dynamics (MD) simulations study. It was suggested that edge functionalization retained efficient thermal transport phenomenon without compromising graphene structure. Comparative study between edge and basal plane functionalization revealed the superiority of edge bonding by 75% over the basal plane functionalization²¹. Mungse *et al.* presented excellent tribo-interfaces through the basal plane functionalization of graphene oxide using long octadecyl chains⁵⁶ and also developed edge functionalized graphene oxide modified by octadecyl amine which enhanced the stability of dispersion and mechanical strength⁵⁷. In another study, the effect of interconnected 3D network structure of edge or basal plane modified graphene oxide on electrical conductivity⁵⁸ was studied. Different studies^{54, 57, 59-61} show this structural effect of functionalized graphene on the mechanical and physical properties of composites.

In this study, we demonstrate for the first time that functionalization on edge can lead to superior thermal conductivity enhancement relative to functionalization on basal plane using MD simulation. We carried out molecular dynamics simulations of the effect of graphene

functionalized with polyethylene chains on both basal plane and edge, on thermal conductivity enhancement of polyethylene-graphene nanocomposites. We analyzed the effect of number of graphene layers within the nanoplatelet on overall heat transfer enhancement in the polymer nanocomposites. Role of inner layers in phonon thermal transport is elucidated using phonon vibrational power spectrum for each sheet in both edge and basal plane functionalization.

3.1 METHODS

3.1.1 Molecular Dynamics Simulations

To simulate the thermal transport in polymer nanocomposites using MD simulation, we employed LAMMPS¹⁴ package. we use the Condensed Phase Optimized Potentials for Atomic Simulations (COMPASS)¹⁵ force field to define the interactions between the atoms. Interactions between graphene layer, functionalized materials and the polymers are described by Lennard-Jones potential. Polyethylene chain and functionalized graphene nanoplatelet (with lateral dimension of 10nmx10nm and with different number of layers) were constructed in Nanoengineer-1 (figure 1a,b and c) and the molecules were packed using PACKMOL⁶². We have modelled the composites with 35% weight of graphene nanoplatelet for all of our simulations. Energy minimization using conjugate gradient algorithm was performed and the structure relaxed in isothermal-isobaric (NPT) ensemble at 1 atm and 300 K for 5 ns to release the residual stress. We simulated all the systems with a timestep of 0.1 fs throughout. Prior to final calculations, our systems were analyzed critically for any possible voids using visual molecular dynamics (VMD)⁶³. The heat transfer in polyethylene and functionalized graphene nanocomposites were investigated using non-equilibrium molecular dynamics (NEMD)⁶⁴ simulation where opposite ends of the simulation box were thermostatted with a temperature difference of 50 K.

To validate our models, we simulated the thermal conductivity of pure polyethylene with a density of 0.72 gcm⁻³ and computed the value to be 0.3 Wm⁻¹K⁻¹ at 300 K which is in good agreement with other simulations^{17, 65} and experimental results.

3.2 RESULTS

3.2.1 Overall composite comparison

To compare edge and basal plane case, we prepared composite embedded with edge and basal plane functionalized graphene nanoplatelet (simulation details are presented in section 3.1.1). A temperature difference of 50 K was imposed across the composite and resulting heat flux was

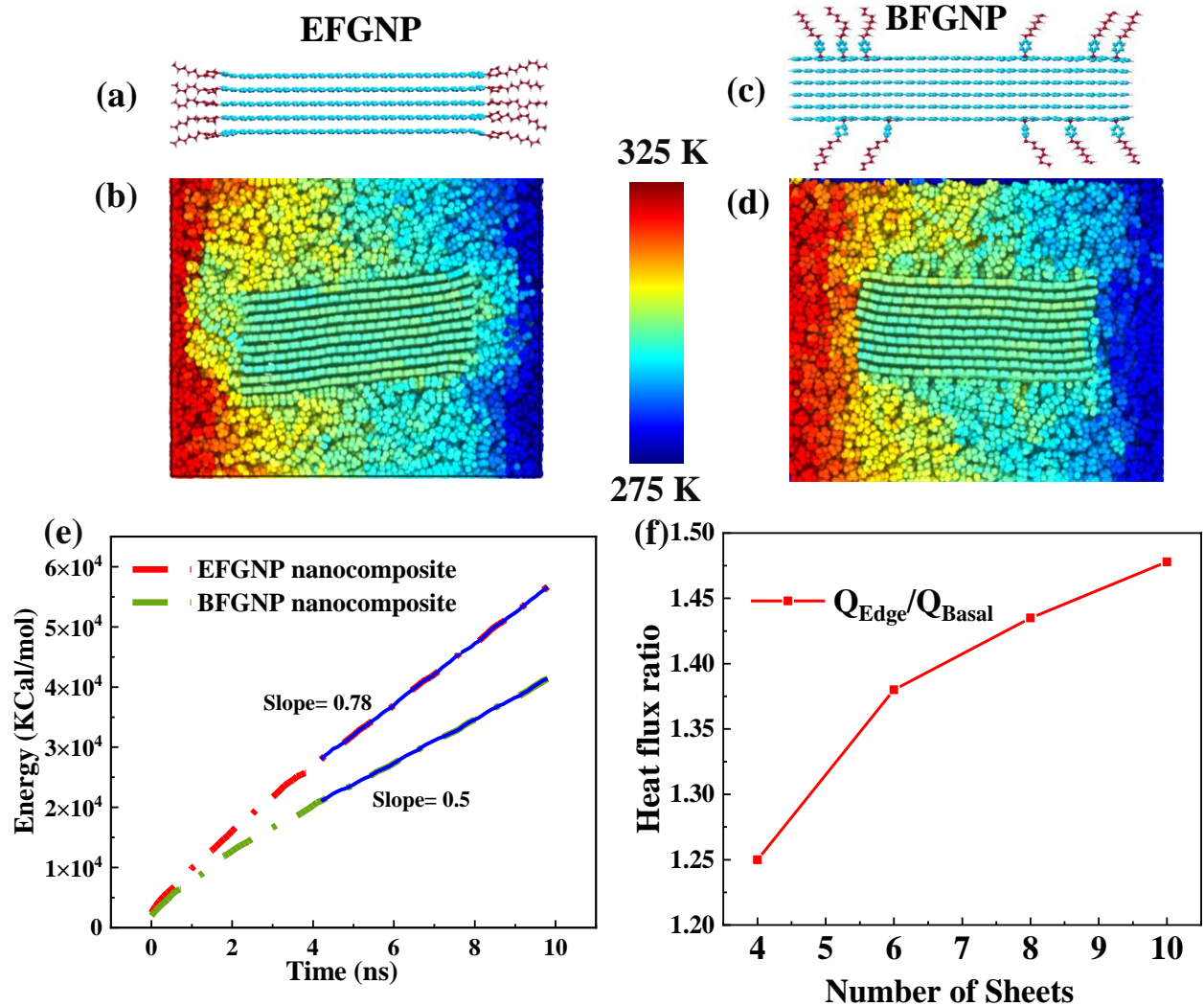


Figure 3.1. (a) EFGNP (Edge functionalized graphene nanoplatelet), (c) BFGNP (Basal plane functionalized graphene nanoplatelet), (b) and (d) Temperature Profiles in (b) PE/EFGNP & (d) PE/BFGNP nanocomposite, respectively (e) Energy transferred as a function of time for edge and basal plane cases, (f) Heat flux ratio for different nanoplatelet thicknesses.

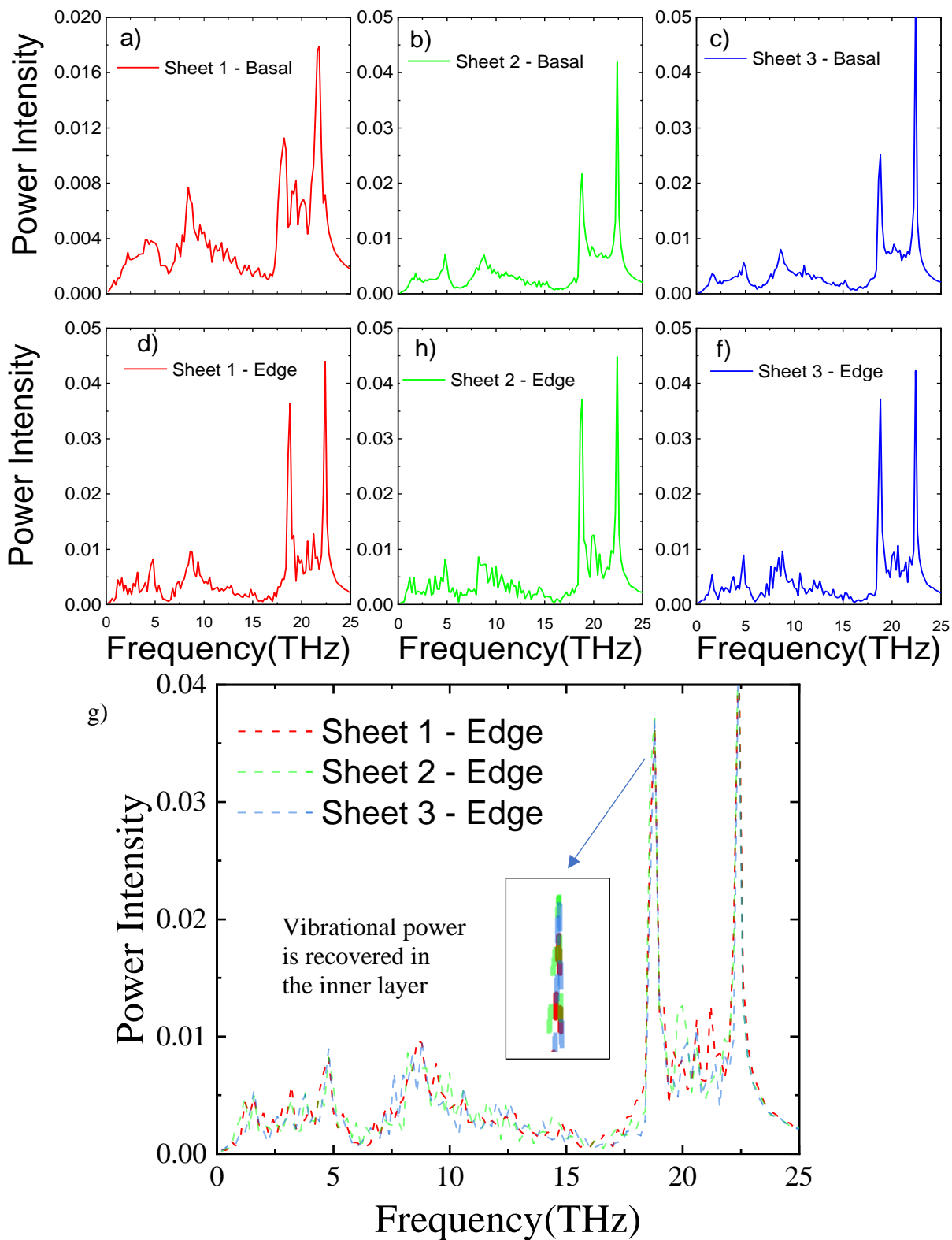


Figure 3.2 a-g). Vibrational power spectra across different layers in EFGNP and BFGNP. High vibrational power in EFGNP inner layer than BFGNP is due to strong coupling of in-plane phonons. compared. Two ends of the simulation box were thermostatted for NEMD simulation with a

temperature difference (ΔT) of 50 K and the energy exchange between the thermosetted region were plotted with time as shown in Fig 3.1a. The heat flux was calculated using the slope value from the plot.

$$J = \Delta E / (A \cdot \Delta t) \quad (3.1)$$

where ΔE is the change in energy, A is the cross-sectional area and t is the total time. Energy exchange (ΔE) with time is shown in Fig 3.1a for EFGNP and BFGNP. We can observe that heat flux for the EFGNP is higher than BFGNP. Fig 3.1a shows an almost 48% higher heat flux for edge case. This higher heat flux is mainly due to all layers of graphene nanoplatelet being efficiently coupled to polymer matrix leading to lower interfacial thermal resistance for edge bonding case. Such coupling of all layers ensures that the entire graphene nanoplatelet participates in heat transfer for edge case, while for basal plane case, only the outermost layers participate. The effect of this efficient coupling in enhancing heat transfer can be seen directly in Fig 3.1 c and d. by comparing temperature profiles across the nanocomposite for the two cases; for the edge case temperature profiles is significantly smoother at the interface between graphene and polymer, relative to basal plane case, indicating a smaller interface thermal resistance, resulting in higher effective thermal conductivity. In addition to the edge bonding enabling the beneficial effect of coupling all graphene layers to polymer, we demonstrate other advantages of edge bonding in this work, namely a) allowing heat to be conducted by inner layers, which are less damped by surrounding polymer and b) higher thermal conductivity of edge-functionalized graphene sheets (studied using MD).

3.2.2 Effect of number of sheets on interface conductance

The effect of number of sheets ($n = 4, 6, 8$ and 10 sheets) on the difference in heat flux (ΔJ) between EFGNP/PE and BFGNP/PE is calculated using molecular dynamics simulation. For each n , filler weight percentage is kept constant (35%) and the functionalized graphene nanoplatelet and polymers were packed into the simulation box using PACKMOL⁶² package and the system is relaxed for 5 ns. The heat flux difference between EFGNP and BFGNP increases with increase in n for both EFGNP and BFGNP. For example, with 4 sheet thick nanoplatelet, EFGNP has 25% high flux than BFGNP; as the sheet thickness increases to 10, this difference in heat flux also increases to 48%. The difference in heat flux (ΔJ) increases with increase in n due to basal plane functionalized nanoplatelet becoming progressively less efficient in conducting heat with increase

in thickness (mediated by larger number of inner layers which are not efficiently coupled to the surrounding polymer) as compared to the edge case, where all layers conduct heat efficiently.

3.2.3 Single Nanoplatelet

As discussed above, the key effect leading to higher heat flux for edge case, is the coupling of all graphene layers with surrounding polymer matrix. To demonstrate this more effectively Fig. shows that when temperature gradient is applied across all layers of the nanoplatelet, the resulting

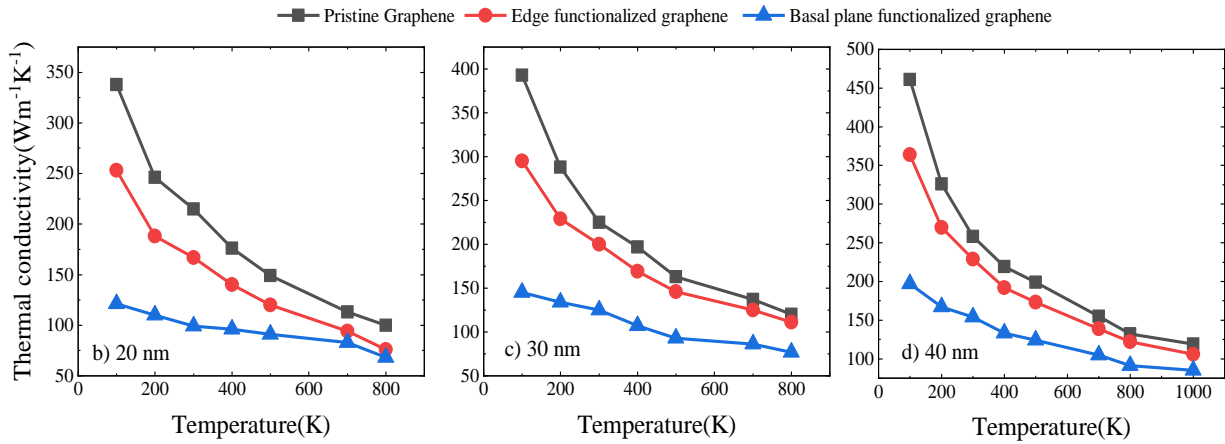


Figure 3.3 : Temperature dependence thermal conductivity of pristine, edge functionalized and basal plane functionalized graphene at a) 20 nm b) 30 nm c) 40nm

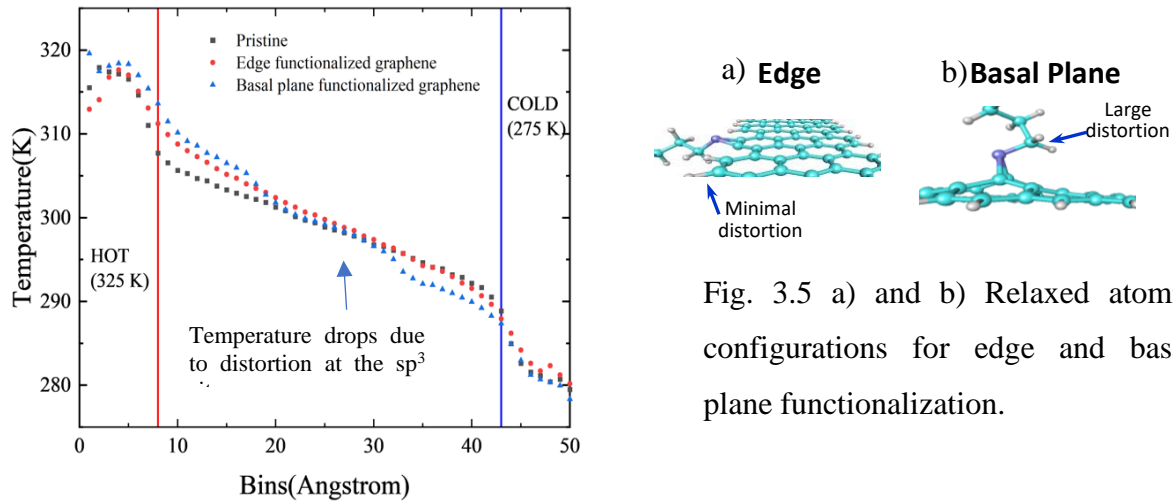


Figure 3.4 : Temperature distribution along the simulation box in pristine, edge and basal plane functionalized graphene heat flux is much higher, as opposed to the case when temperature gradient is applied across only the top and bottom layers. These simulations were performed for a single nanoplatelet.

3.2.4 Power density spectrum

As another significant advantage of edge-functionalization, we show that vibration damping induced by surrounding polymer more adversely impacts basal plane functionalized case. It is well understood that during heat conduction the vibrations in the outer layers of a graphene nanoplatelet are damped by the surrounding polymer. Since outer layers are more important for heat conduction in the case of basal plane functionalization, a damping of vibrations in outer layers by surrounding polymer, more adversely impacts the heat transfer performance for basal plane functionalization. To clearly quantify this effect, we use the phonon vibrational power spectrum in this work.

The phonon vibrational power spectrum is a powerful method based on computing the discrete Fourier transform of the velocity autocorrelation function as shown below⁶⁶,

$$D(\omega) = \int_0^{\tau} \langle v(0).v(t) \rangle \exp(-i\omega t) dt \quad (3.2)$$

where $\langle v(0).v(t) \rangle$ is the velocity autocorrelation obtained by correlating the velocity at every 2 fs, τ is the total correlation time = 5 ps and $D(\omega)$ is the phonon vibrational power spectra at frequency (ω). Figs 3.3 a-h show the vibrational power spectrum computed for individual sheets in a 6 sheet nanoplatelet for both edge and basal plane functionalization case. The Sheet 1 denotes the outermost layer from bottom. Due to the symmetry in nature, we have shown the vibrational power spectra of sheets 1-3. Since the outer layers of BFGNP is functionalized, its vibrating power is more suppressed than EFGNP (Figure 3.2 a and e as shown in sheet1). The vibrating power in inner layer of EFGNP and BFGNP is recovered by increasing the number of layers and is less dampen by the surrounding polymers (Figure 3.2 f-h). We may also notice that, the damping effect is realized in 2nd layer of BFGNP from the outer layer. Since all the layers in EFGNP is functionalized, the strong coupling of in-plane phonons increases the vibrational power in EFGNP whereas there is no coupling between the polymers and the graphene in BFGNP and hence its inner layer has poor vibrational power (Figure 3.2 b-d).

3.2.5 Thermal conductivity of individual graphene sheets

As yet another advantage of edge-bonding, we show that edge-bonded graphene sheets have superior thermal conductivity relative to basal plane functionalized graphene sheets. To understand effects of functionalization on thermal conductivity of a single layer graphene, we computed the temperature and length dependent thermal conductivity of individual functionalized

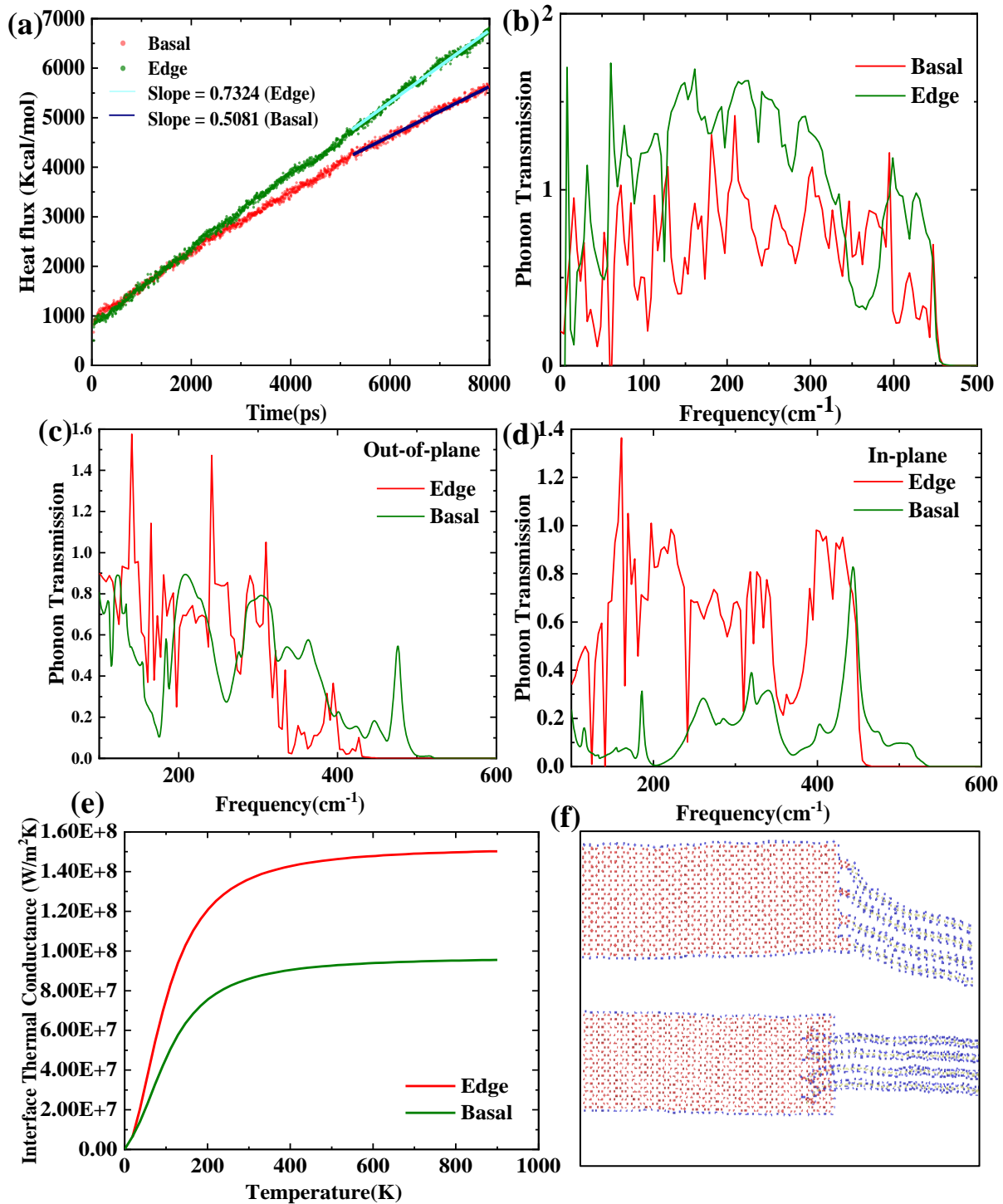


Figure 3.6 (a) Heat flux, b) Overall phonon transmission, c) In-plane phonon transmission, d) Out of-plane phonon transmission, e) Interface thermal conductance and f) Relaxed structures of single sheet edge and basal plane functionalization graphene sheet and compared with pristine graphene. We can observe that, upon functionalization, edge functionalized graphene has higher thermal conductivity than the basal plane

functionalization case. At length scale of 10 nm, and at room temperature (300 K), thermal conductivity (k) of $106 \text{ Wm}^{-1}\text{K}^{-1}$ computed for pristine graphene reduced to $93 \text{ Wm}^{-1}\text{K}^{-1}$ and $78 \text{ Wm}^{-1}\text{K}^{-1}$ for the edge and basal plane functionalized graphene respectively. Similarly, at 40 nm length scale, k for pure, edge functionalized and basal functionalized graphene are $219 \text{ Wm}^{-1}\text{K}^{-1}$, $192 \text{ Wm}^{-1}\text{K}^{-1}$ and $133 \text{ Wm}^{-1}\text{K}^{-1}$ respectively. This reduction in thermal conductivity upon functionalization is due to the distortion in the graphene structure. Large reduction in thermal conductivity in basal plane functionalization is attributed to much larger distortion of graphene in its basal plane as shown in Fig 3.5b. Edge bonding distorts graphene to a much smaller degree compared to basal plane case, seen in the relaxed DFT structures in Fig. 3.6a and b. Carbon atoms on the basal plane of graphene are sp^2 hybridized; in forming an extra bond to functionalize, they transform to sp^3 state, protruding outwards and distorting graphene in the process. Unlike inner carbon atoms, edge atoms can adopt tetrahedral geometries more freely without causing extra strain. Hence, lower distortion through edge bonding can result in significantly higher k_{graphene} relative to basal plane case. To elucidate further, we plotted the temperature distribution along the simulation box in 10 nm pristine, edge functionalized and basal plane functionalized graphene. We have divided the simulation box (100 \AA) into 50 bins. We can observe a sudden temperature drop at the functionalized site in basal plane functionalization indicating a reduction in thermal conductivity ($k = (Q \cdot \Delta x) / (A \cdot \Delta T)$). Temperature distribution within the edge functionalized graphene is, however, linear due to the minimal distribution. Hence, edge functionalization conducts heat better than basal plane functionalized graphene.

3.3 CONCLUSION

Using molecular dynamics simulation, we systematically studied the effects of edge and basal plane functionalization in graphene for thermal conductivity in graphene nanocomposites. Our MD simulations reveals that, edge functionalization has better heat flux than basal functionalization and the different in heat flux increases with number of layers since the inner layers are actively participating in heat conduction in edge than basal plane case. Also, edge functionalization has low distortion compared to basal plane functionalization means less damage to the graphene structure and has better thermal transport.

CHAPTER 4: BIAXIAL STRAIN INDUCED THERMAL CONDUCTIVITY ENHANCEMENT IN BORON PHOSPHIDE – A FIRST PRINCIPLES STUDY

Materials with high thermal conductivity are a primary focus for the modern electronic industries in order to improve thermal management for improving device performance and reliability^{67, 68}. Boron Phosphide (BP) is an isotropic semiconductor with superior properties such as high mechanical hardness⁶⁹, chemically inertness, high thermal conductivity⁷⁰ and stability at high temperatures⁷¹. Electrical⁷², thermal⁷³ and magnetic properties of a semiconductor can be manipulated through strain and pressure. Thermal conductivity of a semiconductor can be modulated through various mechanism such as doping, defects, pressure and strain. Strain affects the materials properties through changes in structure, lattice constants, symmetry⁷⁴ and band gaps^{75, 76}. Strain may increase or decrease the thermal conductivity of the materials based on their structural properties. Thermal conductivity enhancement in semiconductors⁷³, polymers¹⁷ and polymers nanocomposites⁷⁷ through strain has been reported in various works. Mostafa *et. al*⁷⁸ reported 125% increase in thermal conductivity of hexagonal boron arsenide (h-Bas) for 3% strain. Recently 53% enhancement in thermal conductivity of Gallium Nitride(GaN) with 5% biaxial compressive strain was reported by Dao Sheng *et. al*⁷⁹. Thermal conductivity of silicon film was found to decrease with the strain⁸⁰. In this work we study effect of strain on thermal conductivity of BP. We find the 24.21% and 48.3% enhancement in in-plane thermal conductivity of Boron Phosphide⁸¹ for 2% and 4% biaxial compression respectively using first-principles calculations. This enhancement in thermal conductivity upon biaxial compression is attributed to the suppression of phonon-phonon scattering and thus increase in phonon lifetime. This is explained through increase in phonon bandgap upon biaxial compression. We also observed anisotropy in thermal conductivity with in-plane thermal conductivity becoming higher than out of plane thermal conductivity. This provides an avenue for tuning the thermal conductivity of semiconductors through biaxial compression. The increase in thermal conductivity is observed through reduction in phonon linewidth⁸²⁻⁸⁴, which is a measure of the scattering rate.

At nanometer length scales, Fourier law of heat conduction breaks down, decreasing effective thermal conductivity below bulk value, exacerbating heat dissipation in the process. The effect has been shown to lead to overheating, reducing reliability and performance in nanoelectronics applications. The effect was also demonstrated experimentally. To improve thermal management at nanoscale, there is a strong need for materials with enhanced thermal

conductivity at these length scales. In this work, we also show that biaxial strain can significantly enhance thermal conductivity of Boron Phosphide at nanoscale by specifically suppressing scattering of phonons at higher frequencies, where phonon meanfreepaths are in the nanometer range.

4.1 DENSITY FUNCTIONAL THEORY(DFT): Thermal conductivity in this work is predicted for cubic Boron Phosphide using first principles calculations^{85, 86} which involve solving the Phonon Boltzmann Transport Equation (PBTE), both in the single mode relaxation time approximation (SMRT) and also exactly. The key step, in the approach involves deriving 2nd and 3rd order interatomic force constants (IFCs), needed for k prediction, from density-functional theory (DFT).

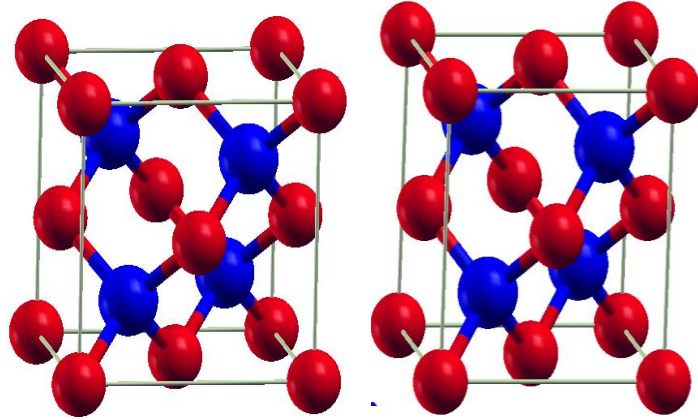


Figure 4.1a. Cubic Boron phosphide crystal structure with lattice constant as 8.44 Å. b) Boron Phosphide after 4% compression in x and y direction and relaxed in z

DFT has been shown to yield highly accurate IFCs, overcoming limitations of empirical potentials, leading to unprecedented accuracy in the prediction of lattice k . Thermal conductivity (k) prediction, based on solving of PBTE⁸⁷ in the single mode relaxation time (SMRT) approximation, is given by,

$$k_{\alpha} = \frac{\hbar^2}{N\Omega k_b T^2} \sum_{\lambda} c_{\alpha\lambda}^2 \omega_{\lambda}^2 \bar{n}_{\lambda} (\bar{n}_{\lambda} + 1) \tau_{\lambda} \quad (4.1)$$

where α , \hbar , Ω , k_b , T , are the cartesian direction, Planck constant, unit cell volume, Boltzmann constant, and absolute temperature respectively. λ represents the vibrational mode (qj) (q is the wave vector and j represents phonon polarization). N is the size of the q mesh used for summation in above equation. ω_{λ} , \bar{n}_{λ} , and $c_{\alpha\lambda}$ ($= \partial\omega_{\lambda}/\partial q$) are the phonon frequency, equilibrium Bose-Einstein population and group velocity along cartesian direction α , respectively of a phonon mode λ . These are derived from the knowledge of phonon dispersion computed using 2nd order IFCs. τ_{λ} is the phonon lifetime (equal to the inverse of scattering rate). In the SMRT approximation, phonon lifetime (τ_{λ}) is computed using the following equation,

$$\frac{1}{\tau_\lambda} = \pi \sum_{\lambda'\lambda''} |V_3(-\lambda, \lambda', \lambda'')|^2 \times [2(n_{\lambda'} - n_{\lambda''})\delta(\omega(\lambda) + \omega(\lambda') - \omega(\lambda'')) + (1 + n_{\lambda'} + n_{\lambda''})\delta(\omega(\lambda) - \omega(\lambda') - \omega(\lambda''))] \quad (4.2)$$

where $V_3(-\lambda, \lambda', \lambda'')$ are the three-phonon coupling matrix elements computed using both 2nd and 3rd order IFCs. Phonon scattering due to anharmonicity can be classified into two processes – absorption and decay processes. In absorption process, a phonon mode ($q\omega$) scatters by absorbing another phonon mode ($q'\omega'$), yielding a higher energy ($q''\omega''$) phonon mode, whereas in decay process, a phonon mode decays into two lower energy phonons. Both processes satisfy energy and

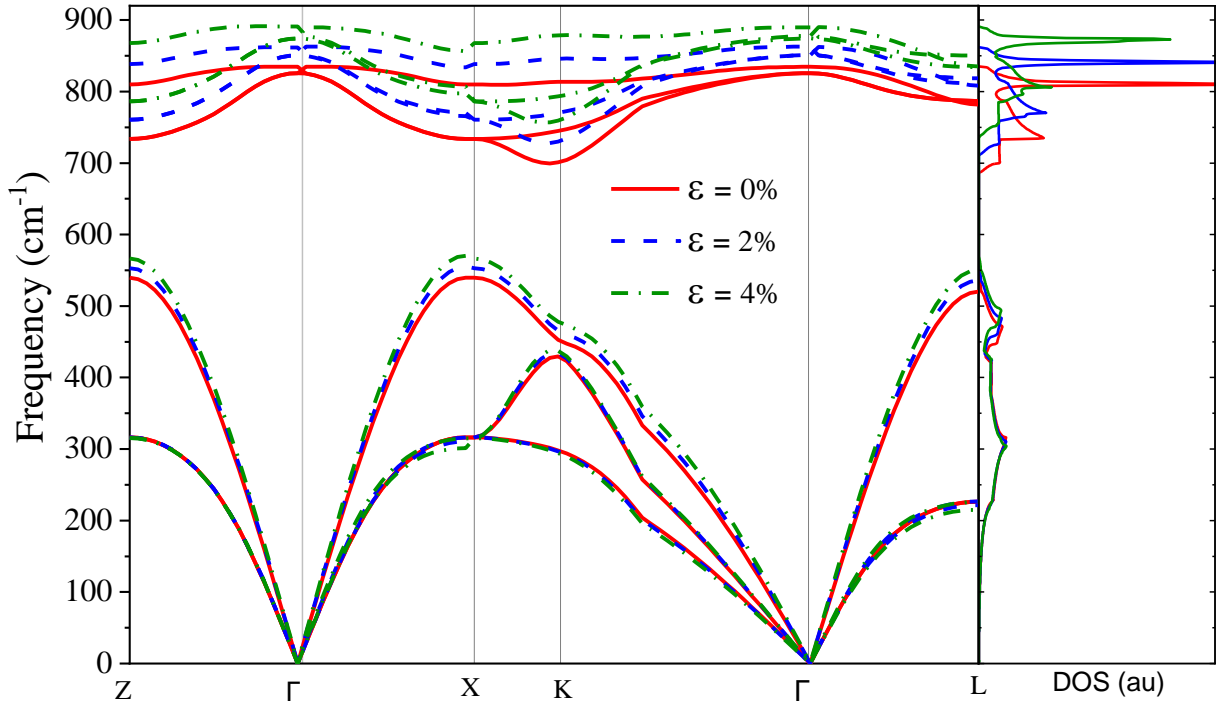


Figure 4.2: Phonon dispersion and density of states for the 0 %, 2 % and 4% strained BP

momentum conservation. These are given by $\omega + \omega' = \omega''$ (*energy*), $q + q' = q''$ (*momentum*) for absorption process and $\omega = \omega' + \omega''$ (*energy*), $q = q' + q''$ (*momentum*) for decay process. The first delta function in above equation, represents the absorption process, whereas the second delta function represents the decay process.

4.2 COMPUTATIONAL METHODS

DFT calculations were carried out using QUANTUM-ESPRESSO⁸⁸ using norm-conserving pseudopotentials in the local-density approximation (LDA) with a plane-wave cut off

100 Ry. Monkhorst k -point mesh of $12 \times 12 \times 12$ was used to describe the electronic properties. $8 \times 8 \times 8$ q -grid was used to compute the dynamical matrix and the 2nd order force constants. 3rd order (anharmonic) force constants were computed using D3Q⁸⁹⁻⁹¹ package, on a $4 \times 4 \times 4$ supercell. Acoustic sum rules were imposed on both 2nd and 3rd order force constants. Phonon linewidth and thermal conductivity calculations were carried out on $30 \times 30 \times 30$ q -mesh. For the exact solution of thermal conductivity, 50 iterations were carried out for the convergence.

Energy minimization was carried out for the unstrained cubic BP with respect to the lattice constant yielding a lattice parameter of $a = 8.44 \text{ \AA}$. The phonon dispersion along the high symmetry points⁹² for the unstrained case is shown in Fig. 4.2. The computed phonon frequencies are in good agreement with the experimental datasets obtained through x-ray scattering⁹³. For the strained cases, the lattice was compressed by 2% and 4% in the x-y plane (along both x and y directions) and relaxed in the z-direction (Fig. 1b). The lattice dimensions obtained after relaxing the structure corresponded to a Poisson ratio of $\nu = 0.19$, which is in good agreement with reported values.

4.3 RESULTS

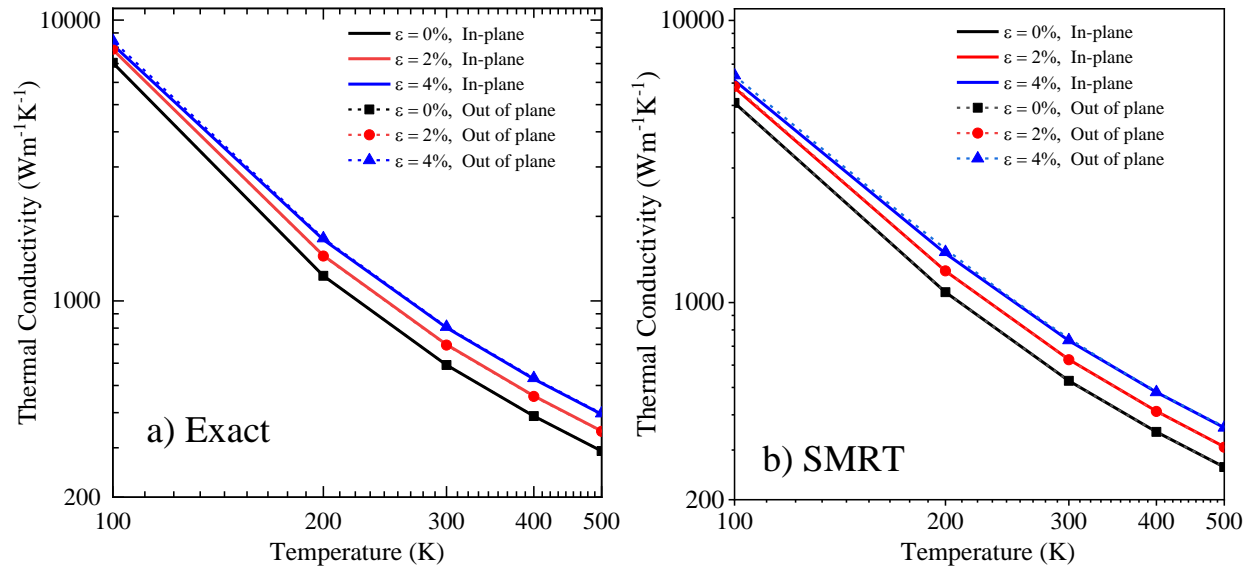


Figure 4.3: In-plane thermal conductivity of 0%, 2% and 4% strained boron phosphide using SMA relaxation method and iterative exact solution method.

4.3.1 Phonon dispersion and density of states

The phonon dispersions of unstrained and strained cases are compared in Fig. 4.2. It can

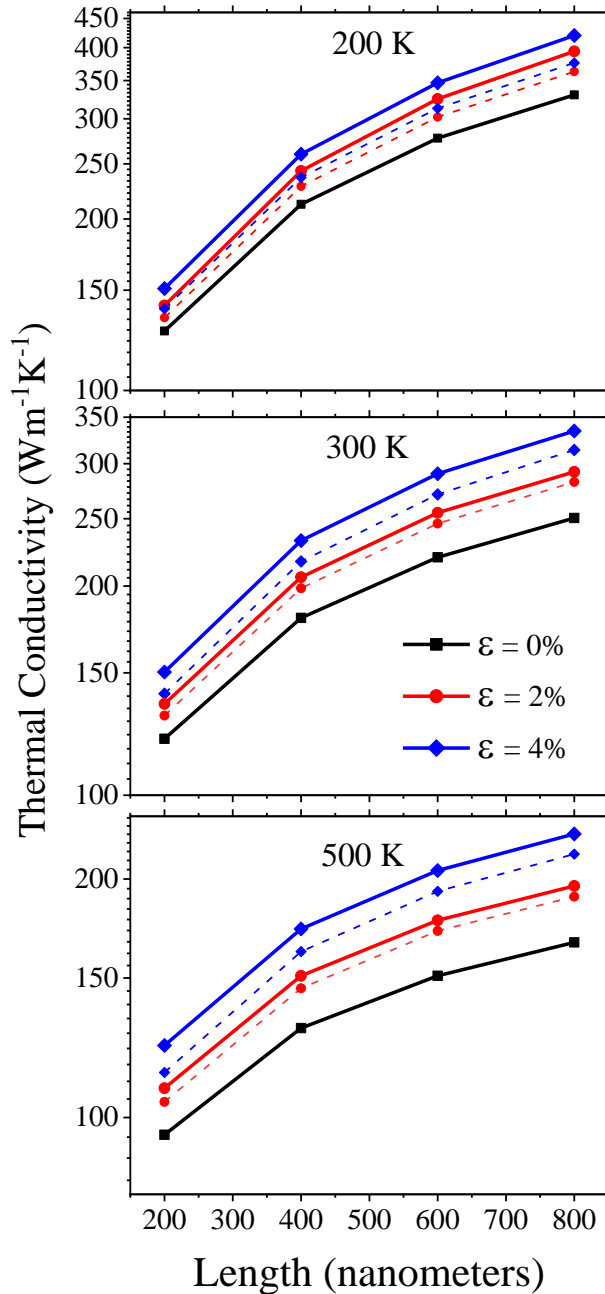


Figure 4.4: In-plane thermal conductivity of 0%, 2% and 4% strained boron phosphide using SMA relaxation method and iterative exact solution method.

be seen that as the lattice is biaxially compressed, phonon band gap between acoustic and optical phonons increases. For the unstrained boron phosphide, the phonon band gap is estimated to be 168 cm^{-1} , while for 2% and 4% compressive strains, the phonon band gap increases to 177 cm^{-1} and 186.5 cm^{-1} respectively representing an increase of 5.35% and 11.0% respectively.

4.3.2 Lattice thermal conductivity

Figs. 4.3 a and b show the thermal conductivity of unstrained, and 2% and 4% strained boron phosphide using an exact solution and single mode relaxation time (SMRT) approximation respectively. The computed k of unstrained BP is in good agreement with previously reported first-principles computations and measurements. Fig. 4.3 shows that in-plane (defined as the plane in which compressive biaxial strain is applied) k increases with increase in biaxial compressive strain. At 300K, while k of unstrained BP is computed to be 591 W/mK , the values for 2% and 4% strain are estimated to be 699 W/mK and 802.5 W/mK , representing an increase of 18.3% and 35.8% respectively. The value of 802.5 W/mK obtained for 4% strained BP is almost 5-times

the thermal conductivity of silicon ($k = 155$ W/mK at 300K), providing avenues to significantly enhance heat dissipation in electronic applications. Similarly, the out of plane k increases by 17.76% and 36.75% for the 2% and 4% biaxial strain respectively.

Length scale dependence of k was estimated by introducing additional Casimir scattering in the exact solution of PBTE. Fig 4.4. shows that biaxial strain leads to considerable increase in thermal conductivity at nanometer length scales. At length scale of 200 nm, an increase in k of 25% from 120.6 W/mK ($\epsilon=0\%$) to 150.4 W/mK ($\epsilon=4\%$) is observed at 300 K. At 400 nm, the increase in k is even higher, by almost 30%, from 180 W/mK to 232.5 W/mK for the same change in strain. The increase in nanoscale k is found to be higher at higher temperatures. At 500 K, out-of-plane k increases by 30% and 33% at 200 nm and 400 nm, respectively, for increase in strain from 0 to 4%. These large increases in nanoscale k point to the potential of applying biaxial strain for enhancement of nanoscale heat dissipation in electronic applications.

We first discuss increase in thermal conductivity for bulk BP (at infinite sample length), seen in Fig. 4.3. We find this increase in k to be due to a combination of decrease in phonon scattering and increase in phonon velocities. The two effects are not additive, and cannot be separated in magnitudes. However, by forcing the linewidths for all strains to be the same as for unstrained case, but using the actual velocities and frequencies, we find an increase in thermal conductivity of 10% for . Thus, an increase in velocities alone would have resulted in 10% increase in k , indicating that a decrease in scattering rates is the dominant effect. To understand this decrease in phonon scattering, we compare the scattering rates (phonon linewidths) for the acoustic modes of unstrained, and 2% and 4% biaxially strained BP in Fig. 4.5. We can observe that phonon linewidths (scattering rates) computed based on lowest order three-phonon scattering, decrease in strained BP, as the strain is increased from 0% to 4%. Figs. also show that the decrease in scattering is significant at 500 K and 300 K, however, as the temperature is decreased to 100 K, the change in scattering rates becomes diminished. To understand the decrease in phonon scattering at higher temperatures (exceeding ~ 300 K), we compare the scattering rates along Γ -X in Fig. 4.6. It is noted that upon applying strain, TA mode along Γ -X loses degeneracy, and splits into TA_1 (lower energy) and TA_2 (higher energy) modes. Here we only show TA_1 mode (behavior of TA_2 mode is similar). It can be seen (in Fig. 4.6b) that linewidth of TA mode decreases with increasing strain along entire Γ -X, while same holds true for LA mode for significant part of Γ -X (seen in Fig. 4.6a).

This decrease can be understood by looking at relevant scattering channels involved in the scattering of LA and TA modes (shown in Fig. 4.6c and d, respectively).

In particular we look at the magnitude of the following scattering channels (other channels were found to have negligible contribution to overall scattering rate) in the scattering of acoustic phonons - a) $a + o \rightarrow o$, b) $a + a \rightarrow o$, c) $a + a \rightarrow a$, and d) $a \rightarrow a + a$. We observe from Figs. 6c and d, that for large part of Γ -X, the most significant contribution to scattering of LA and TA phonons in BP is from the $a + a \rightarrow o$ scattering channel. In Figs. 4.6e and f, we compare the effect of strain on this dominant $a + a \rightarrow o$ (acoustic + acoustic \rightarrow optical) scattering channel for LA and TA modes, respectively. We observe a decrease in the magnitude of $a + a \rightarrow o$ channel for TA₁ mode with strain throughout Γ -X direction (Fig. 4.6f). Magnitude of $a + a \rightarrow o$ for TA₁ mode decreases by 16.1% and 28% for the 2% and 4% strain respectively at Brillouin zone edge (X-point). For LA phonon mode (Fig. 4.6e), we observe a reduction in magnitude of $a + a \rightarrow o$ channel for most part of Γ -X, except close to zone edge (X point), where an increase is observed.

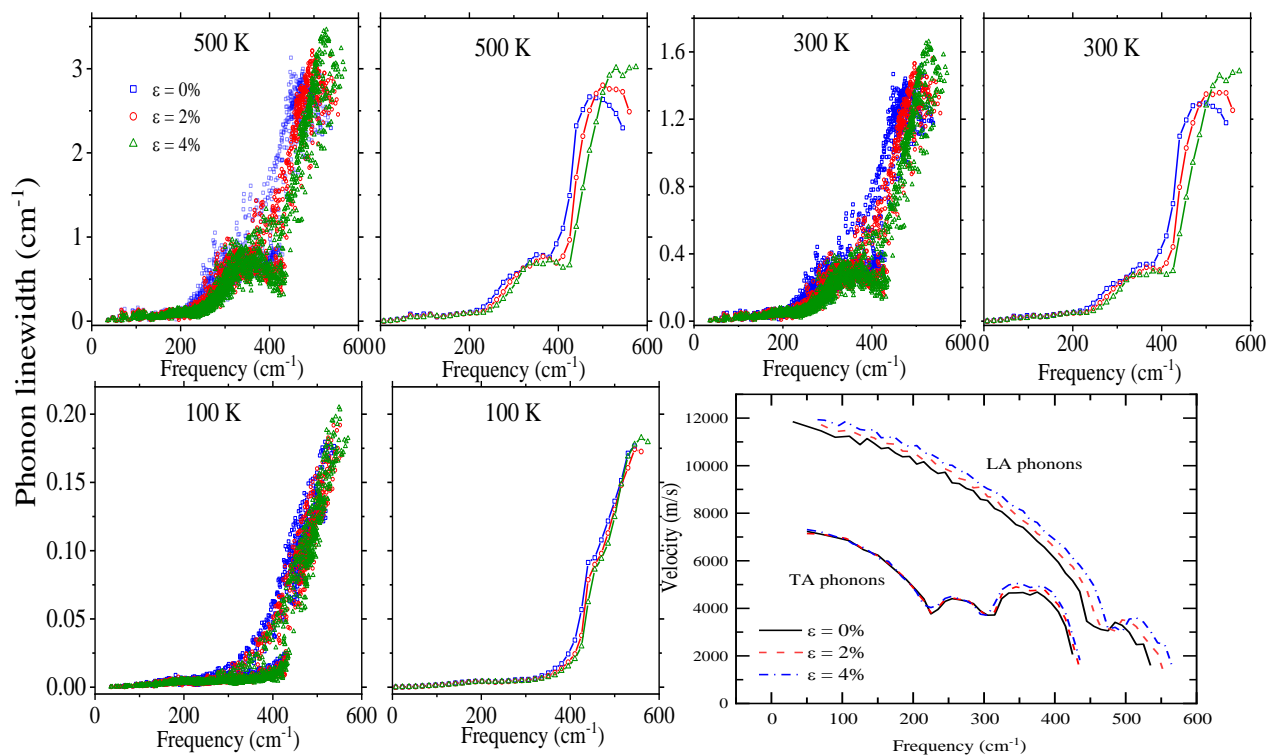


Figure 4.5 Phonon linewidth with strain at different temperature and phonon group velocity of TA and LA phonons

This observed decrease in $a + a \rightarrow o$ scattering channel strength for most of the Brillouin zone, is a direct consequence of increase in phonon band gap between acoustic and optical phonons (seen in Fig. 4.3). This is seen by considering that in unstrained case, a TA acoustic phonon of frequency $\omega=158 \text{ cm}^{-1}$ can scatter by absorbing an LA (acoustic) phonon of frequency $\omega'=532 \text{ cm}^{-1}$, yielding

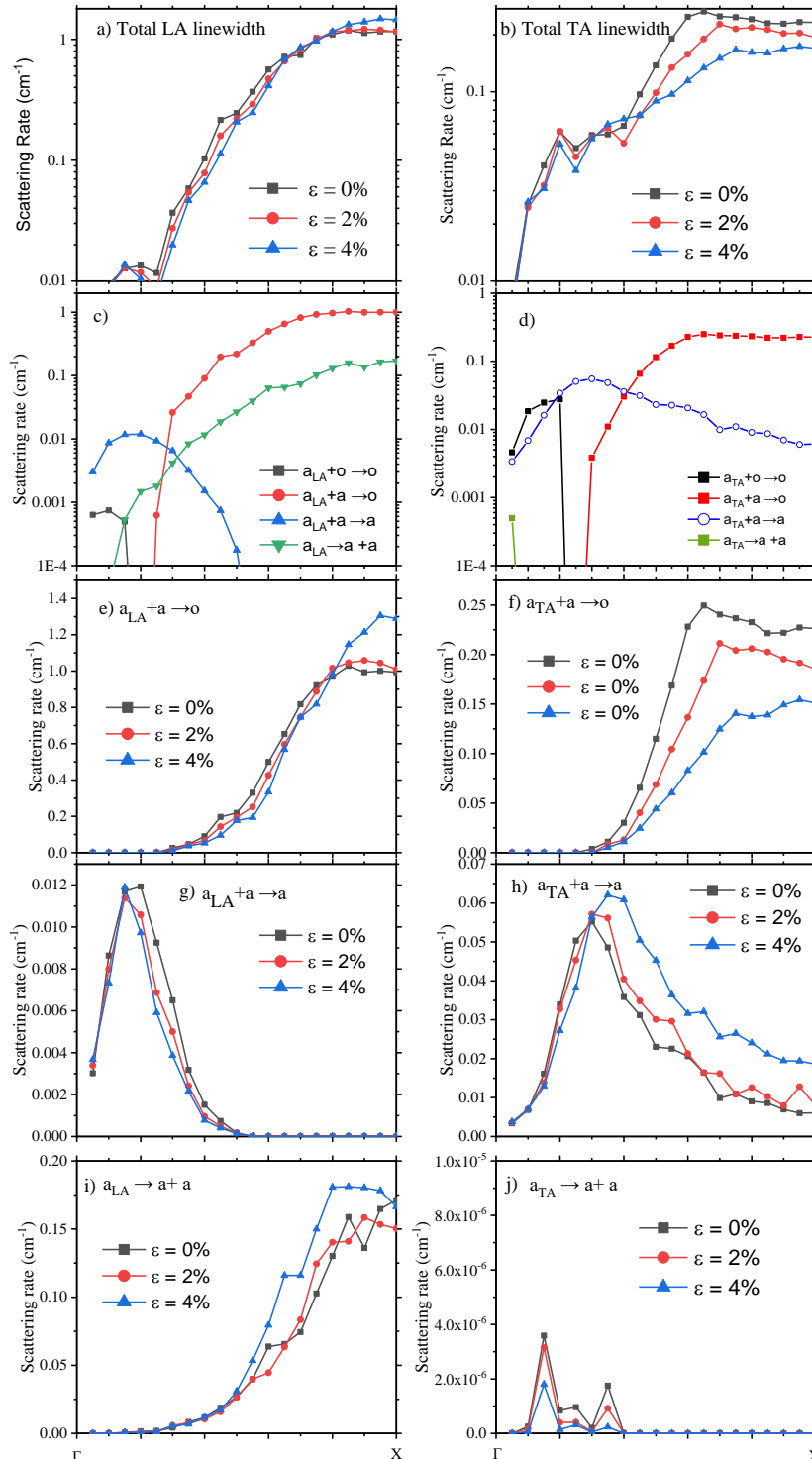


Figure 4.6a: Dominant scattering mechanisms in boron phosphide of LA phonon mode 4.6b. TA phonon mode modes for different strain rate along Γ -X direction. 4.6c and d : Total scattering rate due to all possible scattering for LA and TA phonon mode respectively for different strain rate. 4.6e: Scattering due to $a + a \rightarrow o$ for LA phonon modes for different strain rates. 4.6f: Scattering due to $a + a \rightarrow o$ for TA_1 phonon modes with different strain rate.

the lowest energy optical phonon of frequency $\omega''=690 \text{ cm}^{-1}$ ($\omega+\omega'=\omega''$) (provided the appropriate momentum conservation is satisfied). In the 2% strained case, however, due to the increase in phonon band gap, this scattering channel becomes prohibited, since the optical phonon frequencies become higher than 690 cm^{-1} . Minimum optical phonon frequency ($\omega_{min,optical''}$) in 2% strained case is 711.9 cm^{-1} , causing sum of $\omega_{acoustic}$ (158 cm^{-1}) and $\omega_{acoustic}'$ (532 cm^{-1}) to become less than $\omega_{min,optical''}$ (711.9 cm^{-1}) ($\omega_{acoustic} + \omega_{acoustic}' < \omega_{min,optical''}$), thus making energy conservation for such $a + a \rightarrow o$ channels, infeasible. This causes such $a + a \rightarrow o$ channels (which were feasible in unstrained BP) to become completely forbidden in the strained case. Removal of $a + a \rightarrow o$ scattering channels diminishes scattering of TA phonons by optical phonons in the strained Boron-Phosphide along entire Γ -X, enhancing TA phonon lifetimes. Same decrease in $a + a \rightarrow o$ scattering also occurs for LA phonons.

However, for LA phonons, an increase in $a + a \rightarrow o$ scattering is also observed near the Brillouin zone edge. This can be explained by a shift of the optical phonon frequencies to higher values in strained BP as seen in phonon dispersion in Fig. 4.2. As an example, in the 2% biaxially strained BP, an LA phonon of frequency $\omega=500 \text{ cm}^{-1}$ can scatter by absorbing another LA phonon of frequency $\omega'=340 \text{ cm}^{-1}$, yielding optical phonon of frequency $\omega''=840 \text{ cm}^{-1}$ ($\omega+\omega'=\omega''$), (provided the appropriate momentum conservation is satisfied). Presence of higher frequency optical phonons in strained BP (spanning frequency range of $711 \text{ cm}^{-1} - 848 \text{ cm}^{-1}$) makes such a channel feasible in the 2% strained BP, since $\omega''=840 \text{ cm}^{-1}$ lies within the optical frequency range of strained BP. In the unstrained case, however, optical phonon

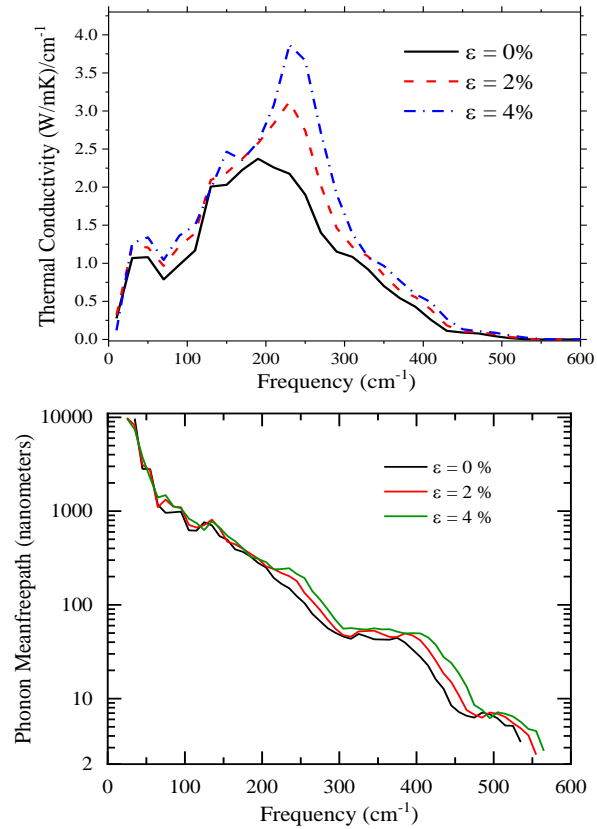


Fig. 4.7a: Spectral dependence of thermal conductivity in strained Boron Phosphide at 300 K. b) Phonon mean freepath of BP with strain

frequencies are lower ($690 \text{ cm}^{-1} - 820 \text{ cm}^{-1}$), and an optical phonon of frequency $\omega''=840 \text{ cm}^{-1}$ does not exist, making the above channel infeasible in unstrained case. The presence of additional scattering channels for higher energy LA phonons near the zone edge (in strained BP), increases their linewidths in strained case.

We also find a small increase in $a_{LA} \rightarrow a + a$ scattering for LA modes, and $a_{TA} + a \rightarrow a$ scattering for TA modes in strained BP. However, magnitudes of these channels are significantly smaller, than $a + a \rightarrow o$ channel; decrease in $a + a \rightarrow o$ scattering of both LA and TA phonons, then, results in a decrease in overall scattering rate, resulting in the observed increase in thermal conductivity of strained Boron-Phosphide.

Competing mechanisms, with decreasing and increasing contributions (discussed above) to $a + a \rightarrow o$ channel for LA phonons, cause smaller overall decrease in scattering of LA phonons compared to TA phonons.

We next address the enhancement in nanoscale thermal conductivity in strained BP, by first studying the spectral dependence of thermal conductivity in strained BP. Fig. shows that peak contribution to thermal conductivity in strained BP is made by phonons of higher frequencies ($\sim 240 \text{ cm}^{-1}$) than in the case of unstrained BP ($\sim 240 \text{ cm}^{-1}$). This shift of peak k to higher frequencies, can be understood by noticing that the decrease in $a + a \rightarrow o$ scattering (that drives overall scattering) is dominant at higher wavevectors ($q > 0.2$ along G-X) and thus leads to a decrease in overall scattering rate at higher frequencies ($> 200 \text{ cm}^{-1}$ as seen in Fig. 4.3). At small wavevectors, the $a + a \rightarrow o$ channel is almost completely absent, as the frequencies of these acoustic phonons are too small to scatter in to the higher energy optical phonons. As frequency of acoustic phonon increases, it becomes large enough to enable absorption of another acoustic phonon, such that the sum is a high energy optical phonon, causing the $a + a \rightarrow o$ channel to be dominant at higher frequencies. The elimination of this channel in strained BP due to increase in optical phonon frequencies, thus leads to larger decrease in overall scattering at higher frequencies ($> 200 \text{ cm}^{-1}$). This decrease in phonon scattering at higher frequencies of $> 200 \text{ cm}^{-1}$ combined with a very large phonon density of states near 250 cm^{-1} , leads to peak thermal conductivity shifting to 250 cm^{-1} . The effect is also found to lead to a spectral focusing of thermal conductivity in strained BP.

The enhancement in thermal conductivity at nanoscale can be understood by comparing phonon meanfreepaths in strained BP relative to unstrained case at different frequencies as shown in Fig. 4.7b shows that there is an increase in phonon meanfreepaths at higher frequencies in

strained BP where meanfreepaths are in the nanometer range. This increase in meanfreepaths at higher frequencies is a direct consequence of the decrease in $a + a \rightarrow o$ scattering at these frequencies. In unstrained BP, meanfreepaths are seen to decrease as frequency increases. However, in strained BP, decrease in $a + a \rightarrow o$ scattering at frequencies exceeding $\sim 200 \text{ cm}^{-1}$ slows down this rate of decrease in meanfreepaths, resulting in a plateauing (flattening) of the meanfreepath behavior with respect to frequency at meanfreepaths around 200nm. This increases the number of phonons at meanfreepaths in the $\sim 100 \text{ nm}$. This increase in phonon density at nanometer freepaths, increases thermal conductivity at nanometer length scale. Finally, it is noted that thermal conductivities in this work are computed based on the lowest order three-phonon scattering. Role of four-phonon processes was shown to be minimal in BP in a recent work.

4.4 CONCLUSION

By deriving harmonic and anharmonic interatomic force interactions, from density functional theory and using them along with an exact solution of the Boltzmann transport equation, we have provided a microscopic description of thermal transport in biaxially strained Boron Phosphide. Thermal conductivity of 4% biaxially compressed Boron-Phosphide (BP) is computed to be 802.5 W/mK at 300 K. This value is almost 35.8% higher than the value of 591 W/mK, computed for unstrained BP, and almost 5-fold the thermal conductivity of silicon (Si). Above enhancement in thermal conductivity is found to be due a decrease in scattering of acoustic phonons, mediated by an increase in phonon band gap in strained BP, which suppresses *acoustic + acoustic* \rightarrow *optical* scattering channel, the dominant scattering channel in unstrained BP. A shift in spectral dependence of thermal conductivity is also observed in strained BP. While in unstrained BP, peak contribution to thermal conductivity occurs from phonons with frequencies less than 200 cm^{-1} , in 4% strained BP, peak contribution shifts to higher frequencies of $\sim 250 \text{ cm}^{-1}$. Finally, we find that biaxially strained BP exhibits superior heat conduction at nanometer length scales. In unstrained BP, phonons of meanfreepaths lower than 600 nm have a thermal conductivity contribution of 248 W/mK, while for 2% and 4% strain case, this value increases to 290 W/mK and 330 W/mK. These results have important implications for improving thermal management in nano-scale applications.

CHAPTER 5: STRAIN TUNED THERMAL CONDUCTIVITY REDUCTION IN INDIUM ARSENIDE(InAs) – A FIRST PRINCIPLES STUDY

Thermoelectric (TE) materials, which are capable of converting heat into electric current through Seebeck effect, draw significant attention among researchers due to the eco-friendly energy conversion⁹⁴⁻⁹⁶. The efficiency of a thermoelectric material is expressed by dimensionless figure of merit ($ZT = \sigma S^2 T / k$), where σ is the electrical conductivity, S is the Seebeck coefficient, T is the temperature and k is the thermal conductivity⁹⁷. High ZT can be obtained by either increasing the power factor (σS^2)^{98,99} or by minimizing lattice thermal conductivity^{100,101}. Over the years, several materials have been reported with high thermoelectric performance such as PbTe¹⁰², SnSe¹⁰³, Bi₂Te₃¹⁰⁴, PbS and SiGe alloys¹⁰⁵. PbTe and PbS are used as thermoelectric materials because of their very good electrical conductivity and low thermal conductivity^{106,107}. The key strategy to improve figure of merit without affecting electrical conductivity and Seebeck coefficient is to reduce the lattice thermal conductivity. Thermal conductivity can be reduced by introducing disorder which leads to increase in phonon scattering. Strain engineering is another promising approach to modify thermal conductivity by controlling the phonon bandgap between acoustic and optical phonons. In a recent work, increase in thermal conductivity of BP is reported through

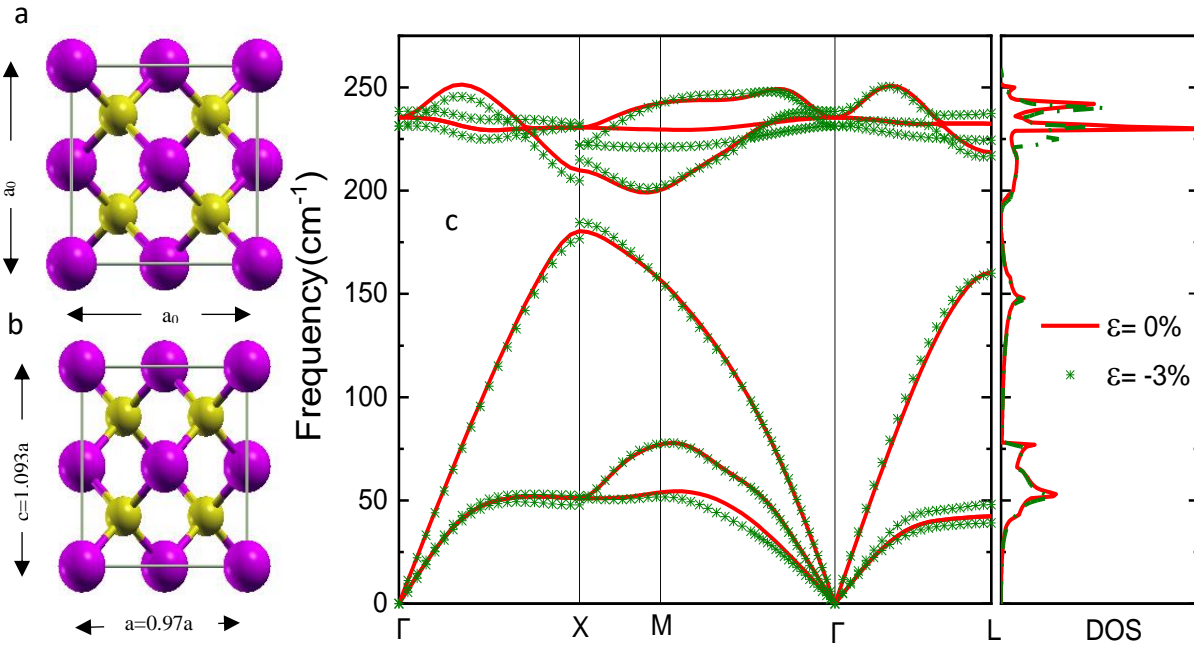


Figure 5.1: Indium Arsenide with a) 0% and b) 3% strain c) Phonon dispersion and density of states for unstrained and 3% biaxially compressed InAs.

biaxial compressive strain⁸¹. Increase and decrease in thermal conductivity of wurtzite gallium nitride have been reported for 5% biaxial compression and biaxial tension respectively⁷⁹. Effects of biaxial strain on thermal conductivity modulation is yet to be explored for thermoelectric materials.

Indium Arsenide (InAs) is a direct band gap semiconductor with high electron mobility and is used for field effect transistors, quantum-well structures, and substrate for magnetic field sensors, lasers and detectors because of its large Hall coefficient^{108, 109}. Indium Arsenide based thermoelectric materials^{110, 111} with a power factor of 10^{-3} W/mK² were observed over a temperature range of 300 to 600 K. An order of increase in power factor was observed at 20K in InAs nanowires¹¹². In this work¹¹³, we report 20% reduction in in-plane thermal conductivity of InAs through 3% biaxial compressive strain. Reduction in thermal conductivity is due to increase in phonon scattering rate and decrease in phonon group velocities of both TA and LA phonons.

5.1 COMPUTATIONAL METHODS

Cubic InAs was relaxed until the residual stress and forces acting on the atoms became zero. The computed equilibrium lattice constant of 5.967 Å is in good agreement with the previously reported first-principles values¹¹⁴. A Monkhorst k -point mesh of 12 x 12 x 12 was used to describe the electronic properties during self-consistent calculations¹¹⁵. To compute the dynamical matrix and 2nd order force constants, an 8 x 8 x 8 q-grid was used. 4 x 4 x 4 q-grid was

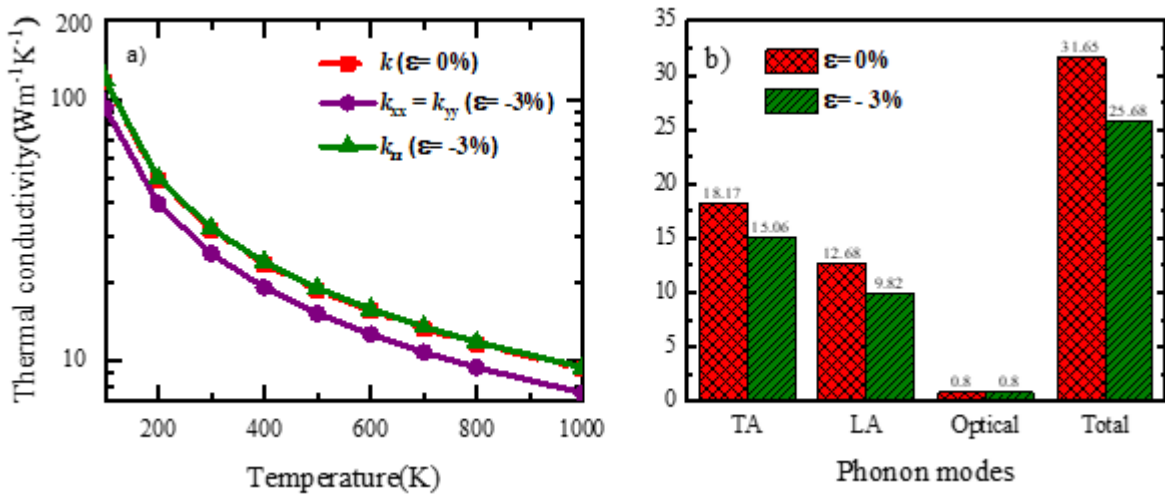


Figure 5.2: a) In-plane and out-of-plane thermal conductivity of 0%, 3% biaxially compressed InAs b) TA, LA and optical phonon mode contribution to overall thermal conductivity.

used to compute the 3rd order force constants using QUANTUM ESPRESSO D3Q^{89, 90} package. Acoustic sum rules were imposed on both 2nd and 3rd order force constants. Phonon group velocities, frequencies and Bose-Einstein populations were calculated using 2nd order force constants and phonon lifetimes were calculated using both 2nd and 3rd order interatomic force constants. 30 x 30 x 30 q-mesh was used to calculate phonon linewidths and thermal conductivity and the solution of Boltzmann transport equation was found to be converged after 8 iterations.

5.2 RESULTS

5.2.1 Phonon dispersion

Phonon dispersions for the unstrained and 3% biaxial strained InAs are compared in figure 6.1. We can observe changes in phonon band gap between acoustic and optical phonons. Phonon band gap for the unstrained InAs is 18.65 cm⁻¹, while for 3% biaxially strained case, it was found to be reduced by 11.62% to 16.48 cm⁻¹.

5.2.2 Lattice Thermal conductivity

Lattice thermal conductivity of InAs was calculated by solving Boltzmann transport equation (BTE) using both single mode relaxation approximation and exactly using iterative solution¹¹⁶. For convenience, we have shown only the exact solution in Fig 5.2a. The computed values are shown in Fig 5.2a and are in good agreement with the previously reported¹¹⁷ first principles calculations for unstrained InAs. At 300 K, thermal conductivity (k) of unstrained InAs is 33.85 Wm⁻¹K⁻¹ which is reduced to 27 Wm⁻¹K⁻¹ along in-plane direction (a decrease of 20.23%).

Fig 5.2b shows the mode contribution of TA, LA and optical phonons to overall thermal conductivity. We can observe a reduction in thermal conductivity in both TA and LA phonon modes with strain. With 3% biaxial compressive strain, thermal conductivity (k) of TA phonon mode contribution drops from 18.17 Wm⁻¹K⁻¹ to 15.06 Wm⁻¹K⁻¹ and LA phonon mode drops from 12.68 Wm⁻¹K⁻¹ to 9.82 Wm⁻¹K⁻¹. Optical phonon modes have less than ~2.5% contribution to overall thermal conductivity. To understand this reduction in thermal conductivity, we compare the phonon linewidths (inverse of phonon lifetime) and phonon group velocities of TA and LA phonon modes, as shown in Fig 5.3a and b respectively. From 5.3a we can observe an increase in phonon scattering rates of both TA and LA phonon modes with 3% biaxial compressive strain. In Fig 5.3b, a small reduction in phonon group velocity of LA phonons is observed. Hence, k

reduction of both TA and LA phonons are due to the combined effect of increase in phonon scattering rate and decrease in phonon group velocity.

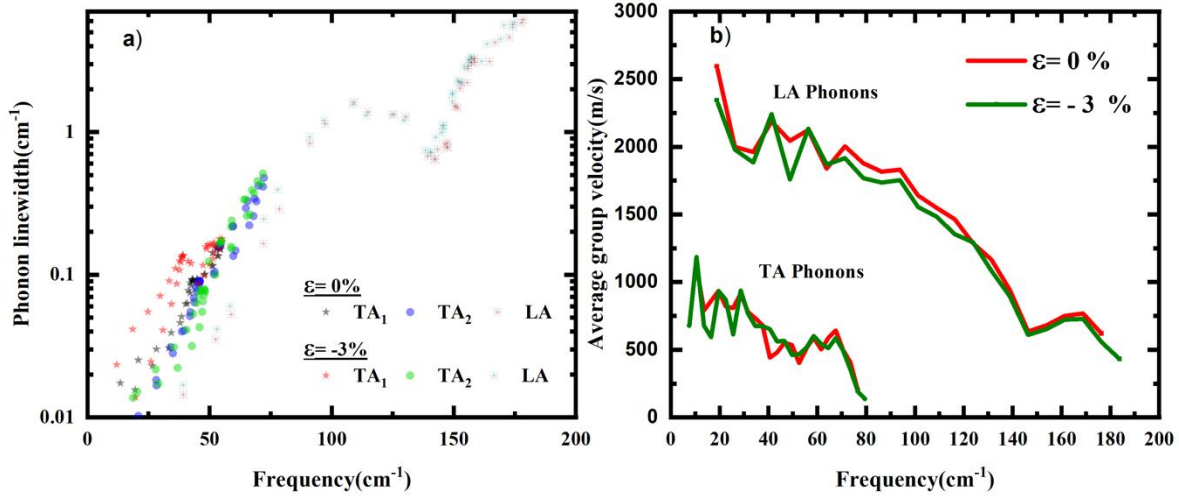


Figure 5.3 a) Phonon linewidth (inverse of lifetime) and b) average phonon group velocity of InAs with 0% and 3% strain

Intrinsic three-phonon anharmonic phonon scattering can be categorized into absorption and decay processes. During the absorption process, a phonon mode ($q\omega$) scatters by absorbing another phonon mode ($q'\omega'$) and yielding a higher energy phonon mode ($q''\omega''$). During the decay process, a phonon mode ($q\omega$) decays into two lower energy phonons. Both absorption and decay processes satisfy energy and momentum conservation. For example, an absorption process has to satisfy both energy ($\omega + \omega' = \omega''$) and momentum ($q + q' = q''$) conservation. Similarly, decay process has to satisfy energy ($\omega = \omega' + \omega''$) and momentum ($q = q' + q''$) conservation.

Figure 5.4a and b represent the total scattering rate of TA and LA mode for unstrained and strained cases along Γ -X. For the 3% biaxial compressive strain, we can observe an increase in total scattering rate of TA phonons throughout Γ -X. To elucidate this increase in TA phonon modes, we have analyzed the dominant scattering channels of TA phonon modes as shown in Fig 5.4c. Figure 5.4c and d represent all the possible phonon scattering channels of TA and LA phonon mode for unstrained InAs such as, a) an acoustic mode decaying into two acoustic phonons ($a \rightarrow a + a$), b) an acoustic phonon absorbing an optical phonon to yield higher energy optical phonon ($a + o \rightarrow o$), c) an acoustic phonon absorbing another acoustic phonon yielding higher energy optical phonons ($a + a \rightarrow o$) and d) an acoustic phonon absorbing another acoustic phonons yielding a higher energy acoustic phonon ($a + a \rightarrow a$).

From Fig 5.4c, we can observe that, the dominant phonon scattering channels of TA modes are

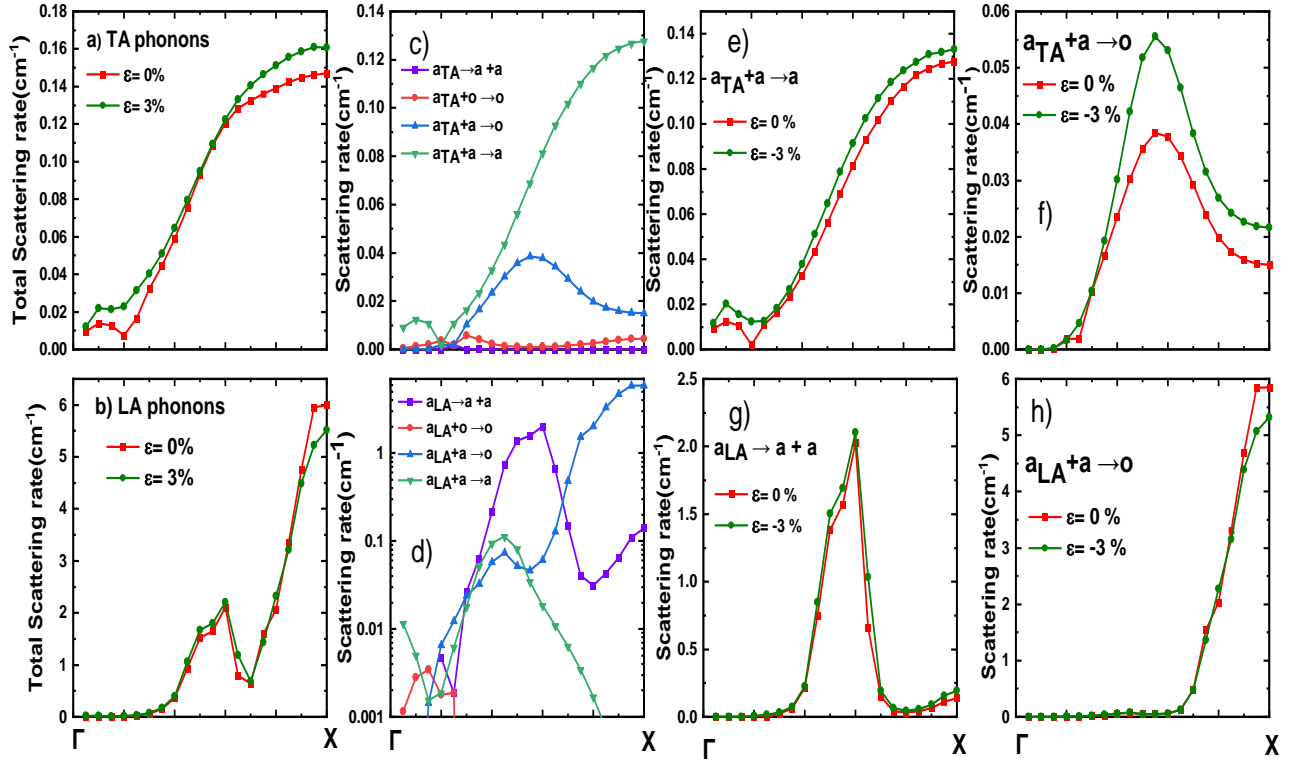


Figure 5.4: a) and b) Total scattering rate of TA and LA phonon modes, respectively, c) and d) dominant scattering channels of TA and LA phonon modes, respectively, e) and f) scattering of TA phonon modes due to $a+a \rightarrow a$ and $a+a \rightarrow o$, respectively, g) and h) scattering of LA phonons due to $a \rightarrow a+a$ and $a+a \rightarrow o$ respectively for the 0% and 3% biaxial compressive strained InAs.

$a+a \rightarrow a$ and $a+a \rightarrow o$. The scattering rates of both these modes increase with applied strain (shown in Fig 5.4e and f). At $q = 0.55$ (reduced units) along Γ -X, scattering due to $a+a \rightarrow o$ mode is found to increase by 50%. Dominant scattering channels for LA phonons are $a+a \rightarrow o$ and $a \rightarrow a+a$ (Fig. 5.4d). The effect of strain on these channels is shown in 5.4g and f. k reduction of LA phonons is due to the combined effect of reduction in phonon group velocities and increase in phonon scattering.

5.3 CONCLUSION

Using first-principles calculations and by solving Phonon Boltzmann Transport Equation iteratively, we have studied the thermal transport in biaxially strained Indium Arsenide (InAs).

Thermal conductivity (k) of 3% biaxial compressively strained InAs reduced by ~20 % along in-plane direction. Phonon group velocity and phonon scattering rate of TA and LA phonon modes upon strain were investigated and our first principles calculations reveal that reduction in k is due to a combination of increase in phonon scattering rate and decrease in phonon group velocity of both TA and LA phonons. These results provide an avenue for improving the thermoelectric performance by reducing the lattice thermal conductivity through biaxial strain.

**CHAPTER 6: STRAIN TUNED LOW THERMAL CONDUCTIVITY IN INDIUM
ANTIMONIDE(InSb) THROUGH INCREASE IN ANHARMONIC SCATTERING – A
FIRST PRINCIPLES STUDY**

Indium Antimonide (InSb) is a promising candidate material for thermoelectric applications¹¹⁸⁻¹²⁰ because of its high mobility of electrons of about 10^4 - 10^5 $\text{cm}^2\text{V}^{-1}\text{s}^{-1}$ and bandgap of about 0.18 eV¹²¹. The performance of a thermoelectric material can be expressed by the dimensionless figure of merit, $ZT = \sigma S^2 T / k$, where σ , S , T and k are the electrical conductivity, Seebeck coefficient, absolute temperature and thermal conductivity respectively. Thermoelectric performance of InSb can be increased by increasing the power factor (σS^2)^{99, 122} and reducing lattice thermal conductivity^{100, 123}. Various strategies such as disorder^{87, 124}, nano structuring^{125, 126}, strain⁷⁹ and defects^{127, 128} can be used to reduce the lattice thermal conductivity. In this work¹²⁹, we report 29% and 17% reduction in in-plane (plane in which compressive biaxial strain is applied) and out-of-plane thermal conductivity of cubic InSb through 5% biaxial compressive strain. This decrease in k is found to be due to a large increase in three-phonon scattering rates of LA phonons driven by a shift of TA frequencies to lower values. Simultaneously TA phonon scattering rates also increase mediated by an increase in absorption scattering channels in strained InSb. First-principles computations are used to present understanding of the role of strain in modifying

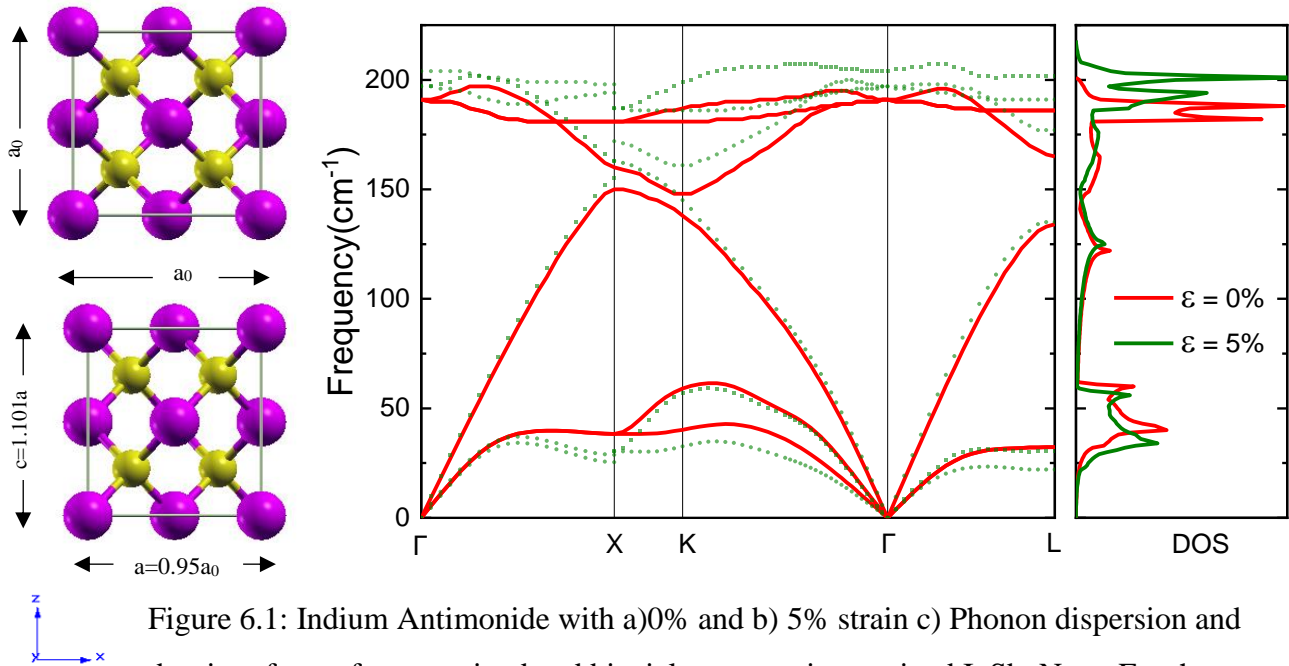


Figure 6.1: Indium Antimonide with a)0% and b) 5% strain c) Phonon dispersion and density of state for unstrained and biaxial compressive strained InSb. Note: For the purpose of comparison, we plotted along the same direction.

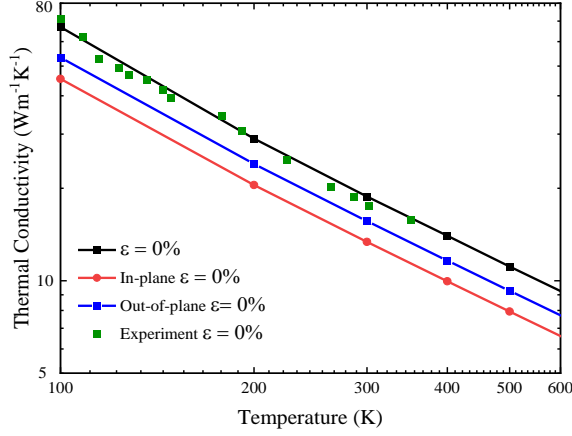


Figure 6.2: Computed in-plane and out-of-plane thermal conductivity of unstrained and 5% biaxially compressed InSb.

scattering rates in strained InSb. These results have important implications for high efficiency thermoelectric materials.

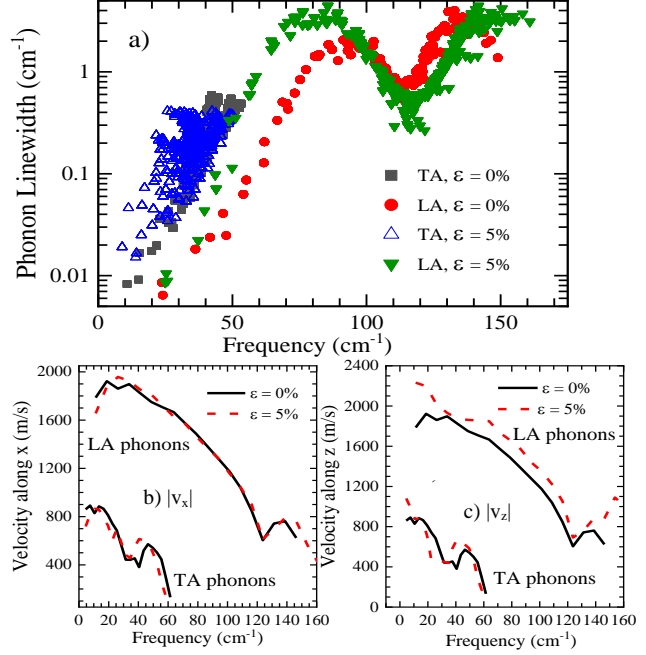


Figure 6.3: Comparison between unstrained and strained InSb of a) Phonon linewidths at 300 K b) mean velocity in in-plane x -direction and c) mean velocity in out-of-plane z -direction.

6.1 COMPUTATIONAL DETAILS

DFT calculations were carried out using QUANTUM-ESPRESSO⁸⁸. Norm-conserving pseudopotentials in the local-density approximation (LDA) were used with a plane-wave cut-off of 100 Ry. Monkhorst¹¹⁵ k -point mesh of $12 \times 12 \times 12$ was used to describe the electronic properties. $9 \times 9 \times 9$ q -grid was used to compute dynamical matrices and the 2nd order IFCs. 3rd order IFCs were computed using D3Q⁹⁰ package, on a $3 \times 3 \times 3$ q points. Acoustic sum rules were imposed on both 2nd and 3rd order force constants. Phonon linewidth and k calculations were carried out on $40 \times 40 \times 40$ q -mesh and smearing of 0.05 cm^{-1} . For the exact solution of PBTE, typically 10 iterations were found to be sufficient to achieve convergence⁹¹.

6.2 RESULTS

6.2.1 LATTICE PARAMETER and THERMAL CONDUCTIVITY

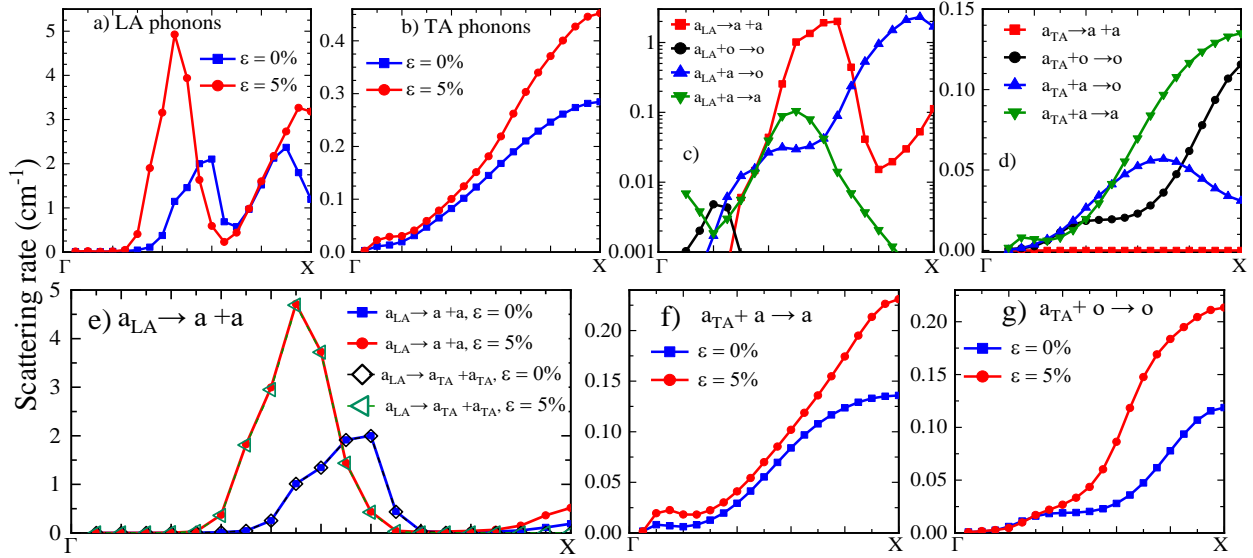


Figure 6.4: Comparison of unstrained and strained InSb in terms of total scattering rate at 300 K along Γ -X of a) LA and b) TA phonon modes. Contribution of dominant scattering channels at 300 K in unstrained InSb for c) LA and d) TA phonons. Comparison between unstrained and strained InSb of e) $a_{LA} \rightarrow a + a$ channel, f) $a_{TA} + a \rightarrow a$ channel and g) $a_{TA} + o \rightarrow o$ channel at 300 K.

Lattice parameter of unstrained InSb was determined through energy minimization to be $a_0 = 6.389 \text{ \AA}$. For the strained cases, the lattice was compressed by 5% in the x - y plane (along both x and y directions) and relaxed in the z -direction. The lattice dimensions of the biaxially strained InSb are computed to be $a = b = 0.95a_0$, and $c = 1.108a$. Computed phonon dispersion for unstrained (which is in good agreement with the experimental measurements²⁴) and strained case is shown in Fig 1. Strain is found to shift TA phonon frequencies to lower values (seen also a shift in phonon density of states) while leading to an increase in LA phonon frequencies.

At 300K, thermal conductivity of unstrained InSb is computed to be $18.83 \text{ Wm}^{-1}\text{K}^{-1}$ (Fig. 6.2), in good agreement with measurements¹³⁰. Upon biaxial compression, k is reduced to $13.38 \text{ Wm}^{-1}\text{K}^{-1}$ and $15.62 \text{ Wm}^{-1}\text{K}^{-1}$ along in-plane and out-of-plane directions, representing a reduction of 29% and 17%, respectively. To understand this reduction and anisotropy in k in strained InSb, we analyze the effect of strain on phonon group velocities and scattering rates in Fig. 6.3.

Fig. 6.3a shows large increase in scattering rates of acoustic phonons in strained InSb, particularly for the LA phonons. At a frequency of $\sim 70 \text{ cm}^{-1}$, the scattering rate of LA phonon for example, increases by nearly a factor of 5 from $\sim 0.5 \text{ cm}^{-1}$ to $\sim 2.5 \text{ cm}^{-1}$, at 300 K. Scattering rates of TA phonons also increase in strained InSb, however, the increase is smaller than for LA phonons. Mean phonon velocities, along the in-plane direction (plane in which bi-axial strain is applied), however, are found to remain almost the same for unstrained and strained InSb (Fig. 6.3b). Decrease in in-plane k in strained InSb is, therefore, primarily due to an increase in scattering rates. Along the, out-of-plane direction, an increase in phonon velocities of LA phonons in strained InSb (Fig. 6.3c), partially cancels the effect of increase in scattering rates, leading to lower decrease in k along this direction.

6.2.2 INCREASE IN LA PHONON SCATTERING

To understand increase in phonon scattering in strained InSb, we analyze the scattering rates of LA and TA phonons along Γ -X in Fig. 6.4. A large increase of 330% in scattering rate of LA phonon is observed in strained InSb at wavevectors close to the middle of the Brillouin zone (at $q_x = 0.45$) in Fig. 6.4a. Fig. 6.4c shows that a dominant contribution to scattering of LA phonons is from the $a \rightarrow a + a$ channel which represents decay of an acoustic phonon into two lower frequency acoustic phonons. The scattering rate for the $a \rightarrow a + a$ channel is found to peak with respect to wavevector for unstrained InSb at $q_x=0.60$ (Fig. 6.4e); in strained InSb, the scattering rate for this channel increases at lower wave-vectors, seen also as a shift in peak scattering rate to lower wavevector of $q_x=0.45$. The peak scattering rate for $a \rightarrow a + a$ channel for LA phonons

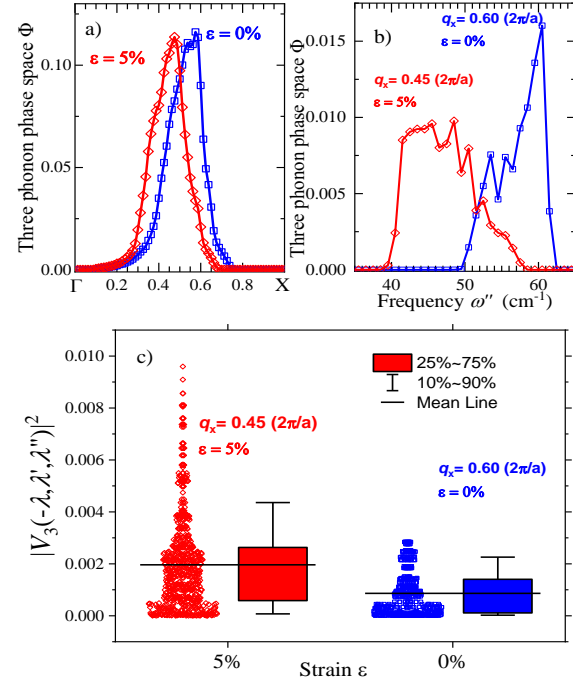


Figure 6.5: a) Phase space for scattering of LA phonons in strained and unstrained InSb b) phase space for scattering of LA at different frequencies and c) Comparison of three-phonon coupling elements in strained and unstrained InSb.

increases significantly in magnitude in strained InSb, by almost a factor of 2 relative to peak in unstrained InSb (Fig. 6.4e).

Fig. 6.1 shows that strain shifts TA phonons to lower frequencies. Above increase in scattering rate of mid-Brillouin zone LA phonons is found to be due to this decrease in TA frequencies, through two important effects – a) an increase in number of decay scattering channels and b) an increase in magnitude of three-phonon coupling elements, as described next. We first describe increase in number of decay channels for LA phonons at mid-Brillouin zone wave-vectors. To understand this increase, it is realized that scattering rate of $a_{LA} \rightarrow a + a$ channel is almost entirely due to decay of LA phonons in to two TA phonons, i.e the $a_{LA} \rightarrow a_{TA} + a_{TA}$ channel, as seen in Fig. 4e. Decrease in TA phonon frequencies in strained InSb (Fig. 6.1), increases the probability of scattering of lower frequency LA phonons in to these larger number of TA phonons now available at lower frequencies, leading to an increase in number of $a_{LA} \rightarrow a_{TA} + a_{TA}$ scattering (decay) channels, for low frequency (mid Brillouin zone) LA phonons in strained InSb.

To show this increase clearly, we define scattering phase space Φ for the $a_{LA} \rightarrow a_{TA} + a_{TA}$, as $\Phi = 1/(4N) \sum_{\lambda'} \delta(\omega_{LA}(q) - \omega_{TA}(q') - \omega_{TA}(q'' = q - q'))$, N is the size of the q' mesh used for summation (summation is performed only over the TA modes). The phase space as defined above, is indicative of the number of decay scattering channels contributing to the magnitude of $a_{LA} \rightarrow a_{TA} + a_{TA}$ channel (the definition essentially assumes all of the three-phonon coupling elements to be unity, and ignores absorption processes in Equation 4.2). Fig. 6.5a shows an increase in scattering phase space for LA phonons at smaller wavevectors (lower frequencies) in strained InSb (Fig. 6.5a). While peak phase space for unstrained InSb occurs at $q_x \sim 0.60$, this peak shifts to lower wavevector of $q_x \sim 0.45$ in strained InSb. At wavevector $q_x=0.45$, phase space for scattering of LA phonon in strained InSb is almost 55% higher, relative to the case of unstrained InSb (Fig. 6.5a).

To see that this increase in phase space for lower frequency LA phonons is directly due to shift of TA frequencies to lower values, we show distribution of TA phonon frequencies contributing to the scattering phase space for $a_{LA} \rightarrow a_{TA} + a_{TA}$ channel in Fig. 6.5b. This distribution is shown as a function of the larger of the two TA phonon frequencies involved in decay of LA phonon through $\omega_{LA} = \omega_{TA}' + \omega_{TA}''$, denoting it by ω'' on x -axis in Fig. 6.5b. This split of overall phase space for the channel $a_{LA} \rightarrow a_{TA} + a_{TA}$ into contributing frequencies is shown at

the two wavevectors discussed above, namely, $q_x=0.60$ for unstrained and $q_x=0.45$ for strained cases (wavevectors at which $a_{LA} \rightarrow a + a$ channel is seen to peak in Fig. 6.4e), Fig. 6.5b shows that the peak contribution to scattering of LA phonon at $q_x=0.60$ ($\omega = 103 \text{ cm}^{-1}$) in unstrained InSb is from TA phonons with frequency $\omega'' \sim 60 \text{ cm}^{-1}$ (with corresponding $\omega' = 43 \text{ cm}^{-1}$); these frequencies correspond to the two peaks in phonon density of states (Fig. 6.1). In strained InSb, however, Fig. 6.5b shows that strong contribution to scattering of LA phonon at $q_x = 0.45$ ($\omega = 82.2 \text{ cm}^{-1}$) is from TA phonons of much lower frequencies, with peak contribution occurring from $\omega'' \sim 48 \text{ cm}^{-1}$ (with $\omega' = 34.2 \text{ cm}^{-1}$) (Fig. 6.5b) in strained InSb. This provides evidence of the dominant role of lower frequency TA phonons in increasing scattering rates of mid-Brillouin zone LA phonons in strained InSb.

However, while the peak phase space shifts to lower wavevector in strained InSb relative to unstrained InSb, the peak value of this phase space remains almost the same in magnitude (~ 0.11) for strained and unstrained cases (Fig. 6.5a), and cannot alone explain the ~ 2 -fold higher peak scattering rate in strained InSb (seen in Fig. 6.4b), relative to peak rate for unstrained InSb. This increase can be explained by an increase in magnitude of three-phonon coupling elements in strained InSb. Notice that the three-phonon coupling elements $|V_3(-\lambda, \lambda', \lambda'')|^2$ in equation 3.2 are inversely proportional to the product of the three frequencies involved in scattering⁴⁴, $|V_3(-\lambda, \lambda', \lambda'')|^2 \propto \frac{1}{\omega(\lambda)\omega'(\lambda')\omega''(\lambda'')}$. A shift in scattering to lower frequencies in strained InSb increases the magnitude of these coupling elements. The approximate ratio of $|V_3(-\lambda, \lambda', \lambda'')|^2$ corresponding to peak frequency contributions to scattering of wavevector $q_x = 0.60$ in unstrained and $q_x = 0.45$ strained InSb (described above and shown in Fig. 5b) can be computed as $\frac{|V_3(-\lambda, \lambda', \lambda'')|_{strain, q_x=0.45}^2}{|V_3(-\lambda, \lambda', \lambda'')|_{unstrain, q_x=0.60}^2} = \frac{(103)(43)(60)}{(82.2)(34.2)(48)} = 1.97$. Distribution of all $|V_3(-\lambda, \lambda', \lambda'')|^2$ involved in scattering of LA phonons at the two wavevectors is also shown in Fig 6.5c. Overall, the average value of $|V_3(-\lambda, \lambda', \lambda'')|^2$ involved in scattering of LA phonon at $q_x = 0.45$ in strained InSb is found to be almost two-fold higher relative to the case of $q_x=0.60$ in unstrained InSb. These higher magnitudes of three-phonon coupling elements (Fig. 6.5c) combined with increase in scattering phase space (Fig. 6.5a) lead to the observed large increase in scattering rates of LA phonons in the middle of the Brillouin zone in strained InSb.

6.2.3 INCREASE IN TA PHONON SCATTERING

For TA modes, strain is found to increase the magnitude of $a + a \rightarrow a$ and $a + o \rightarrow o$ scattering channels (Fig. 6.4f and g, respectively) leading to an increase in TA phonon scattering rate by a maximum of ~60% close to zone edge (point X) (Fig. 6.4b). Increase in $a + a \rightarrow a$ scattering for TA phonons can be understood by an increase in frequencies of LA phonons in strained InSb. Fig. 6.1 shows that, while, maximum LA phonon frequency in unstrained InSb is 150.4 cm^{-1} , the peak frequency in strained InSb is 162.8 cm^{-1} . This increase in LA frequencies introduces new $a + a \rightarrow a$ channels for TA phonons. This is seen through an example, by considering that in strained InSb, a TA phonon of frequency $\omega = 20 \text{ cm}^{-1}$ can scatter by absorbing an LA phonon of frequency $\omega' = 140 \text{ cm}^{-1}$, yielding an LA phonon of frequency $\omega'' = 160 \text{ cm}^{-1}$, thus satisfying energy conservation $\omega + \omega' = \omega''$ (provided the momentum conservation is satisfied) (Fig. 6.1). In unstrained case, however, LA phonon frequencies are lower, and an LA phonon of frequency $\omega'' = 160 \text{ cm}^{-1}$ does not exist, forbidding this channel. The presence of additional scattering channels in strained InSb leads to increase in $a + a \rightarrow a$ scattering for TA phonons. The effect is found to lead to larger increase in scattering at higher wavevectors (Figs. 6.4b and f); this can be understood by realizing that a TA phonon of frequency ω can only scatter into a final LA phonon of frequency ω'' higher than ω , restricting the frequency range $(\omega''_{LA,max} - \omega)$ for scattering as ω increases. Increase in LA frequencies in strained InSb by increasing this frequency range, thus resulting in a more dramatic increase in scattering of higher frequency TA phonons.

Increase in $a + o \rightarrow o$ channel for TA phonons can similarly be understood in terms of increase in optical frequency range in strained InSb. While in unstrained InSb, optical phonons range from $140.8 - 200.5 \text{ cm}^{-1}$, in strained InSb, the corresponding range is from $144.1 - 217.7 \text{ cm}^{-1}$. This increase in optical phonon frequency range introduces new channels for scattering of higher frequency TA phonons. This can be again be seen through an example, by considering that in strained InSb, a TA phonon of frequency 30 cm^{-1} can absorb an optical phonon of frequency 180 cm^{-1} to yield an optical phonon of frequency 210 cm^{-1} . However, in unstrained such a scattering channel is forbidden because of the lower optical phonon frequencies.

Above presented increase in scattering rates of TA and LA phonons diminishes their k contributions in strained InSb. While in unstrained InSb, TA and LA phonons contribute 10.52 and 8.30 W/mK to total k at 300 K , in strained InSb, their contribution decreases to 7.91 and 5.47 W/mK , respectively, along the in-plane direction, leading to the observed 29% decrease in k .

Strain induced increase in phonon scattering may provide avenues to enhance thermoelectric efficiency through above demonstrated decrease in k . Biaxial strain investigated in this work, can be achieved by growth of a material on a lattice mismatched substrate¹³¹, providing avenues for realization of outlined decrease in k in applications.

6.4 CONCLUSION

Using first principles approach we have provided a microscopic description of decrease in thermal conductivity (k) in strained Indium Antimonide (InSb). While k of unstrained InSb is computed to be 18.82 W/mK at 300 K, upon 5% biaxial compression, k decreases to 13.38 W/mK and 15.62 W/mK along in-plane (plane in which biaxial strain is applied) and out-of-plane directions. This reduction in k is due to increase in phonon scattering rates of both longitudinal (LA) and transverse (TA) acoustic phonons. Increase in scattering of LA phonons is found to be due to a shift in TA phonon frequencies to lower values in strained InSb, which both increases the phase space for scattering and the magnitude of three-phonon coupling elements involved in scattering of mid-Brillouin zone LA phonons, leading to a large 330% increase in scattering rate of zone-center LA phonons. Increase in TA scattering rates is found to be due to increase in LA and optical phonon frequencies in strained InSb, which increase the number of absorption scattering channels for TA phonons. These results have important implications for design of high efficiency InSb based thermoelectrics.

CHAPTER 7: FIRST PRINCIPLES INVESTIGATION OF ULTRA-HIGH THERMAL CONDUCTIVITY in HEXAGONAL GERMANIUM CARBIDE(2H-GeC)

Thermal conductivity in nanostructures differs from bulk values because of the comparable meanfreepaths (MFP) to the characteristic length of the nanostructures¹³². Thermal conductivity is reduced significantly when the dimensions are reduced to nanoscale due to boundary scattering of phonons^{133, 134}. In bulk materials with phonon mean free path of the acoustic phonons higher than the system size, boundary scattering will occur when the system is reduced. Typically, acoustic phonons conduct most of the heat due to high phonon group velocities and vibrational frequencies with optical phonons being the scattering channels for the acoustic phonons through Umklapp scattering. Various materials have been reported with optical phonons making a significant contribution to overall thermal conductivity¹³⁵⁻¹³⁸. Despite having an ultra-high thermal conductivity (k) of $1517 \text{ Wm}^{-1}\text{K}^{-1}$ in cubic germanium carbide(c-GeC)¹³⁹, k of its wurtzite structure is unknown. Electronic properties of bulk¹⁴⁰ and monolayer¹⁴¹ hexagonal germanium carbide have been reported; however, there is lack of knowledge of its thermal conductivity. In this work¹⁴², we are reporting an ultra-high thermal conductivity of $1350 \text{ Wm}^{-1}\text{K}^{-1}$ ($1050 \text{ Wm}^{-1}\text{K}^{-1}$) along the a-axis (c-axis) in hexagonal germanium carbide(2H-GeC) which is 130% higher than the hexagonal silicon carbide (2H-SiC)¹⁴³. We systematically investigate the contributions from transverse acoustic (TA), longitudinal acoustic (LA) and optical phonons modes. Our first principles calculations reveal that, optical phonons with high phonon group velocity contribute ~46% to overall thermal conductivity at room temperature (300 K). We also report the length dependent thermal conductivity between 10 nm - 1000 nm for application in nanoscale. At nanometer length scale of $L = 100 \text{ nm}$, a high thermal conductivity of ~65 $\text{Wm}^{-1}\text{K}^{-1}$ is reported. High thermal conductivity of 2H-GeC in both bulk and nanoscale indicates that, 2H-GeC will be a promising material for thermal management applications.

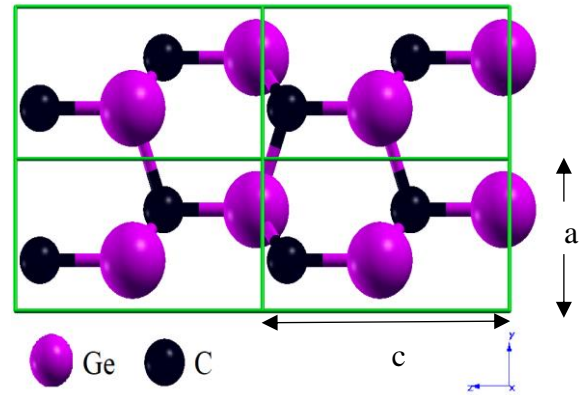


Figure 7.1: Atomic structure of 2H-GeC

7.1 COMPUTATIONAL METHODS: The geometry of the 2H-GeC with 4 atoms unit cell is optimized until the forces on all atoms are less than 10^{-5} eV \AA^{-1} and the energy difference is converged to 10^{-12} Ry. A plane-wave cutoff energy of 80 Ry was used. Monkhorst-Pack¹¹⁵ k -point mesh of $12 \times 12 \times 8$ is used during the variable cell optimization. Optimized 2H-GeC structure with lattice constants of $a=3.188$ \AA and $c/a=1.646$, is shown in Fig. 7.1 (in good agreement with the previous study¹⁴⁰). Elastic constants were computed using QUANTUM ESPRESSO thermo_pw package and Voigt-Reuss-Hill approximation¹⁴⁴ is used to calculate the bulk modulus, shear modulus(G) and Young's Modulus(E). Lattice thermal conductivity is calculated by deriving the most important ingredients, namely, the harmonic and anharmonic interatomic force interactions from density-functional theory and using them with an exact solution of the phonon Boltzmann transport equation (PBTE)^{85, 89, 91}. Phonon linewidth and lattice thermal conductivity were calculated iteratively using QUANTUM ESPRESSO thermal2 code with $30 \times 30 \times 24$ q - mesh and 0.05 cm^{-1} smearing until the Δk values are converged to $1.0e^{-5}$. Casimir scattering¹⁴⁵ is imposed for length dependent thermal conductivity calculations. Thermal conductivity for

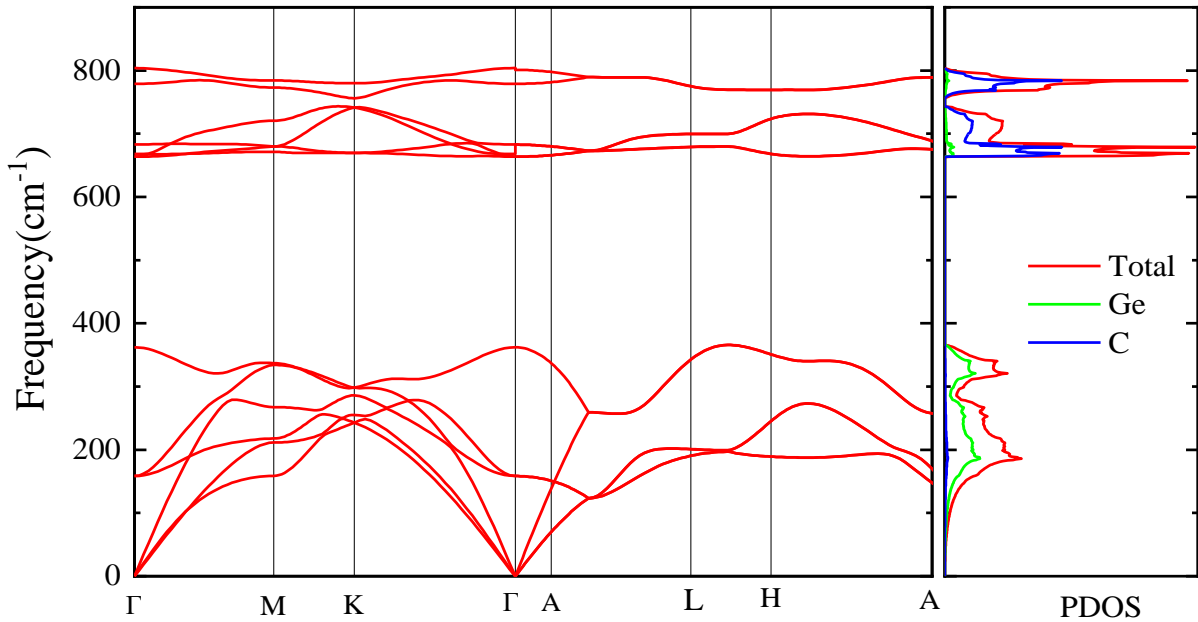


Figure 7.2: Phonon dispersion and phonon density of state for the 2H-GeC with lattice constants $a=3.188$ \AA and $c/a=1.646$

naturally occurring 2H-GeC was computed by introducing phonon scattering arising out of mass-

disorder due to random distribution of isotopes¹⁴⁶ of Carbon and Germanium throughout the crystal.

7. 2 RESULTS

7.2.1 Phonon dispersion and elastic constants

Table 7.1: Elastic constants of 2H-GeC

Material	C11	C33	C44	C66	C12	C13	Bulk Modulus(B)	Young modulus(E)	Shear Modulus(G)
2H-GeC	440.6	488.13	136.6	181	78.5	36.5	185.8	389	169
2H-SiC	522.5	557.7	156.1	214.9	92.64	43.6	218	453.2	196.4

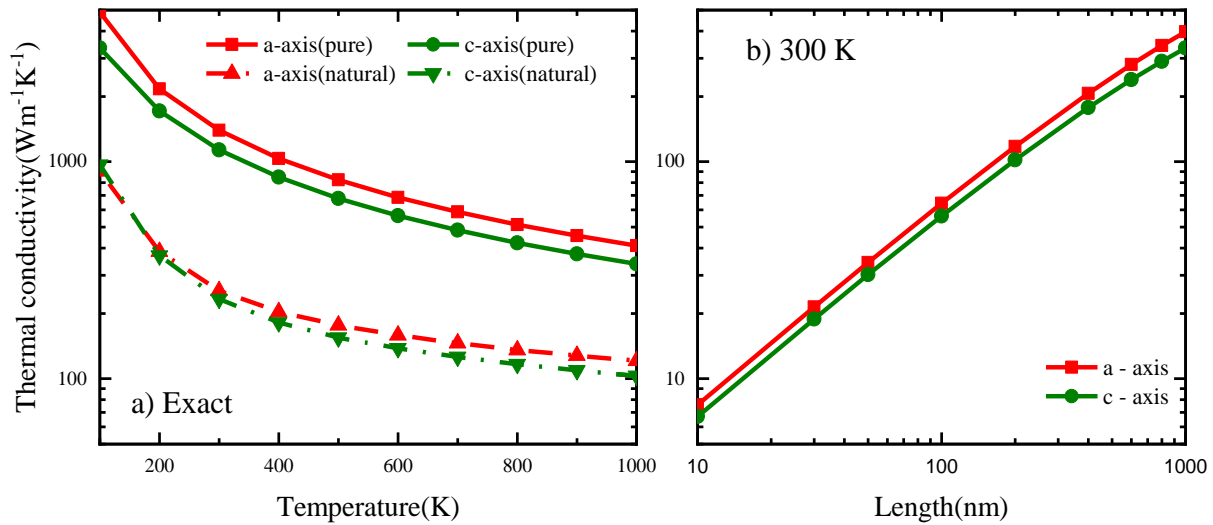


Figure 7.3: Temperature dependent lattice thermal conductivity of the isotopically pure and natural 2H-GeC along a and c axis. 3b) Length dependent lattice thermal conductivity of 2H-GeC along a and c axis.

Phonon dispersion and phonon density of states for the 2H-GeC with equilibrium lattice constants $a=3.188 \text{ \AA}$ and $c/a=1.646$ are shown in Fig 7.2. Positive phonons frequencies of all the phonon branches indicate dynamical stability of 2H-GeC. To validate the mechanical stability of the system, we calculated elastic constants to check the Born stability criteria¹⁴⁷. Elastic constants of 2H-GeC are listed in Table 7.1 and the values are in good agreements with the previously reported value¹⁴⁰. The calculated elastic constants satisfied the Born stability criteria of $C_{66}=(C_{11}-C_{12})/2$, $C_{11} > C_{12}$, $C_{33}(C_{11}+C_{12}) > 2(C_{13})$, $C_{44} > 0$, $C_{66} > 0$, and hence the system is mechanically stable. Bulk modulus(B), Young modulus(E) and Shear modulus based on Voigt-Reuss-Hill

approximation are also listed in Table 7.1. The computed values are slightly lower than the hexagonal diamond. These constants indicate the mechanical and dynamical stability of 2H-GeC.

7.2.2 LATTICE THERMAL CONDUCTIVITY

Temperature dependence thermal conductivity (k) of pure (solid lines) and naturally (dotted lines)

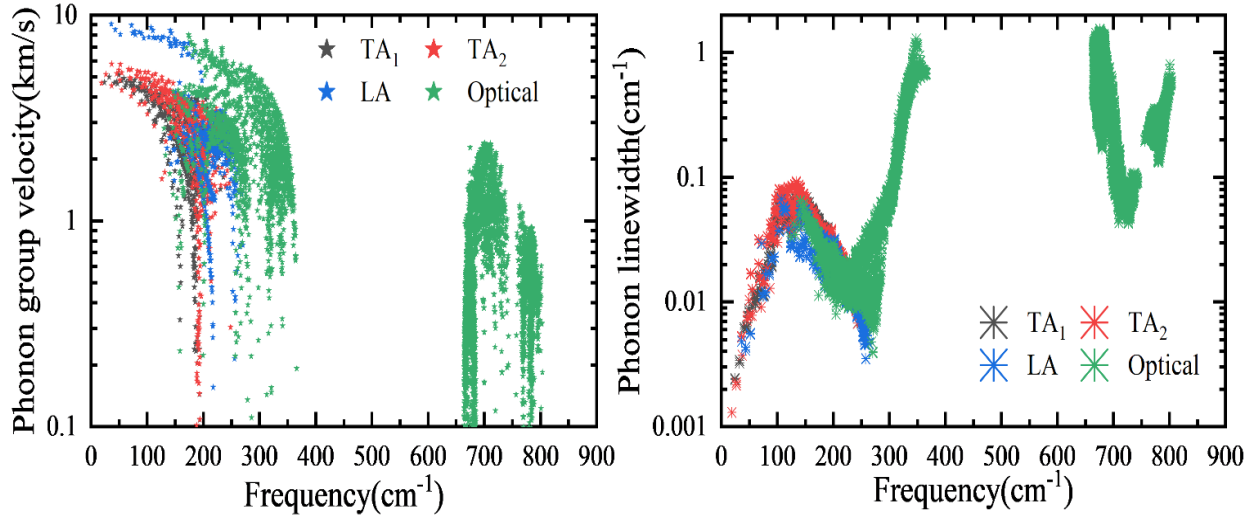


Figure 7.4 a) Phonon group velocity and b) phonon linewidth (inverse of lifetime) for a hexagonal germanium carbide(2H-GeC)

occurring 2H-GeC., obtained by solving the phonon Boltzmann transport equation exactly, is shown along a- and c-axis in Fig 7.3a. At 300 K, thermal conductivity of pure and naturally occurring 2H-GeC is $1396 \text{ Wm}^{-1}\text{K}^{-1}$ ($1135 \text{ Wm}^{-1}\text{K}^{-1}$) and $255 \text{ Wm}^{-1}\text{K}^{-1}$ ($233 \text{ Wm}^{-1}\text{K}^{-1}$) respectively along the a-axis (c-axis). k of naturally occurring 2H-GeC is just 18.2% (20.52%) of the pure 2H-GeC along a-axis which is in good agreement with the cubic germanium carbide (c-GeC)¹³⁹. This is due to the large number of natural

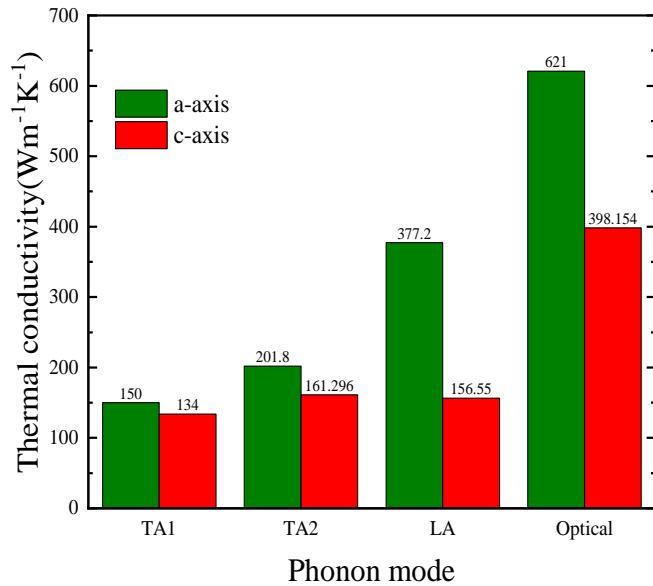


Figure 7.5: Thermal conductivity contribution from TA₁, TA₂, LA and optical phonon modes at 300 K.

isotopes¹⁴⁶ of germanium (20.57% ^{69.924}Ge, 27.45% ^{71.922}Ge, 7.75% ^{72.923}Ge, 36.5% ^{73.921}Ge and 7.73% ^{75.921}Ge) and carbon (98.93% ¹²C and 1.07% ^{13.003}C).

This ultra-high thermal conductivity of 2H-GeC is mainly attributed to high phonon frequencies (ω_λ) and phonon group velocities ($= \partial\omega_\lambda/\partial q$) of both acoustic and optical phonons (Shown in Fig.7.4a) as well as the large phonon bandgap ($\sim 335 \text{ cm}^{-1}$) between the acoustic and high frequency optical phonons. These high frequencies are due to the strong bonds between the germanium and carbon atoms and the light atomic mass of the constituent atoms C and Ge. These strong bonds are verified by the elastic constants presented in Table 7.1 with 2H-SiC^{148, 149} which are in good agreement with the previous study. Elastic constants of 2H-GeC are slightly lower than the 2H-SiC. This is due to

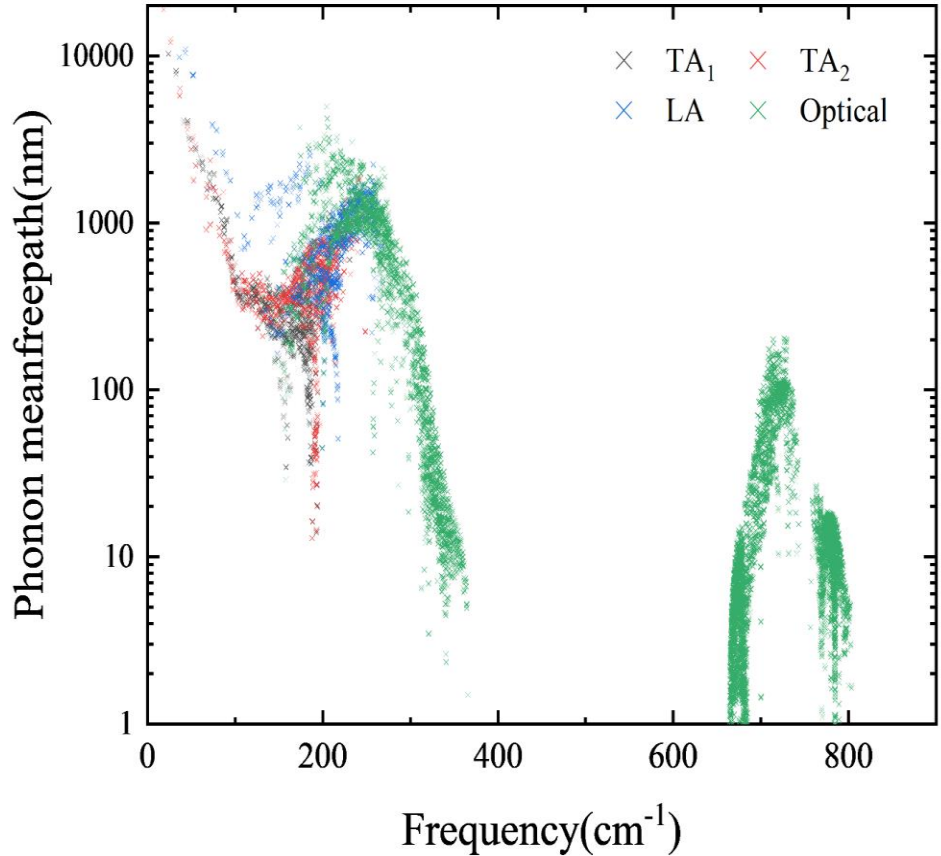


Figure 7.6: Phonon meanfreepaths (nm) of TA₁, TA₂, LA and acoustic phonon modes for 2H-GeC at room temperature

the strong covalent bond between germanium and carbon atoms. Interestingly, we can observe that, optical phonons have significant phonon group velocities (Fig 7.4a) and phonon lifetimes (Fig 7.4b). To elucidate contribution of optical phonons to overall thermal conductivity, we computed the mode dependent thermal conductivity of transverse acoustic (TA₁ and TA₂), longitudinal acoustic (LA) and optical phonon modes (shown in Fig 7.5). We can observe that, at

300 K, optical phonons contribute $621 \text{ Wm}^{-1}\text{K}^{-1}$ ($398 \text{ Wm}^{-1}\text{K}^{-1}$) to overall thermal conductivity along a-axis(c-axis). This is approximately 46% (45%) contribution to overall thermal conductivity and is higher than both transverse and longitudinal acoustic phonon modes. This is due to the high phonon group velocities and phonon lifetimes of optical phonons.

We also report the length dependent lattice thermal conductivity between 10 nm and 1000 nm as shown in Fig 7.3b for the thermal management in nanostructures. At nanoscale length of $L=100 \text{ nm}$, room temperature thermal conductivity of $70 \text{ Wm}^{-1}\text{K}^{-1}$ is 100% higher than that the cubic germanium carbide. This is due to the large contribution from optical phonons with phonon meanfreepath in the range of 100 nm as shown in Fig 7.6.

7.3 CONCLUSION

In summary, using first principles calculations, we report the lattice thermal conductivity (k) of isotopically pure and naturally occurring hexagonal germanium carbide(2H-GeC) by solving the Boltzmann transport equation exactly. At room temperature, we report an ultra-high thermal conductivity of $1350 \text{ Wm}^{-1}\text{K}^{-1}$ ($1050 \text{ Wm}^{-1}\text{K}^{-1}$) along the a-axis (c-axis) for the pure hexagonal germanium carbide(2H-GeC) which is 130% higher than the value for hexagonal silicon carbide(2H-SiC). We observed a large reduction (approximately 80%) in k due to large number of isotopes of germanium and moderate isotopic variation in carbon. We also report the length dependence lattice thermal conductivity for the applications in micro/nanoelectronics. At nanometer length scales of $L=100 \text{ nm}$, a high thermal conductivity of $70 \text{ Wm}^{-1}\text{K}^{-1}$ is 100% higher than cubic germanium carbide. These results may lead to potential applications of 2H-GeC in nanoscale thermal management.

CHAPTER 8: ULTRAHIGH THERMAL CONDUCTIVITY IN HEXAGONAL BC₆N- AN EFFICIENT MATERIAL FOR NANOSCALE THERMAL MANAGEMENT – A FIRST PRINCIPLES STUDY

Cubic¹⁵⁰⁻¹⁵² and hexagonal diamond¹⁵³ (also known as lonsdaleite) have been reported as the most thermally conductive materials on earth due to strong covalent bonds and light atomic mass of carbon atoms. Likewise, boron^{70, 136, 137, 154-159} based compounds were reported with high thermal conductivity due to high phonon group velocity arising from the light atomic mass. Recently, Sadeghi *et al.*, reported a high thermal conductivity of 2073 Wm⁻¹K⁻¹ for the hexagonal BC₂N(*h*-BC₂N)¹³⁷. Likewise, Shafique *et al.*, reported a high thermal conductivity of 1275 Wm⁻¹K⁻¹ for the monolayer graphene like BC₂N¹⁵⁶. Mortazavi *et al.*, reported an ultra-high thermal conductivity 1710 Wm⁻¹K⁻¹ for the monolayer BC₆N¹⁶⁰ but its counterpart of bulk thermal conductivity is yet to be reported. In this work¹⁶¹, we analyzed the thermal conductivity of bulk and nanostructured hexagonal BC₆N(*h*-BC₆N) through first principles calculations. Our first principles calculations reveal an ultra-high bulk thermal conductivity (*k*) of 2090 Wm⁻¹K⁻¹(1395 Wm⁻¹K⁻¹) for the pure (natural) hexagonal BC₆N which is among the highest thermal conductivity values ever reported (lower only to diamond and boron arsenide¹⁵⁷). Likewise, at nanometer length scales such as 100 nm, room temperature thermal conductivity is computed to be 175 Wm⁻¹K⁻¹, indicating *h*-BC₆N will be a candidate material for thermal management in nanoelectronics. We systematically investigated the elastic constants, mode-contribution thermal conductivity of transverse acoustic (TA), longitudinal acoustic (LA) and optical phonon modes, phonon group velocity, phonon scattering rates and phonon mean free paths. We noticed that, optical phonons with considerable phonon group velocities and phonon lifetimes, contribute significantly to overall thermal conductivity in *h*-BC₆N.

8.1 COMPUTATIONAL METHODS

The geometry of the hexagonal BC₆N(*h*-BC₆N) with 8 atoms unit cell is optimized until the

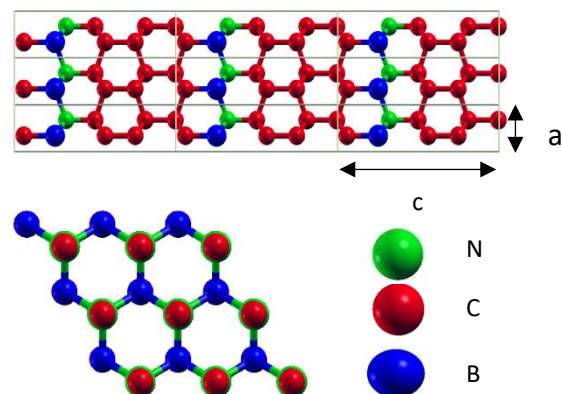


Figure 8.1: *h*-BC₆N crystal structure with lattice parameters *a*= 2.4802 Å and *c/a*=3.3438. Blue, red and green represents the boron, carbon and nitrogen atoms respectively.

forces on all atoms are less than 10^{-5} eV \AA^{-1} and the energy difference is converged to 10^{-15} Ry. A plane-wave cutoff energy of 80 Ry was used. Electronic calculations were performed using $12 \times 12 \times 4$ Monkhorst-Pack¹¹⁵ k -point mesh. Optimized h -BC₆N structure with lattice constants of $a=2.4802$ \AA and $c/a=3.3438$ is shown in Fig. 8.1. Elastic constants were computed using QUANTUM ESPRESSO thermo_pw package and Voigt-Reuss-Hill approximation¹⁴⁴ is used to calculate the bulk modulus(B), Young's Modulus(E) and shear modulus(G). Dynamical matrix and harmonic force constants were computed using $12 \times 12 \times 4$ q-grid. $6 \times 6 \times 2$ q-points were used to compute the anharmonic force constants using QUANTUM ESPRESSO D3Q⁸⁹⁻⁹¹ package. Acoustic sum rules were imposed on both harmonic and anharmonic interatomic force constants. Lattice thermal conductivity(k) is calculated by solving phonon Boltzmann transport equation (PBTE)^{85, 89, 91}.

Phonon linewidth and lattice thermal conductivity were calculated iteratively using QUANTUM ESPRESSO thermal2 code with $30 \times 30 \times 10$ q -mesh and 0.05 cm^{-1} smearing until the Δk values are converged to $1.0e^{-5}$ $\text{Wm}^{-1}\text{K}^{-1}$. Iterative results were converged after 6 iterations.

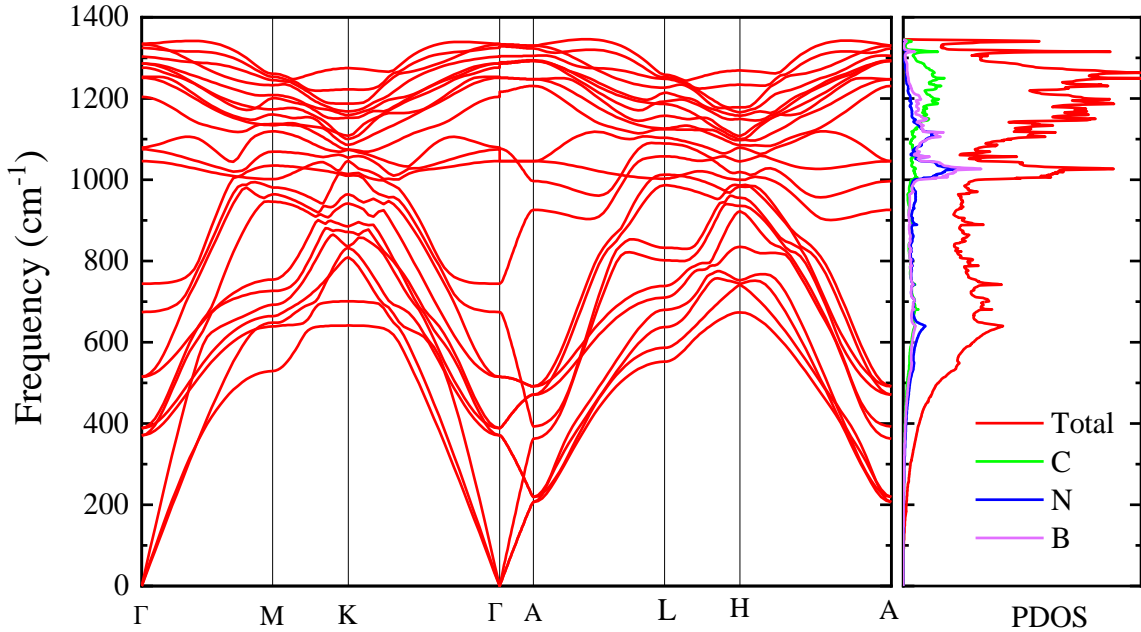


Figure 8.2: Phonon dispersion and phonon density of states for the hexagonal BC₆N with lattice constants $a= 2.4802$ \AA and $c/a=3.3438$. Green, blue and purple color represents the contributions from carbon (C), nitrogen (N) and boron (B) respectively.

Casimir scattering¹⁴⁵ is imposed for size dependence thermal conductivity calculations for the nanostructured h -BC₆N.

Table 8.1: Elastic constants (in GPa) of h -BC₆N, h -Diamond and h -BC₂N.

Material	C11	C33	C44	C66	C12	C13	Bulk Modulus (B)	Young modulus (E)	Shear Modulus (G)
h -BC ₆ N	1182.98	1298.11	438.90	537.20	108.58	20.33	440.00	1107.40	512.30
h -Diamond	1251.52	1367.74	483.00	579.40	92.61	20.00	450.74	1182.45	556.31
h -BC ₂ N	1091.10	1146.23	399.50	498.70	93.60	2.97	391.90	1007.40	470.05

8.2 RESULTS

8.2.1 Phonon dispersion and elastic constants

Phonon dispersion and phonon density of states for the hexagonal BC₆N with its equilibrium lattice constants $a = 2.4802 \text{ \AA}$ and $c/a = 3.3438$ is shown in Fig 8.2. Positive phonons frequencies of all the phonon branches indicate the dynamical stability of h -BC₆N. Elastic

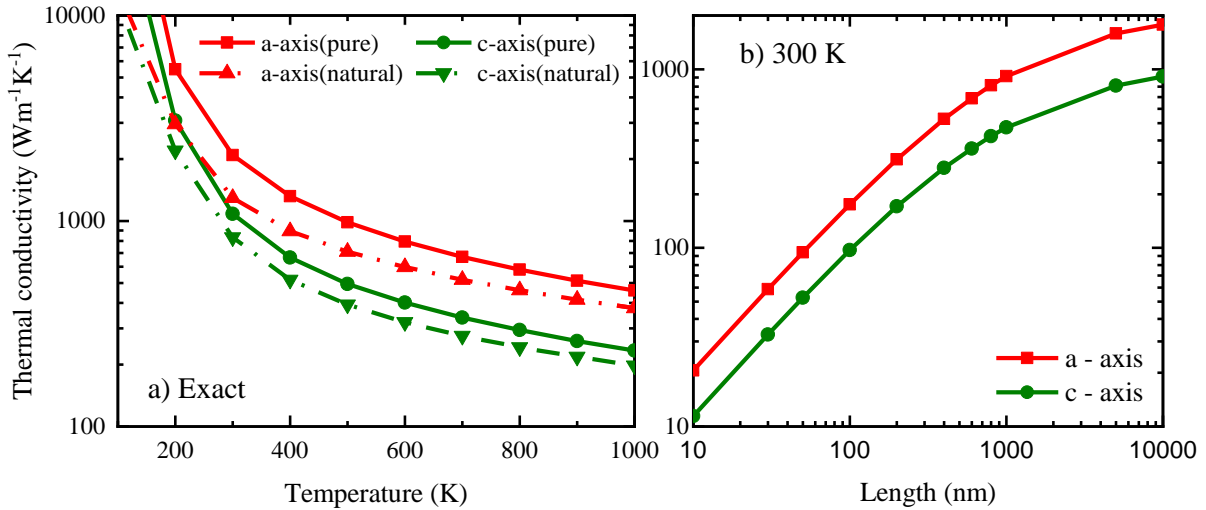


Figure 8.3 a): Temperature dependent lattice thermal conductivity along a and c axis for pure and naturally occurring h -BC₆N. b) Room temperature size dependence thermal conductivity of pure h -BC₆N.

constants of h -BC₆N are listed in Table 8.1 and compared against h -diamond and h -BC₂N. The calculated elastic constants satisfied the Born stability criteria and hence the system is mechanically stable. Bulk modulus(B), Young modulus(E) and Shear modulus(G) based on Voigt-

Reuss-Hill approximation are also listed in Table 8.1. The computed values are slightly lower than the hexagonal diamond. These elastic constants and positive frequencies in phonon dispersion indicate the mechanical and dynamical stability of h -BC₆N.

8.2.2 LATTICE THERMAL CONDUCTIVITY

Temperature dependent lattice thermal conductivity (k) of the pure (solid lines) and naturally (dotted lines) occurring h -BC₆N, obtained by solving the phonon Boltzmann transport

equation exactly, is shown along a-axis and c-axis in Fig 8.3a. At 300 K, thermal conductivity of

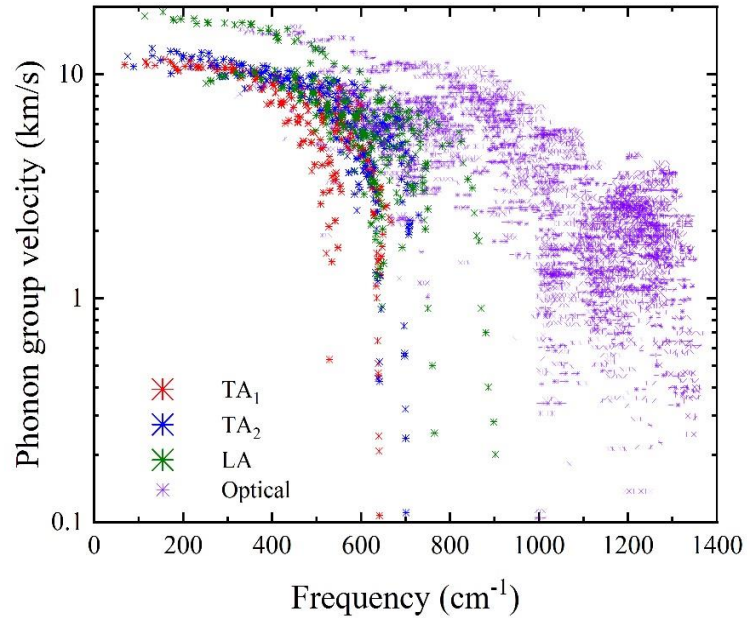


Figure 8.4: Phonon group velocity of TA₁, TA₂, LA and Optical phonon modes of h -BC₆N.

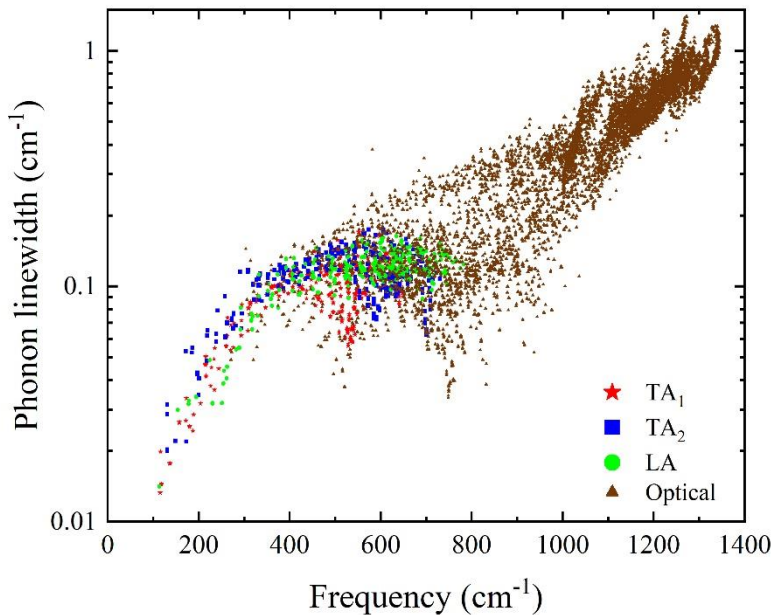


Figure 8.5: Phonon linewidths of TA₁, TA₂, LA and optical phonons for h -BC₆N. Red, Blue, Green and brown color represents the TA₁, TA₂, LA and optical phonons respectively.

pure and naturally occurring h -BC₆N is 2090 Wm⁻¹K⁻¹ (1082 Wm⁻¹K⁻¹) and 1395 Wm⁻¹K⁻¹ (832 Wm⁻¹K⁻¹) respectively along the a-axis (c-axis). k of naturally occurring h -BC₆N is 33.25% lower than the pure h -BC₆N. Thermal conductivity for naturally occurring h -BC₆N was computed by introducing phonon scattering arising out of mass-disorder due to random distribution of isotopes of Boron, Carbon and Nitrogen throughout the crystal. The

small mass variation in isotopes of B (atomic mass of 10.012 a.u with 19.9% concentration and atomic mass of 11.009 a.u with 80.1% concentration), C (atomic mass of 12 a.u with 98.93% concentration and 13.0033 a.u with 1.07% concentration) and N (atomic mass of 14.003 a.u with 99.636% concentration and 15.0 a.u with 1.07% concentration) atoms¹⁶², induces moderate additional phonon scattering, causing only 33.25% decrease in thermal conductivity of naturally occurring *h*-BC₆N relative to the pure case. At 300K, lattice thermal conductivity of *h*-BC₆N within the SMA is 1601 Wm⁻¹K⁻¹ (999 Wm⁻¹K⁻¹) along the a-axis (c-axis); this value is 23.3% (7.67%) lower than the iterative solution.

This ultra-high thermal conductivity of *h*-BC₆N is mainly attributed to high phonon frequencies (ω_λ) and phonon group velocities ($= \partial\omega_\lambda/\partial q$) of both acoustic and optical phonons. These high frequencies are due to the strong C-C, B-C and B-N bonds and the light atomic mass of the constituent atoms B, C and N. These strong bonds are verified by the elastic constants presented in Table 8.1 with diamond and *h*-BC₂N. Bulk modulus and Young modulus for *h*-BC₆N is close to that of diamond. This is due to the strong covalent bond network through *sp*³ hybridization of the atoms.

To elucidate further, we analyzed the mode contribution thermal conductivity, phonon group velocities and phonon scattering rates of transverse acoustic (TA), longitudinal acoustic (LA) and optical phonons. At 300 K, we observed that, TA₁, TA₂, LA and optical phonons contribute 21.9% (16.62%), 18.11% (15.77%), 17.37% (18.87%) and 42.62% (48.74%) to overall thermal conductivity, respectively, along a-axis (c-axis). Typically, acoustic phonons are considered as major heat carrier phonons and optical phonons serve as a scattering channels for the acoustic phonons¹⁶³. It is interesting to note that in BC₆N, optical phonons also contribute significantly to overall thermal conductivity. This is mainly due to the fact that optical phonons

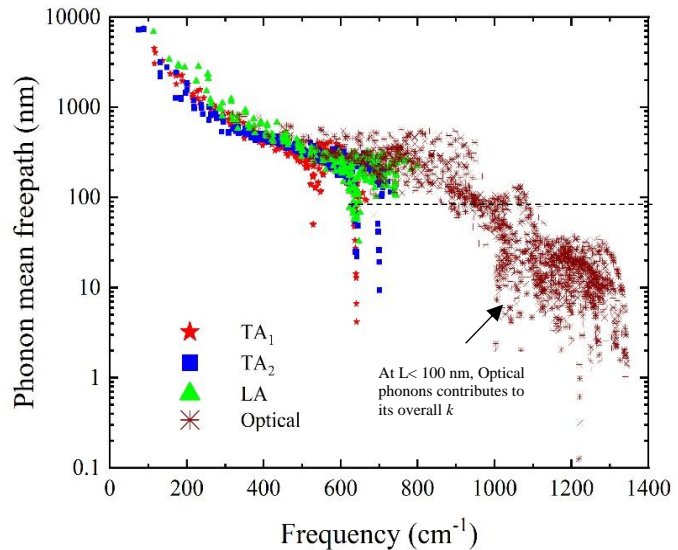


Figure 8.6: Phonon mean free path of TA₁, TA₂, LA and Optical phonons for *h*-BC₆N.

have considerable high phonon group velocities (Fig 8.4) and phonon lifetimes (inverse of the phonon linewidths as shown in Fig 8.5).

To explore the thermal transport in nanostructures, we have computed the size dependent thermal conductivity of *h*-BC₆N by introducing phonon boundary/Casimir¹⁴⁵ scattering. We have computed the length dependence of only pure *h*-BC₆N. Length dependent thermal conductivity(*k*) of *h*-BC₆N between 10 nm and 10 μm is shown in Fig 8.3b. For an example, at nanometer length scales of *L* = 100 nm, room temperature *k* of *h*-BC₆N is 175 Wm⁻¹K⁻¹ along the a-axis which is significantly higher than the thermal conductivity of bulk silicon¹⁶⁴. To understand this further, we computed the phonon mean free paths of TA₁, TA₂, LA and optical phonon modes as shown in Fig 8.6. We can observe that acoustic phonons have mean free path higher than 100 nm and will be scattered significantly for nanostructures smaller than 100 nm, due to boundary scattering. Optical phonon meanfreepaths, however, are in the range of nanometers, contributing to the high nanoscale thermal conductivity in *h*-BC₆N.

8.3 CONCLUSION

By solving Boltzmann transport equation with first principles calculations, we report an ultra-high lattice thermal conductivity of 2090 Wm⁻¹K⁻¹(1082 Wm⁻¹K⁻¹) along a-axis(c-axis) for pure hexagonal BC₆N(*h*-BC₆N) which is the 3rd highest reported thermal conductivity after diamond and cubic boron arsenide. This ultra-high thermal conductivity is mainly attributed to high phonon frequencies and phonon group velocities arising from the strong C-C, B-C and B-N bonds and the light atomic mass of the constituent atoms B, C and N. We also observed a significant phonon scattering due to isotopic disorder. Elastic constants show that *h*-BC₆N is ultrahard with elastic constants almost equal to diamond. We also computed the size dependent thermal conductivity of *h*-BC₆N between 10 nm and 10000 nm. At nanometer length scales of *L*=100 nm, a high room temperature thermal conductivity of 175 Wm⁻¹K⁻¹ was reported. This points to the promising nature of *h*-BC₆N as candidate for nanoscale thermal management applications.

CHAPTER 9- ULTRAHARD BC₅ – AN EFFICIENT NANOSCALE HEAT CONDUCTOR THROUGH DOMINANT CONTRIBUTION OF OPTICAL PHONONS

Boron and carbon based compound-semiconductors are promising materials for thermal management due to their high thermal conductivity emerging from light mass of atoms involved and strong bonds of C-C and B-C^{136, 165-169}. An ultra-high thermal conductivity of 2305 Wm⁻¹K⁻¹ for the super-hard bulk hexagonal BC₂N was reported by Safoura *et al.*¹³⁷. Similarly, high anisotropic thermal conductivities of 1275.79 Wm⁻¹K⁻¹ and 893.90 Wm⁻¹K⁻¹ were reported for monolayer BC₂N along zig-zag and arm-chair directions¹⁵⁶. BC₅ is a diamond-like ultra-hard semiconductor with exceptional hardness of 83 GPa and experimental bulk modulus of 335 GPa^{170, 171}. In this work¹⁷², we use first principles calculations to analyze the thermal conductivity of BC₅. At 300 K, we report a high thermal conductivity (k) of 169 Wm⁻¹K⁻¹ for bulk BC₅ (infinite dimensions) along a -axis. A high nanoscale thermal conductivity of ~ 51 Wm⁻¹K⁻¹ is reported for length scale of 50 nm (at 300 K), indicating BC₅ will be a promising material for thermal management in nanoelectronics. To understand the origin of this high nanoscale thermal conductivity we systematically analyzed elastic constants, phonon group velocities and phonon scattering rates of different phonon modes. The high nanoscale thermal conductivity is found to be due to a dominant contribution of optical phonons to overall thermal conductivity in BC₅; at 500 K and 1000 K, optical phonons (with meanfreepaths in the nanometer regime) contribute almost $\sim 54\%$ and 57.3% , respectively to the overall thermal conductivity along the a -axis. First-principles computations are used to shed light on the dominant role of optical phonons in BC₅ thermal conductivity.

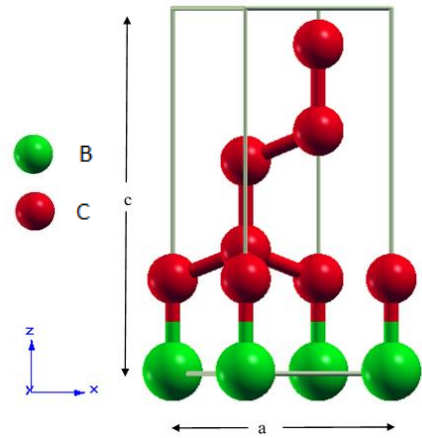


Figure 9.1: Atomic arrangements of BC₅ with space group P3m1. Red and green sphere represents the carbon and boron respectively.

9.1 COMPUTATIONALS METHODS

The geometry of the tetragonal (space group P3m1) BC_5 with 6 atoms unit cell is optimized until the forces on all atoms are less than 10^{-5} eV \AA^{-1} and the energy difference is converged to 10^{-12} Ry. A plane-wave cutoff energy of 100 Ry was used. Electronic calculations were performed using $12 \times 12 \times 6$ Monkhorst-Pack¹¹⁵ k -point mesh. Optimized BC_5 structure is shown in Fig. 9.1; obtained lattice constants of $a=2.516$ \AA and $c/a=2.506$ are in good agreement with the previous first principles calculations¹⁷³. Elastic constants were computed using QUANTUM ESPRESSO thermo_pw package and Voigt-Reuss-Hill approximation¹⁴⁴ is used to calculate the bulk modulus, shear modulus(G) and Young's Modulus(E). Lattice thermal conductivity is calculated by deriving the most important ingredients, namely, the harmonic and anharmonic interatomic force interactions from density-functional theory and using them with an exact solution of the phonon Boltzmann transport equation (PBTE)^{85, 89, 91}. Dynamical matrix and harmonic force constants were calculated using $8 \times 8 \times 4$ q-grid. $4 \times 4 \times 2$ q-points were used to compute the anharmonic force constants using QUANTUM ESPRESSO D3Q⁸⁹⁻⁹¹ package. Acoustic sum rules were imposed on both harmonic and anharmonic interatomic force constants. Phonon linewidth and lattice thermal conductivity were calculated iteratively using QUANTUM ESPRESSO thermal2 code with $30 \times 30 \times 15$ q-mesh and 0.05 cm^{-1} smearing until the Δk values are converged to $1.0e^{-5}$. Casimir scattering¹⁴⁵ is imposed for length dependence thermal conductivity calculations.

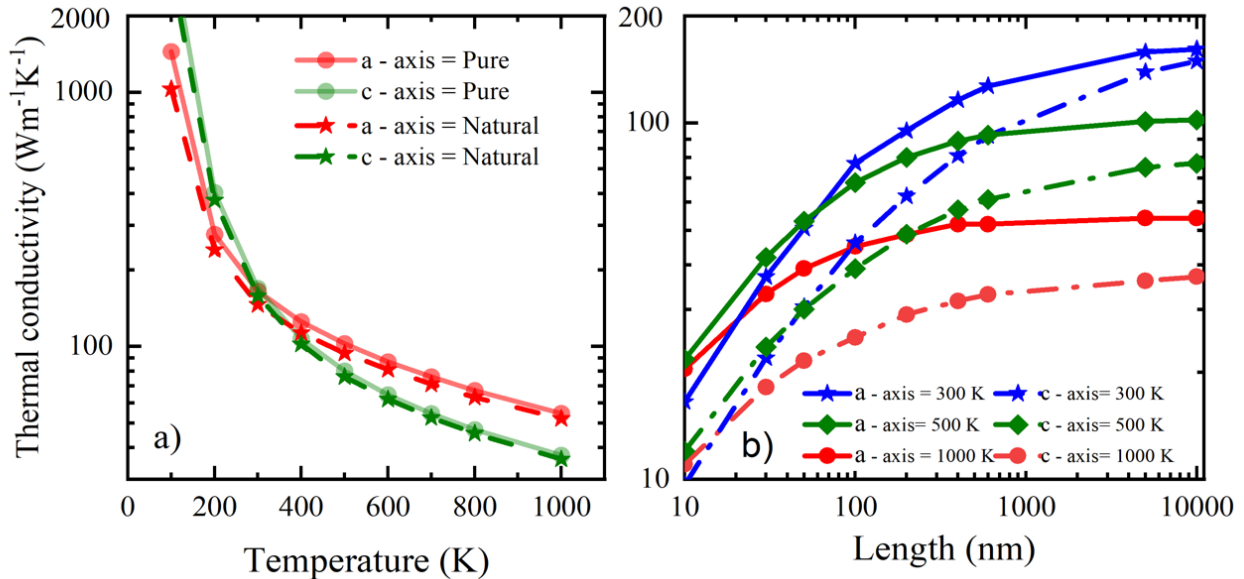


Figure 9.2: a) Thermal conductivity of BC_5 along a-axis and c-axis at different temperatures
b) Length dependence of thermal conductivity (300 K) of BC_5 between 10 nm and 10000 nm.

9.2 RESULTS

9.2.1 Lattice thermal conductivity

Lattice thermal conductivity of isotopically pure and isotopically disordered (naturally occurring) BC₅ along a-axis and c-axis is shown in Fig 9.2a as a function of temperature. At room temperature (300 K), computed thermal conductivities of bulk BC₅ along a-axis and c-axis are 165 W/mK and 169 Wm⁻¹K⁻¹, respectively, for pure BC₅. Our reported *k* values are higher than the *k* values of silicon (153 Wm⁻¹K⁻¹)¹⁷⁴ at room temperature suggesting that BC₅ will be a promising material for thermal management applications.

Table 9.1: Elastic constants of BC₅, Silicon and Diamond in GPa

Material	C11	C33	C44	C66	C12	C13	Bulk Modulus	Young modulus	Shear Modulus
BC ₅	911	1061.8	394.5	361.1	189	97	405	894	396
Silicon	159.5	159.5	78.1	78.1	61.3	61.3	94.1	158.1	64.8
Diamond	1099.5	1099.5	601.4	601.4	127.1	127.1	451.3	1176.8	552.3

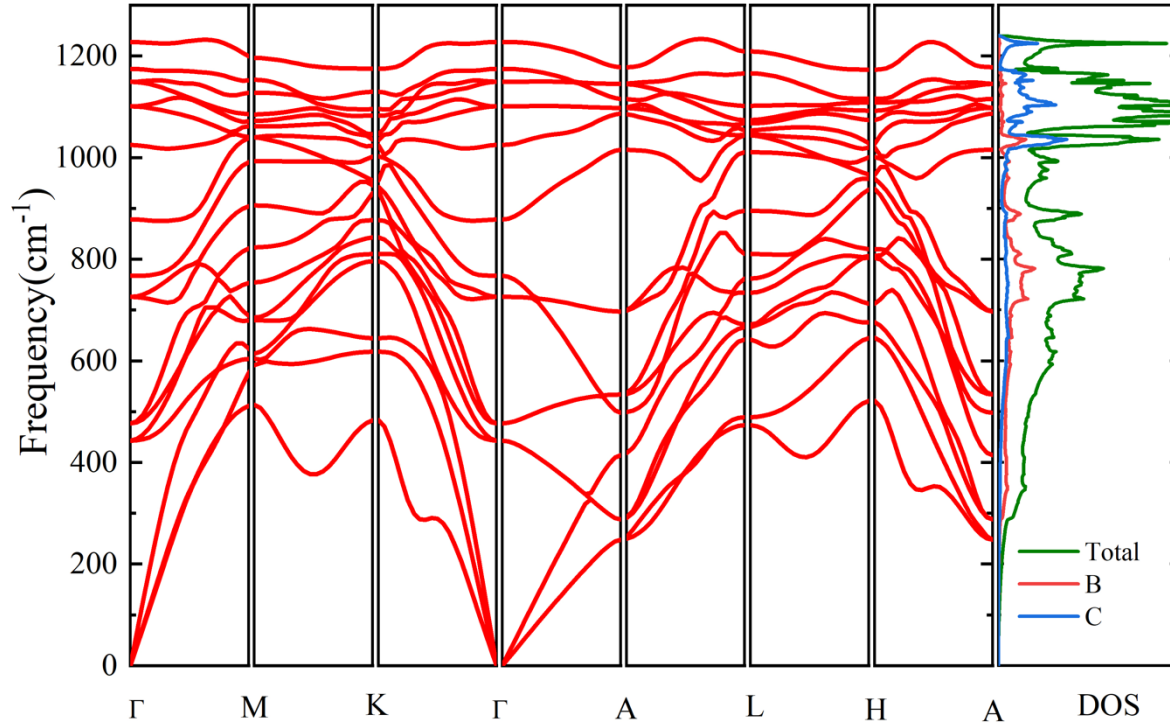


Figure 9.3: Phonon dispersion along the high symmetry points of tetragonal BC₅ and phonon density of states

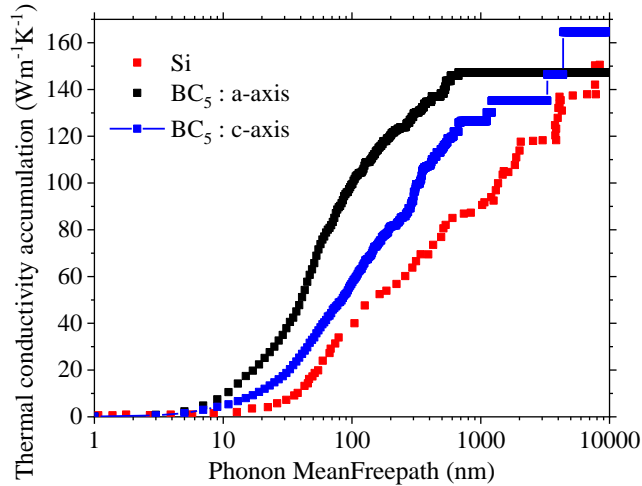


Figure 9.4: Phonon meanfreepath dependence thermal conductivity of BC5 and Silicon at 300 K.

are higher than Silicon and almost equal to the values for Diamond. This is due to the strong covalent bond network through sp^3 hybridization¹⁷⁶.

We also estimated k of naturally occurring BC₅ to be 146 Wm⁻¹K⁻¹ and 158 Wm⁻¹K⁻¹, along a-axis and c-axis, respectively at 300 K. k of naturally occurring BC₅ is only lower by 11.5% and 6.5% relative to pure BC₅ along a-axis and c-axis respectively. Thermal conductivity for naturally occurring BC₅ was computed by introducing additional phonon scattering arising out of mass-

This high thermal conductivity of BC₅ is a direct consequence of high phonon frequencies and phonon group velocities in BC₅ as seen in Fig. 9.3 resulting from the strong C-C and B-C bonds, and the light mass of B and C atoms. While in silicon, the maximum LA phonon frequency reaches 400 cm⁻¹¹⁷⁵, Fig. 9.3 shows that in BC₅, LA phonons have higher frequencies, reaching values greater than 600 cm⁻¹. The strong bonding in BC₅ is seen by noticing that the bulk modulus and Young Modulus of BC₅

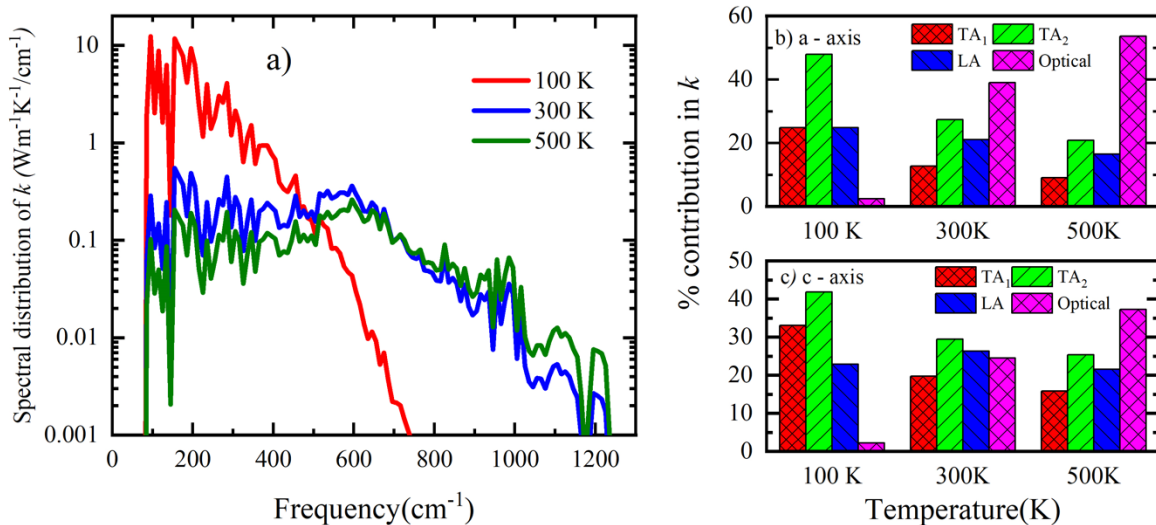


Figure 9.5a) Spectral distribution of k with frequency at 100 K, 300 K and 500 K. b and c) Percentage contribution by transverse acoustic (TA₁ and TA₂), longitudinal acoustic (LA) and optical phonon modes.

disorder due to random distribution of isotopes of Boron and Carbon throughout the crystal. The small mass variation in isotopes of both B (atomic mass of 10.013 a.u with 19.9% concentration and atomic mass of 11.009 a.u with 80.1% concentration) and C (atomic mass of 12 a.u with 98.93% concentration and 13.003 a.u with 1.07% concentration) atoms¹⁶², induces only a small additional phonon scattering, causing only a minor decrease in thermal conductivity of naturally occurring BC₅ relative to the pure case.

Length dependent k of pure BC₅ was also investigated by introducing Casimir scattering (boundary scattering). High thermal conductivity of $\sim 51 \text{ Wm}^{-1}\text{K}^{-1}$ at nanometer length scale of $L = 50 \text{ nm}$ (at 300 K) is observed in Fig. 9.2b. Nanoscale thermal conductivity of BC₅ is more than a factor of 2 higher than silicon as seen in Fig. 9.4 where we compare the phonon meanfreepath dependence of thermal conductivity accumulation in BC₅ and silicon. In silicon, phonons with meanfreepath below 100 nm contribute only $\sim 40 \text{ W/mK}$ at 300 K; in BC₅, however, phonons in

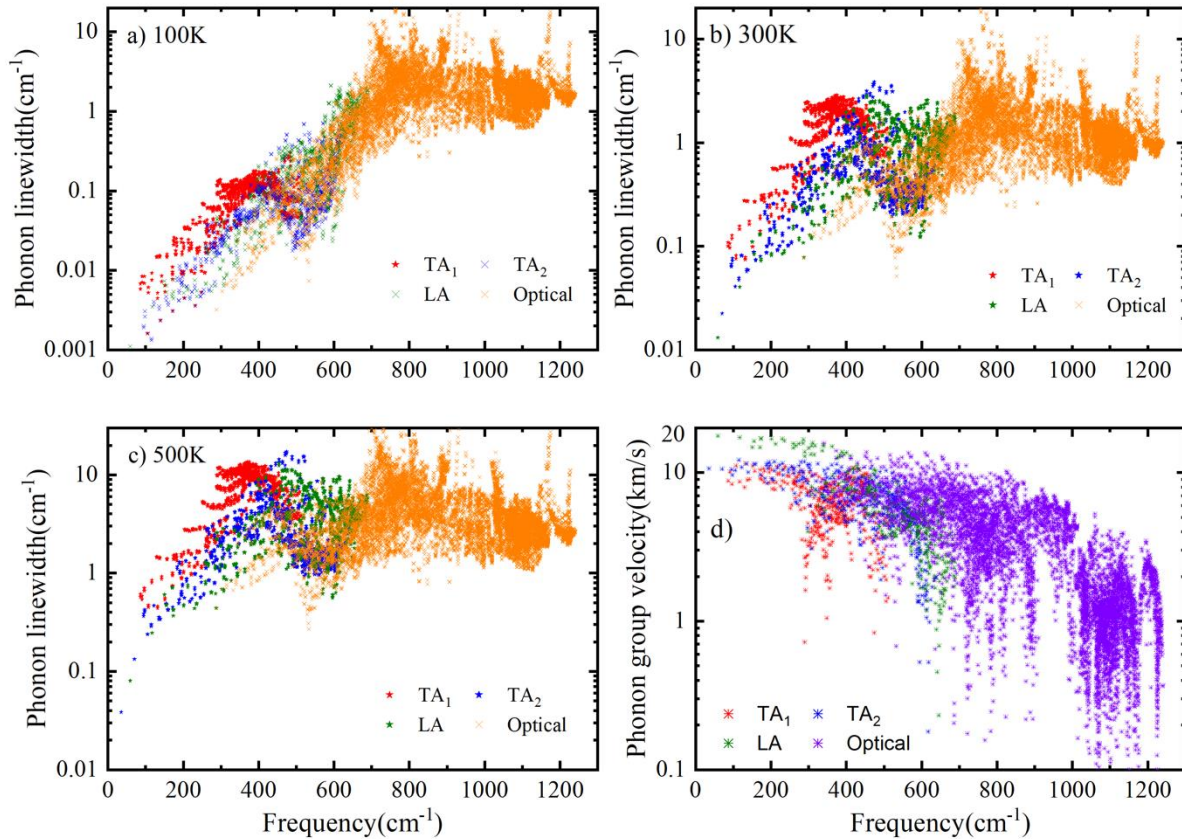


Figure 9.6 Phonon linewidths of transverse acoustic, longitudinal acoustic and optical phonon modes at a) 100 K b) 300 K c) 500 K. d) Phonon group velocity of all phonon modes

the same meanfreepath range, contribute a much higher value of ~ 95 W/mK along a-axis in BC₅. This higher nanoscale thermal conductivity of BC₅ provides promising new avenues for achieving efficient nanoscale thermal management.

This much higher nanoscale thermal conductivity in BC₅ is found to be due to the dominant role played by optical phonons in conducting heat in BC₅. At 500 K and 1000 K, optical phonons contribute 54% and 57.3%, respectively, to overall k along a-axis. This is in contrast to typical semiconductors like silicon, where optical phonon contribution to k is in the range of $\sim 5\%$ ¹⁶⁴ at 300 K. Large contribution of optical phonons can also be seen in Figures 5a and b which show the spectral distribution of k as well as percentage contribution of transverse acoustic (TA), longitudinal acoustic (LA) and optical phonon modes to overall k . At $T > 300$ K, optical phonons have a considerable contribution to overall thermal conductivity.

First-principles computations reveal that this dominant contribution of optical phonons to overall thermal conductivity in BC₅ is due to a combination of high optical phonon velocities (Fig. 9.6d) and comparable optical phonon scattering rates to acoustic phonons at temperatures greater than 300 K (Fig. 9.6a-c). This second effect is particularly interesting, since higher optical phonon frequencies typically result in optical phonon scattering rates to be significantly larger than acoustic phonons. While at 100 K, optical phonon scattering rates in BC₅ are indeed higher than acoustic phonons (Fig. 9.6a), as temperature increases optical-phonon scattering rates increase at a much slower rate compared to acoustic phonons, causing optical and acoustic phonon scattering rates to become comparable (Fig. 9.6b and c).

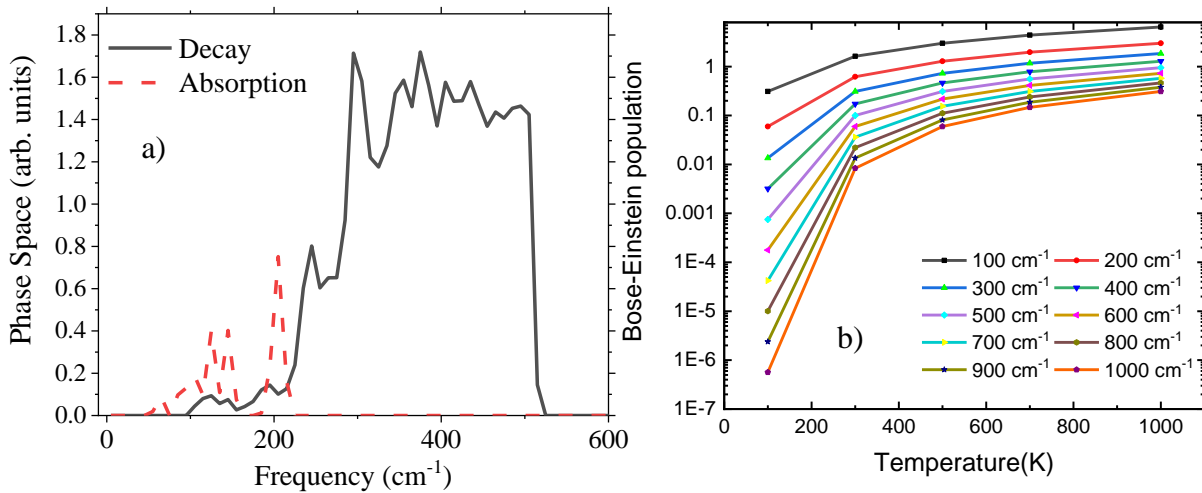


Figure 9.7: a) Scattering Phase space and b) Bose-Einstein population of phonons in BC₅.

This weak dependence of optical phonon scattering rates on temperature and comparable scattering rates of optical and acoustic phonons in BC_5 at $T > 100$ K can be understood by observing that optical phonons in BC_5 have significantly higher frequencies than in materials like silicon. This causes optical phonons in BC_5 to scatter by decaying into phonon modes which also have high frequencies. In Fig. 9.7a we show the dominant contributions to scattering phase space (indicative of the number of scattering channels) of an optical phonon mode with wavevector $q = (0.25, 0, 0)(2\pi/a)$ (where a is the lattice parameter) and frequency $\omega = 1021.6 \text{ cm}^{-1}$. A phonon mode with frequency ω can scatter either by an absorption process (energy conservation: $\omega + \omega' = \omega''$) or by a decay process (energy conservation: $\omega = \omega' + \omega''$) represented by the first and second delta functions in k equation 4.2. The x -axis of Fig. 9.7a corresponds to lower of the two frequencies ω' and ω'' (denoted by ω' in Fig. 7a) involved in the scattering of above outlined optical phonon mode with frequency ω . The high frequency of the optical phonon (in Fig. 9.7a) ensures that frequencies of phonons involved in the decay channels are also high (in the range of 400 cm^{-1}). It is also clearly visible that decay channels make a large contribution to overall scattering phase space of optical phonons.

The relative insensitivity of optical phonon linewidths to temperature can now be understood by noticing that the scattering rates due to decay processes are proportional to $1 + n_{\lambda'} + n_{\lambda''}$ (second term in Equation 4.2). The high frequencies of the phonons ($\sim 400 \text{ cm}^{-1}$ as seen in Fig. 7a) involved in decay of optical phonons causes their populations ($n_{\lambda'}$ and $n_{\lambda''}$) to be remain less than 1.0 even as the temperature increases from 100 K to 800 K (Fig. 9.7b). The presence of a constant prefactor of 1 in the decay term $1 + n_{\lambda'} + n_{\lambda''}$, then ensures that the overall magnitude

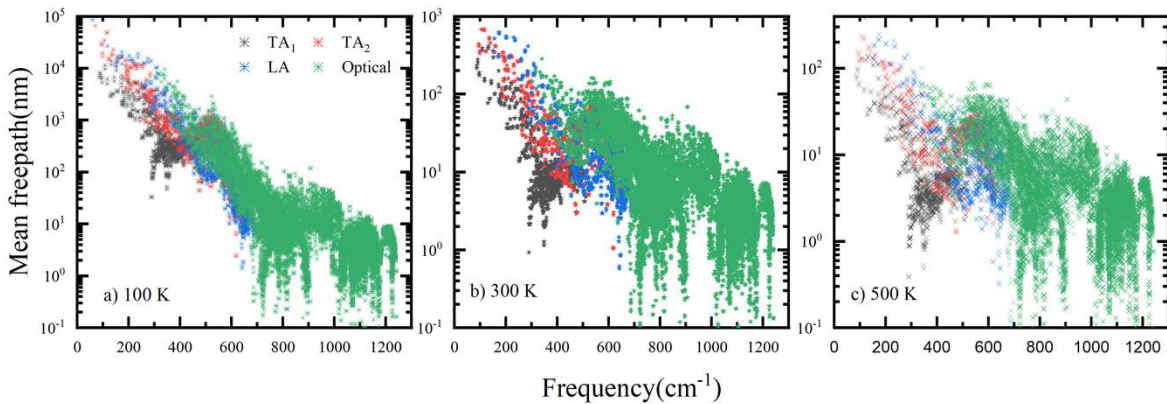


Figure 9.8: Phonon meanfreepaths in BC_5 at a) 100 K b) 300 K and 500 K.

of the term, $1 + n_{\lambda'} + n_{\lambda''}$, does not increase significantly over the temperature range of 100 – 800 K, due to the populations, $n_{\lambda'}$ and $n_{\lambda''}$, not exceeding 1.0 over this temperature range. This causes the linewidths of optical phonons to increase slowly with temperature.

For acoustic phonons, however, the dominant scattering mechanism involves absorption scattering channels, which have a population dependence of $n_{\lambda'} - n_{\lambda''}$ (first term in Equation 4.2).

Acoustic phonon scattering rates thus increase in direct proportion to the increase in phonon populations with temperature resulting in a strong increase in linewidths of acoustic phonons. This coupled with only a small increase in linewidths of optical phonons with increase in temperature, causes the linewidths of the two phonon modes to become comparable at temperatures of 300 K and higher (Fig. 9.6). These results along with high phonon group velocities of optical phonons and a

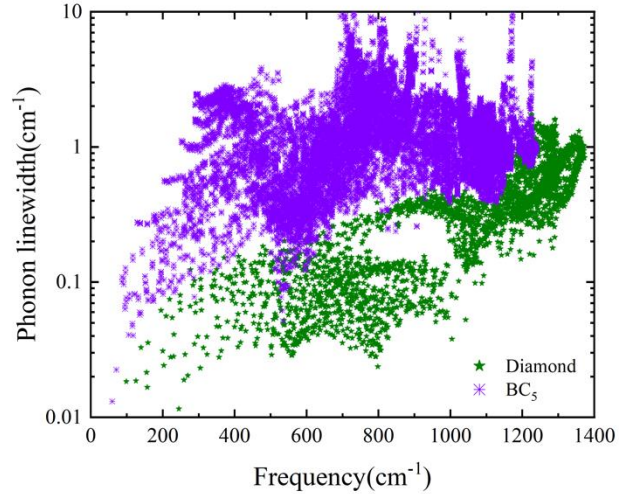


Figure 9.9: Phonon linewidths of BC₅ and Diamond

large phonon density of states of optical phonon modes at frequencies $\omega > 500 \text{ cm}^{-1}$ causes optical phonon modes to be a dominant heat carrying channel for the BC₅ system.

Optical phonon meanfreepaths in BC₅ are in the range of nanometers (tens of nanometers) as seen in Fig. 9.8. The large optical phonon contribution to thermal conductivity coupled with optical phonon meanfreepaths being in the nanometer regime, leads to a large contribution to k in nanoscale regime in BC₅. Furthermore, as temperature increases to 300 K and higher, the large increase in acoustic phonon linewidths also causes their meanfreepaths to decrease to nanometers (Fig. 9.8), further contributing to high nanoscale k in BC₅. Though the hardness of BC₅ is comparable to diamond, its thermal conductivity is much lower than diamond. The presence of large number of optical phonon branches, results in a dramatic increase in scattering phase space, resulting in phonon scattering rates being significantly larger in BC₅ than in diamond (Fig. 9.9).

9.3 CONCLUSION

In summary, using first principles calculations, we analyzed the thermal conductivity of an ultrahard BC₅ by solving the Boltzmann transport equation exactly. At room temperature, we report a high thermal conductivity of 169 Wm⁻¹K⁻¹ for the bulk BC₅ and 51 Wm⁻¹K⁻¹ at the nanometer length scales of L= 50 nm. Ultrahard BC₅ will be a promising material for thermal management due to its high thermal conductivity. We also reveal the contributions of optical phonons to overall thermal conductivity to be dominant at high temperatures. At 500 K, optical phonons contribute ~54% to the overall thermal conductivity. This large contribution of optical phonons to overall k was found to be due to comparable group velocities and scattering rates to acoustic phonons at temperatures greater than 300 K. The comparable scattering rates of optical phonons arise from the particular population dependence of decay channels involved in scattering of optical phonons. The large contribution of optical phonons coupled with their meanfreepaths being in the nanometer regime leads to high nanoscale thermal conductivity in BC₅. These results may lead to potential applications of BC₅ in nanoscale thermal management.

CHAPTER 10 – THERMAL CONDUCTIVITY OF *h*-BC₂P- A FIRST PRINCIPLES STUDY

Carbon based materials such as diamond¹⁷⁷⁻¹⁷⁹, graphene¹⁸⁰⁻¹⁸² and stacked-graphene¹⁸³ (graphene nanoplatelets) exhibit ultrahigh thermal conductivity due to light mass of carbon (C) atom and strong C-C bonds. Likewise, boron based III-V compound semiconductors such as boron nitride (BN)¹⁸⁴, boron phosphide (BP)^{70, 81, 159} and boron arsenide (BAs)^{157, 185} have very high thermal conductivity due to light mass of Boron atom and due to a phonon bandgap in vibrational spectra of these materials which suppresses scattering of acoustic phonons by optical phonons thus leading to high acoustic phonon lifetimes. Recently, ultra-high thermal conductivities of 2305 Wm⁻¹K⁻¹ and 4196 Wm⁻¹K⁻¹ were reported¹³⁷ for bulk ultra-hard hexagonal BC₂N(*h*-BC₂N) at 0 GPa and 150 GPa respectively. Similarly, for monolayer BC₂N, high thermal conductivities of 1275.79 Wm⁻¹K⁻¹ and 893.9 Wm⁻¹K⁻¹ were reported along the zigzag and armchair directions, respectively. These results provide motivation to further explore thermal conductivity of III-IV-V compounds. In this work we explore thermal conductivity of hexagonal BC₂P.

In this work¹⁸⁶, thermal conductivity of bulk hexagonal BC₂P is computed from first-principles by deriving harmonic (2nd order) and anharmonic (3rd order) interatomic force interactions from first-principles and using them along with an exact solution of the phonon Boltzmann transport equation

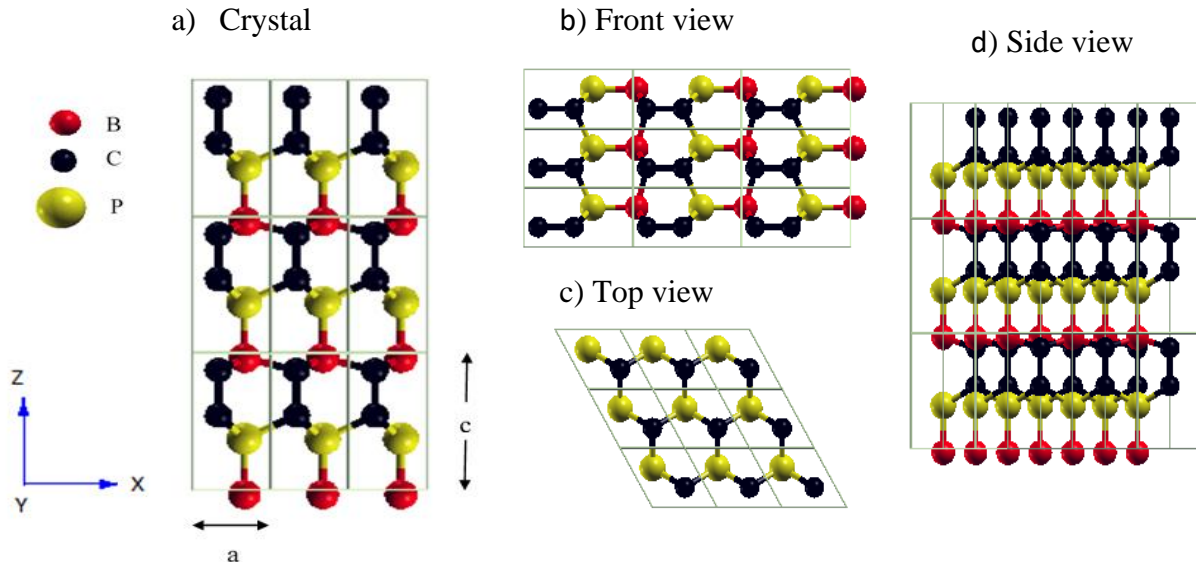


Figure 10.1: a) Atomic arrangements of *h*-BC₂P with 3 x 3 x 3 supercell with lattice constants $a = 5.2686$ bohr and $c/a = 1.686$ b) front view c) top view d) side view. Red, black and yellow sphere represents boron, carbon and phosphorous respectively.

(PBTE). We find an anisotropic high thermal conductivity (k) of $162 \text{ Wm}^{-1}\text{K}^{-1}$ and $52 \text{ Wm}^{-1}\text{K}^{-1}$ along directions perpendicular and parallel to c -axis, at 0 GPa. Interestingly, optical phonons are found to contribute 30% ($\sim 50 \text{ Wm}^{-1}\text{K}^{-1}$) and 14.5% ($\sim 7.54 \text{ Wm}^{-1}\text{K}^{-1}$) at 300 K, to overall thermal conductivity along directions perpendicular and parallel to c -axis, respectively, due to their high group velocities. Finally, a high k value of $68 \text{ Wm}^{-1}\text{K}^{-1}$ at nanometer length scale of 100 nm (at 300 K) shows that BC_2P will be a promising material for thermal management in nanoelectronics.

10.1 COMPUTATIONAL METHODS

Computations were performed using norm-conserving pseudopotentials and exchange-correlation was computed in the local density approximation¹⁸⁷. The geometry of the hexagonal BC_2P with 4 atoms unit cell, was optimized until forces on all atoms were less than 10^{-6} Ry/bohr . Plane-wave energy cutoff of 80 Ry and $12 \times 12 \times 8$ Monkhorst-Pack¹¹⁵ k -point mesh were used for electronic structure calculations. Optimized lattice constant (crystal structure of Fig. 10.1) of BC_2P was obtained to be $a=5.2686 \text{ bohr}$ with $c/a=1.686$. For k calculations, a $21 \times 21 \times 14$ q -mesh was used and

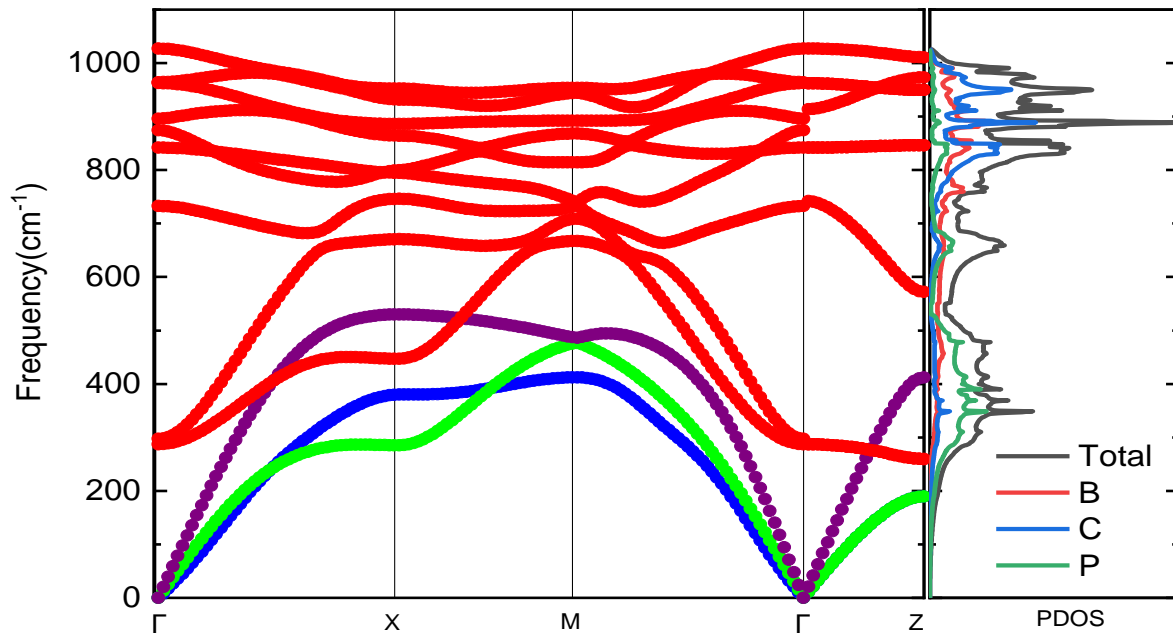


Figure 10.2: Phonon dispersion curve and phonon density of states for the h - BC_2P . Blue, green and purple color in phonon dispersion represent the TA_1 , TA_2 and LA phonon modes respectively. Red, blue and green in PDOS represent the vibrational frequencies of B, C and N atoms respectively.

iterations in the exact solution of the PBTE were performed until Δk between consecutive iterations diminished to below $1.0e^{-5}$. Casimir scattering¹⁴⁵ is imposed to include the effect of boundary scattering for computing length dependent thermal conductivity.

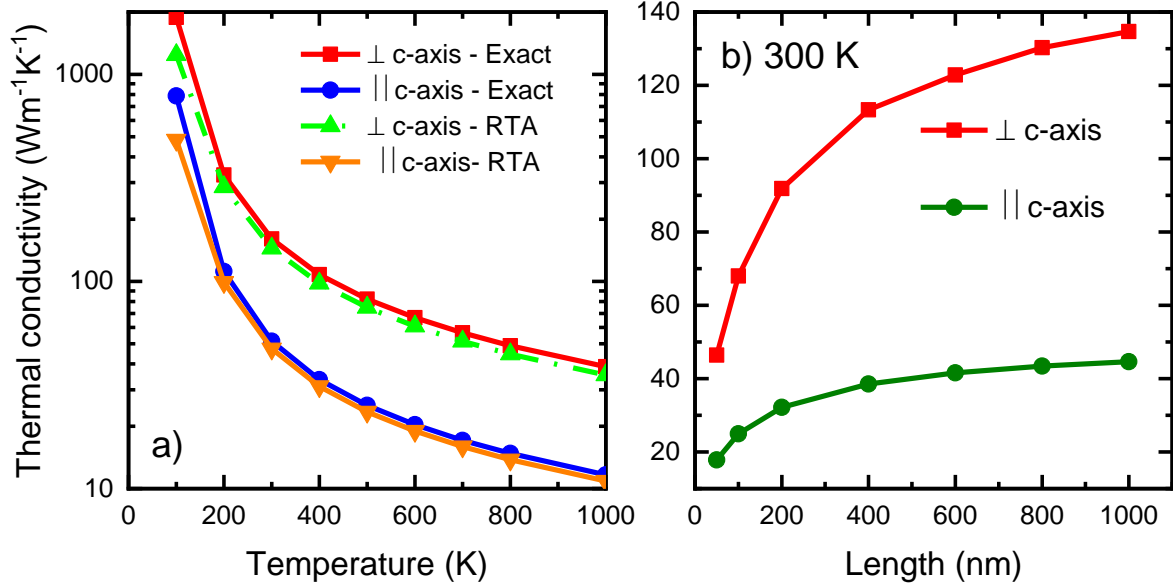


Figure 10. 3a) Temperature dependence and b) Length dependence of thermal conductivity along and perpendicular to c-axis of *h*-BC₂P.

10.2 RESULTS

10.2.1 Phonon dispersion and Lattice constants

Phonon dispersion and phonon density of states for hexagonal BC₂P are shown in Fig 10.2. Positive phonon frequencies indicate stability¹⁸⁸ of computed *h*-BC₂P crystal structure. Phonon modes at higher frequencies (above 750 cm⁻¹) are mainly dominated by C and B atoms due to light mass and stiff C-C and B-C bonds, whereas P atoms dominate lower frequencies (less than 500 cm⁻¹) due to heavy mass and moderate bond strengths of B-P and C-P. Elastic constants of hexagonal BC₂P at 0 GPa are computed to be, $C_{11}=675$ GPa, $C_{33}=680.6$ GPa, $C_{44}=198$ GPa, $C_{66}=305$ GPa, $C_{12}=65.0$ GPa, $C_{13}=30.8$ GPa which satisfies the Born stability criteria¹⁴⁷ of $C_{66}=(C_{11}-C_{12})/2$, $C_{11} > C_{12}$, $C_{33}(C_{11}+C_{12}) > 2(C_{13})^2$, $C_{44} > 0$, $C_{66} > 0$. Young modulus (E), bulk modulus (B), shear modulus (G) and poisson ratio based on Voigt-Ruess-Hill approximation¹⁴⁴ are 582.2 GPa, 253.6 GPa, 260.6 GPa and 0.117 respectively. These values are higher than silicon¹⁸⁹, germanium¹⁸⁹ and silicon carbide¹⁹⁰.

10.2.2 Lattice thermal conductivity

Computed thermal conductivity of the h -BC₂P is reported in Fig 10.3. Figure 10.3a shows the temperature dependent thermal conductivity of h -BC₂P along directions perpendicular and parallel to c -axis. At 300 K, computed thermal conductivity of $162 \text{ Wm}^{-1}\text{K}^{-1}$, perpendicular to c -axis, is almost 3 times higher than the value, parallel to c -axis, of $52 \text{ Wm}^{-1}\text{K}^{-1}$. This is due to the higher phonon frequencies of TA, LA and optical phonons modes, in a direction perpendicular to c -axis, relative to parallel to c -axis, as seen in the computed phonon dispersion. thermal conductivity of h -BC₂N is also higher than that of silicon⁸⁶. Perpendicular to c -axis, TA₁, TA₂ and LA phonon modes contribute 19.8%, 27.5% and 35.7% to overall thermal conductivity while along c -axis, the corresponding contributions are 23%, 30% and 32% to overall k . Interestingly, at 300 K, optical phonon modes contribute 30% and 14.5% to overall thermal conductivity, perpendicular and parallel to c -axis, respectively. This contribution is significantly higher than typical semiconductor materials such as silicon, where optical phonons contribute $\sim 5\%$ to overall k . This is due to the high phonon group velocities of optical phonons (Fig. 10.4a) and optical phonon linewidths being comparable to that of acoustic phonons, in the frequency range of $\sim 300\text{-}550 \text{ cm}^{-1}$ (Fig. 10.4b).

An advantage of BC₂P is its relatively high thermal conductivity at nanometer length scales. Length dependence of thermal conductivity was calculated by introducing Casimir

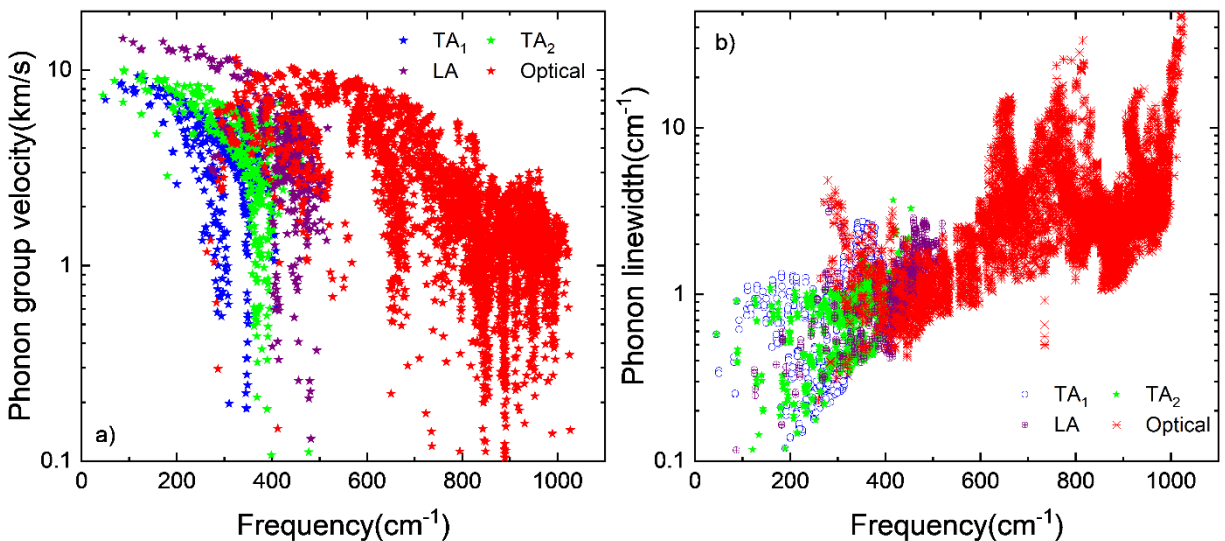


Figure 10.4a) Phonon group velocity and b) phonon linewidth of TA, LA and optical phonon modes of h -BC₂P at 300 K.

scattering $1/\tau_{\text{boundary}} = |v|/L$, where v is the phonon velocity and L is the system size. Length dependent thermal conductivity is shown in Fig 10.3b. We observe that at a length scale of 100 nm, the predicted thermal conductivity of $\sim 68 \text{ Wm}^{-1}\text{K}^{-1}$ is significantly high. This can lead to potential avenues for use of BC_2P in nanoscale thermal management applications. This high nanoscale thermal conductivity of BC_2P is due to the relatively large k contribution of optical phonons, which typically have meanfreepaths in the nanometer regime.

10.3 CONCLUSION

Thermal conductivity of hexagonal $\text{BC}_2\text{P}(h\text{-BC}_2\text{P})$ is computed by solving phonon Boltzmann transport equation exactly coupled with force-constants derived from first principles calculations. We report an anisotropic thermal conductivity (k) of $162 \text{ Wm}^{-1}\text{K}^{-1}$ and $52 \text{ Wm}^{-1}\text{K}^{-1}$ along directions perpendicular and parallel to c -axis of BC_2P respectively. This high thermal conductivity is due to the high frequency and phonon group velocity arising from light mass of the constituent atoms (B, C, P) and stiff C-C, B-C and B-P bonds. Anisotropy in k is due to higher phonon frequencies and group velocities along direction perpendicular to c -axis relative to the parallel direction. Moreover, optical phonon modes are found to contribute significantly to k along directions both perpendicular to c -axis (30%) and parallel to c -axis (14.5%) at 300 K. Finally, a high room temperature thermal conductivity of $68 \text{ Wm}^{-1}\text{K}^{-1}$ at 100 nm length scale, makes BC_2P attractive for thermal management in nanoelectronics.

CHAPTER 11 – THERMAL CONDUCTIVITY OF MAGNESIUM SELENIDE(MgSe) – A FIRST PRINCIPLES STUDY

Wide bandgap materials have attracted various scientific and technological interest due to its reduced energy consumption, low power loss and can accommodate higher operating temperatures, high switching speed and high voltage, high frequencies¹⁹¹⁻¹⁹³ and thermoelectric applications¹⁹⁴⁻¹⁹⁷. Magnesium chalcogenides such as magnesium sulphide (MgS), magnesium selenide (MgSe) and magnesium telluride (MgTe) are wide bandgap semiconductors which are extensively studied for their electronic¹⁹⁸⁻²⁰⁰, magnetic¹⁹⁹, optical¹⁹⁸, structural^{199, 201-203} and vibrational^{204, 205} properties. Understanding thermal conductivity of these materials is critical for optimum thermal design of devices based on these materials. There are, however, limited studies on thermal properties which is critical for wide range of applications such as thermoelectrics²⁰⁶⁻²¹¹, thermal management systems^{17, 136, 154, 156, 158, 212}, opto-electronics²¹³, thermal barrier coatings²¹⁴⁻²¹⁶ and solar cells²¹⁷⁻²¹⁹ etc., which inspired us to compute it. In this work^{220, 221}, we report the temperature and length dependence thermal conductivity of magnesium selenide (MgSe) with different crystalline phases using first principles calculations and phonon Boltzmann transport equation. MgSe exists in four crystalline phases; zincblende(ZB), rocksalt(RS), wurtzite(WZ) and nickel arsenic(NiAs)²⁰⁴. We also report the length dependence thermal conductivity for its nanostructures. At 300 K, the first principles computed thermal conductivities of MgSe are – a) 4.54 Wm⁻¹K⁻¹ along a-axis and 6.37 Wm⁻¹K⁻¹ along c-axis for NiAs structure, b) 11.89 Wm⁻¹K⁻¹

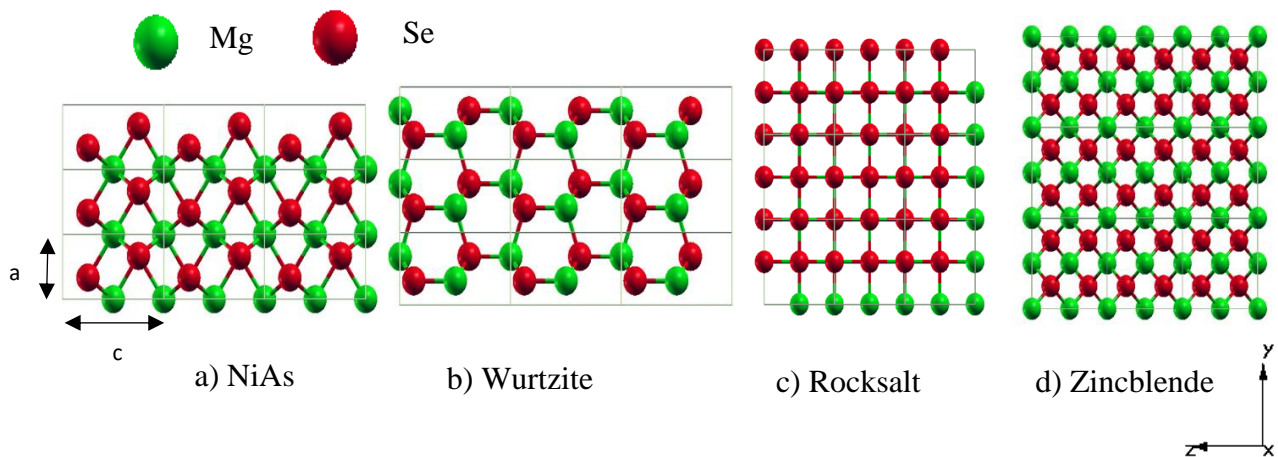


Figure 11.1 a-d): Crystal structure of MgSe with crystalline phases; NiAs ($a=7.216$ bohr, $c/a=1.6672$), wurtzite ($a=7.924$ bohr, $c/a=1.6149$), rocksalt ($a=10.2617$ bohr) and zincblende ($a=11.16$ bohr) respectively.

for Rocksalt structure, c) $19.58 \text{ Wm}^{-1}\text{K}^{-1}$ a-axis and $20.39 \text{ Wm}^{-1}\text{K}^{-1}$ along c-axis for WZ structure and d) $21.27 \text{ Wm}^{-1}\text{K}^{-1}$ for Zinc-Blende structure. Understanding of differences in thermal conductivity is achieved through analysis of differences in phonon scattering arising from different phonon dispersions for different structures.

11. 1 COMPUTATIONAL DETAILS

All the first principles calculations were performed using QUANTUM ESPRESSO⁸⁸ package. Norm-conserving pseudopotential with local density approximation (LDA)¹⁸⁷ exchange-correlation functional is used for electronic calculations. The geometries of the zinc-blende and rocksalt MgSe with 2 atom unit cell and wurtzite and NiAs structures with 4 atom unit cell, were optimized until forces on all atoms were less than 10^{-6} Ry/bohr. Plane-wave energy cutoff of 70 Ry was used for electronic calculations. Monkhorst-Pack¹¹⁵ k -point mesh sizes of $8 \times 8 \times 8$ and $12 \times 12 \times 8$ were used for zinc-blende/rocksalt and wurtzite/NiAs structures, respectively, to

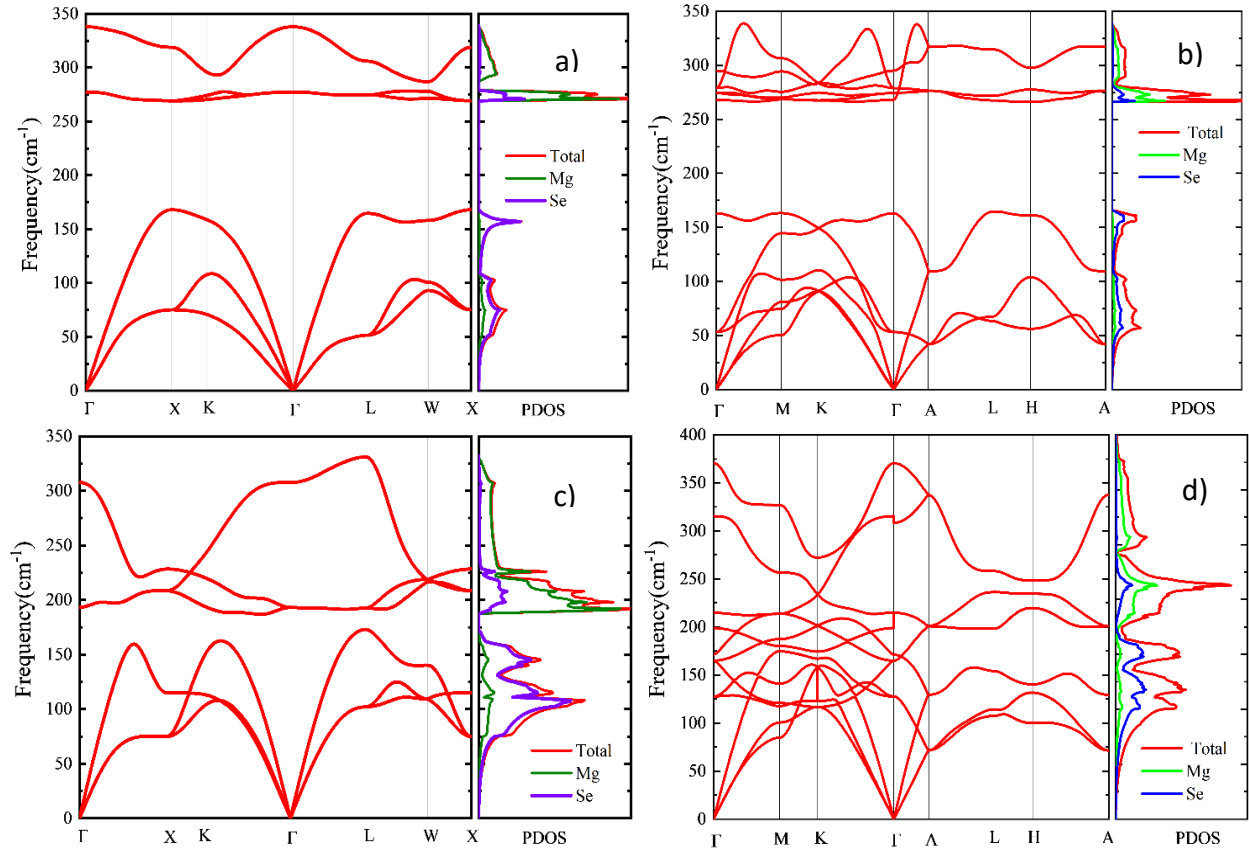


Figure 11.2: Phonon dispersion and phonon density of states(PDOS) of MgSe with crystalline phase; a) zincblende b) wurtzite c) rocksalt and d) nickel arsenic.

integrate over the Brillouin zone. Relaxed structures with equilibrium lattice constants of MgSe with different lattice crystal phases are shown in Fig 11.1 and also listed in Table 11.1 (in excellent agreement with previously published values^{200, 204, 222-224}). Lattice thermal conductivity (k) was computed by solving phonon Boltzmann transport equation (PBTE)⁹¹ in both single mode relaxation approximation (SMRT)²²⁵ and exactly by using a variational method.

Harmonic force constants were computed on an 8 x 8 x 8 q-grid for ZB and RS systems and on a 9 x 9 x 6 grid for WZ and NiAs structures. Anharmonic force constants were computed on a 4 x 4 x 4 grid for ZB and RS and on a 3 x 3 x 2 grid for WZ and NiAs structures, using D3Q⁸⁹⁻⁹¹ package within QUANTUM-ESPRESSO. Acoustic sum rules were imposed on both harmonic and anharmonic interatomic force constants. Phonon linewidth and lattice thermal conductivity were calculated using ‘thermal2’ package within QUANTUM ESPRESSO. For these calculations, q -mesh of 30 x 30 x 30 was used for ZB and RS structures, while a mesh of 30 x 30 x 20 was used for WZ and NiAs structures. Iterations in the exact solution of the PBTE were performed until Δk between consecutive iterations diminished to below $1.0e^{-5}$. k values were typically converged after 4 iterations. Casimir scattering¹⁴⁵ was imposed to include the effect of boundary scattering for computing length dependent thermal conductivity in the nanoscales. Phonon-isotope scattering is included for the effect of isotope variation with naturally occurring isotopes of Mg and Se²²⁶. Elastic constants were computed using QUANTUM ESPRESSO thermo_pw package. Voigt-Reuss-Hill approximation¹⁴⁴ was used to calculate Bulk modulus, Shear modulus(G), Young’s Modulus(E) and Poisson’s ratio (ν).

11.2 RESULTS

11.2.1 Phonon Dispersion and Lattice Constants

Phonon dispersion and phonon density of states (PDOS) for the MgSe with crystalline phases of zincblende(ZB), wurtzite (WZ), rocksalt(RS) and nickel arsenic(NiAs) are shown in Fig 11.2 a-d. Computed dispersions are in good agreement with previously reported values²⁰⁴. Elastic properties such as Young’s modulus (E), Bulk modulus (B), Shear modulus (G) and Poisson’s ratio based on Voigt-Ruess-Hill approximation are listed in Table 11.1 and are also in excellent agreement with the previously published work²⁰⁴.

Table 11.2: Lattice constants, Bulk modulus(B), Youngs modulus(E), Shear modulus(G) and poisson's(ν) ratio of MgSe with different crystal phase.

S. No	Crystal phase	a (bohr)	c/a	B (GPa)	E(GPa)	G(GPa)	ν
1.	Nickel arsenic (NiAs)	7.216	1.667	67.36	92.8	36.53	0.2703
2.	Wurtzite (WZ)	7.9238	1.615	50.7	55.34	21	0.3182
3.	Rocksalt (RS)	10.2617		67.7	113.07	46.28	0.2216
4.	Zincblende (ZB)	11.16		49.695	47.903	17.933	0.3356

11.2.2 Lattice Thermal Conductivity

Lattice thermal conductivity (k) of MgSe for different crystalline phases is shown in Fig 11.3a. Single-mode relaxation results (SMA) are 5% less than the iterative solution. At room temperature (300K), computed k of pure MgSe is as follows; k_{NiAs} ($4.54 \text{ Wm}^{-1}\text{K}^{-1}$ along a-axis and $6.37 \text{ Wm}^{-1}\text{K}^{-1}$ along c-axis) $< k_{\text{RS}}$ ($11.89 \text{ Wm}^{-1}\text{K}^{-1}$) $< k_{\text{WZ}}$ ($19.58 \text{ Wm}^{-1}\text{K}^{-1}$ along a-axis and $20.39 \text{ Wm}^{-1}\text{K}^{-1}$ along c-axis) $< k_{\text{ZB}}$ ($21.27 \text{ Wm}^{-1}\text{K}^{-1}$). Fig 11.3c shows the length dependent thermal conductivity of MgSe between 10 nm and $10\mu\text{m}$. At 300K and at 100 nm, k of different crystalline

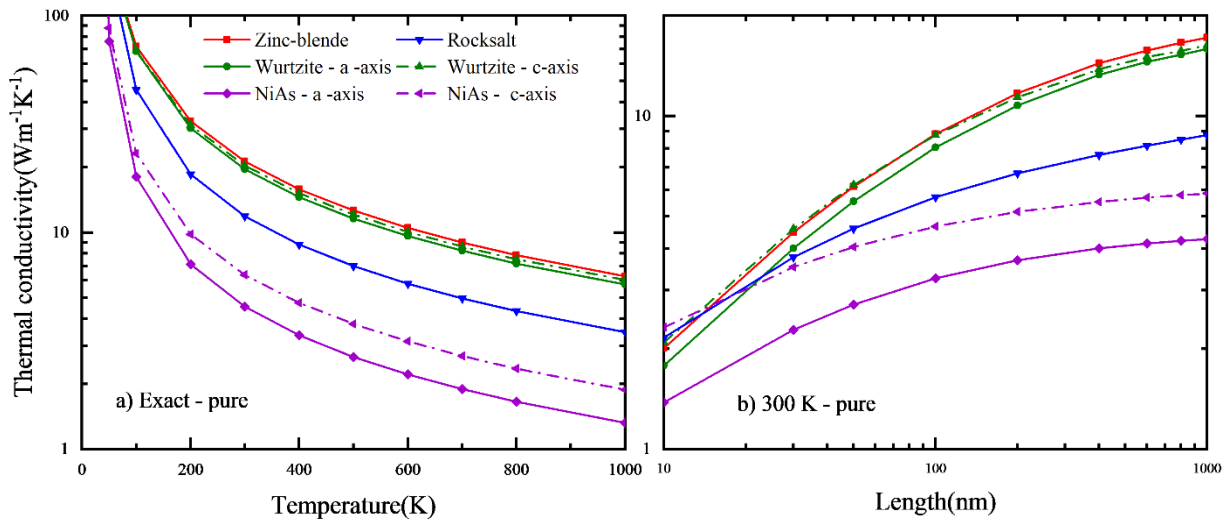


Figure 11.3: Temperature dependent lattice thermal conductivity of MgSe with different crystalline phase with a) iterative solution of BTE c) Length dependent thermal conductivity of MgSe at room temperature(300K).

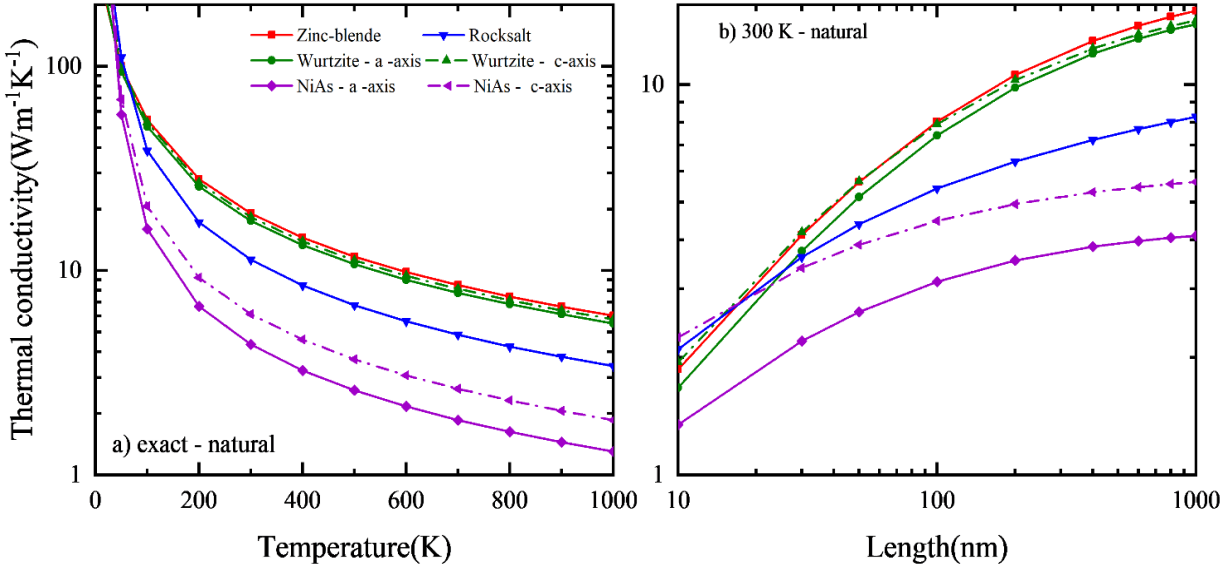


Figure 11.4 a and b) Temperature and length dependent (300 K) thermal conductivity of natural MgSe with isotopic scattering for different crystalline phase.

phases are as follows; k_{NiAs} ($3.25 \text{ Wm}^{-1}\text{K}^{-1}$ along a-axis and $4.67 \text{ Wm}^{-1}\text{K}^{-1}$ along c-axis) $< k_{RS}$ ($5.71 \text{ Wm}^{-1}\text{K}^{-1}$) $< k_{WZ}$ ($8.05 \text{ Wm}^{-1}\text{K}^{-1}$ a-axis and $8.76 \text{ Wm}^{-1}\text{K}^{-1}$ along c-axis) $< k_{ZB}$ ($8.82 \text{ Wm}^{-1}\text{K}^{-1}$).

Lattice thermal conductivity of naturally occurring MgSe, which includes the effect of isotopic disorder is shown in Fig 11.4. Thermal conductivity of naturally occurring MgSe at 300K is as follows; k_{NiAs} ($4.36 \text{ Wm}^{-1}\text{K}^{-1}$ along a-axis and $6.13 \text{ Wm}^{-1}\text{K}^{-1}$ along c-axis) $< k_{RS}$ ($11.31 \text{ Wm}^{-1}\text{K}^{-1}$).

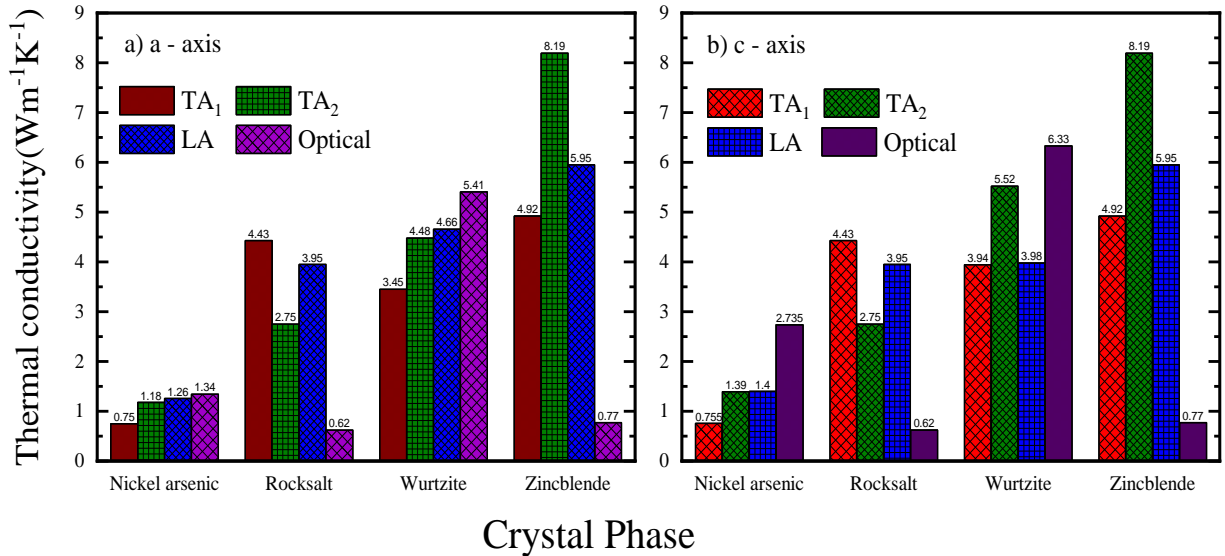


Figure 11.5: Mode contribution thermal conductivity of MgSe at 300K for different crystalline phase.

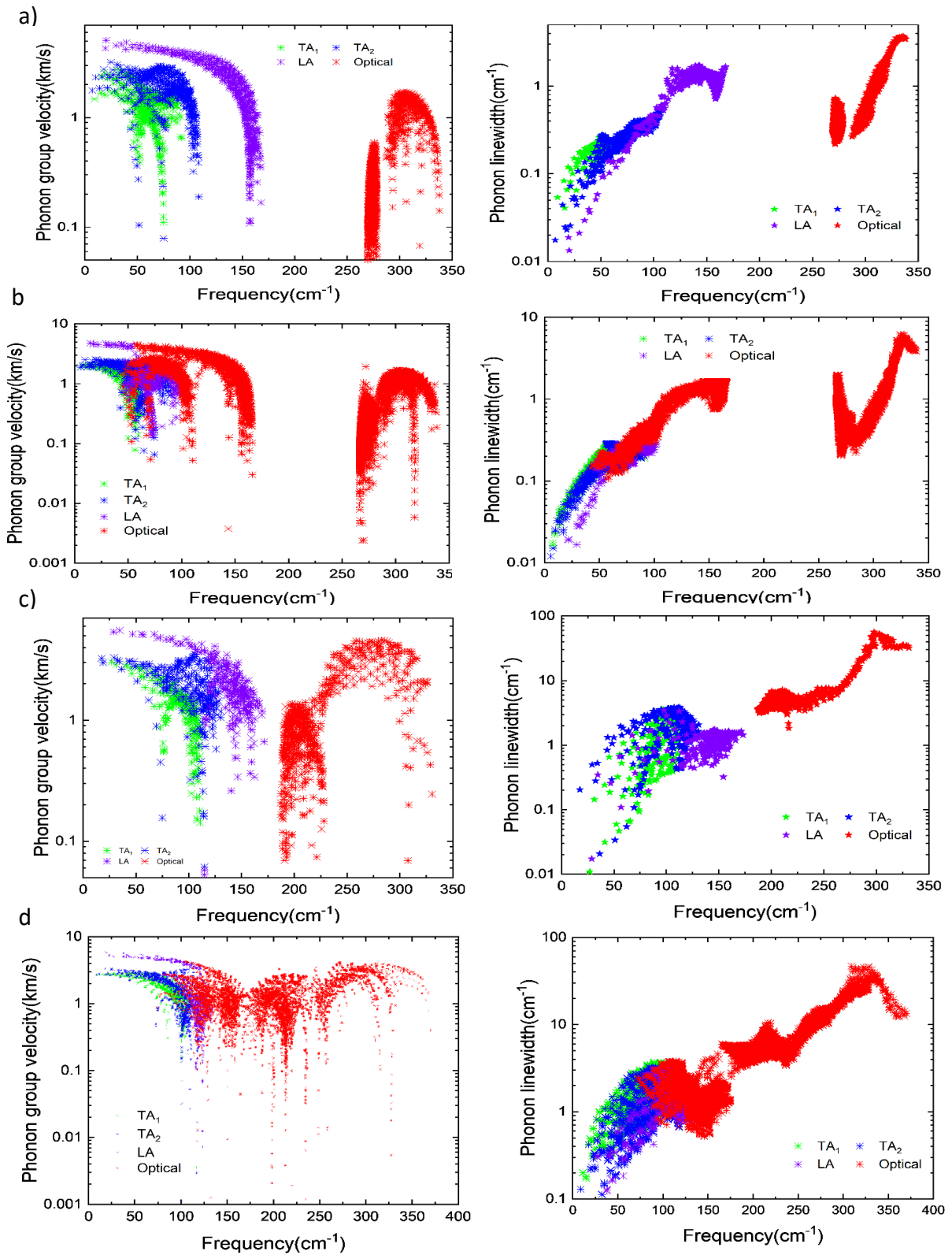


Figure 11.6: Phonon group velocity and scattering of MgSe with crystalline phase; a) zincblende b) wurtzite c) rocksalt and d) nickel arsenic

$1\text{K}^{-1}) < k_{WZ}(17.5\text{ Wm}^{-1}\text{K}^{-1}\text{ a-axis and }18.3\text{ Wm}^{-1}\text{K}^{-1}\text{ along c-axis}) < k_{ZB}(19.04\text{ Wm}^{-1}\text{K}^{-1})$. These

values show that isotopic scattering reduces its lattice thermal conductivity by a maximum of ~10% for ZB and WZ phase.

As seen above, thermal conductivity of the NiAs crystal phase is the lowest, while that of zincblende phase is the highest. Thermal conductivity of MgSe with zincblende crystal structure is 4.68 times that of the NiAs phase along a-axis. In Fig. 11.5, we also compare contributions of different vibration modes to overall thermal conductivity in different crystalline phases. Interestingly, in NiAs and wurtzite MgSe, k contribution from optical phonon is higher than the acoustic phonon modes.

This is mainly due to the suppression of phonon-phonon scattering in zincblende structure mediated by a large phonon bandgap ($\sim 100 \text{ cm}^{-1}$) in the phonon dispersion of zinc-blende structure. We have presented the phonon scattering rates (inverse of phonon lifetime) and phonon group velocities of MgSe with different crystalline phases in Fig 11.6. We can observe from Figs 11.6a and d that, scattering rate of TA_1 and TA_2 for NiAs is approximately one order of magnitude higher

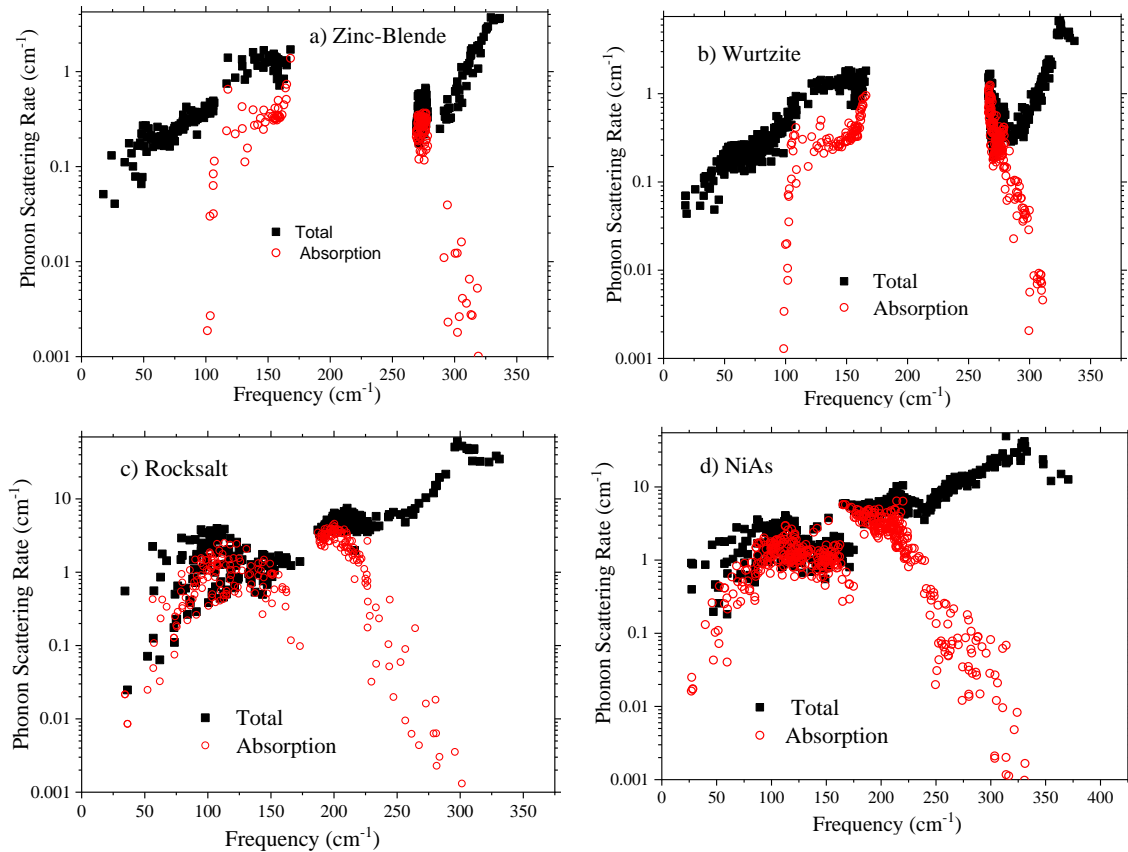


Figure 11.7: Phonon scattering of MgSe with crystalline phase; a) zincblende b) wurtzite c) rocksalt and d) nickel arsenic

than that of the zincblende phase causing a dramatic reduction in thermal conductivity contributions of TA₁ and TA₂ phonon modes in NiAs structure.

The effect can be understood by observing that anharmonic scattering of phonons through the lowest-order three phonon processes can be classified into two categories - absorption scattering process, where a phonon mode ($q\omega$) scatters by absorbing another phonon mode ($q'\omega'$), yielding a higher energy ($q''\omega''$) phonon mode, and decay processes, where a phonon mode decays into two lower energy phonons. These processes satisfy energy and momentum conservation given by, $\omega + \omega' = \omega''$ (energy), $q + q' = q''$ (momentum) for absorption process and $\omega = \omega' + \omega''$ (energy), $q = q' + q''$ (momentum) for decay process.

The large energy gap in the phonon dispersion of zincblende structure suppresses the absorption scattering channels for acoustic phonons involving scattering of an acoustic phonon by absorbing another acoustic phonon to convert into an optical phonon. The large energy gap in the phonon dispersion of the zinc-blende structure prohibits energy conservation ($\omega + \omega' = \omega''$) for such absorption scattering channels. This is seen through an example, where, an acoustic phonon of frequency 100 cm⁻¹ cannot scatter into an optical phonon, even by absorbing the highest frequency acoustic phonon (168.05 cm⁻¹). This is because the lowest optical phonon frequency 269.25 cm⁻¹ is higher than the sum of the frequencies of above two listed acoustic phonons. This elimination of absorption scattering channels in zinc-blende structure dramatically decreases overall scattering rates in zinc-blende case. We have shown this for all crystalline phases in Fig. where we compare the magnitude of absorption scattering channel with the overall scattering rates.

It can be seen that for zincblende and wurtzite structures (with a large bandgap in their phonon dispersions), the magnitude of absorption channels is significantly smaller than for the case of rocksalt and NiAs structures. Below a frequency of 100 cm⁻¹, the absorption channel is seen to be almost completely absent in zinc-blende and wurtzite structures. This smaller rate of absorption scattering in zincblende and wurtzite structures also leads to a smaller overall scattering rate in these structures. At a frequency of 50 cm⁻¹, the overall scattering rate in zinc-blende and wurtzite structures is ~0.1 cm⁻¹, almost an order of magnitude lower, relative to the scattering rate of 1 cm⁻¹ in NiAs structure. The higher scattering rates in rocksalt and NiAs structures (due to smaller or absent phonon band gap) lead to lower thermal conductivity in these crystalline phases.

Higher contribution of optical phonon modes to overall thermal conductivity in NiAs and Wurtzite structures can now be understood in terms of the phonon band gap in these materials. In NiAs structure, the large scattering rates of acoustic phonons (due to absence of a band gap in phonon dispersion), imply that the scattering rates of low frequency optical phonons become comparable to that of acoustic phonons. Significant group velocities of optical phonons in NiAs structure combined with comparable phonon scattering rates to acoustic phonons, leads to high thermal conductivity contribution of optical phonons in NiAs structure. In Wurtzite crystalline phase, the high thermal conductivity of optical phonons arises due to the large phonon band gap in the dispersion. Fig 11.7 shows that some of the optical phonons are below the band gap. Similar to the case of acoustic phonons, these optical phonons also experience inhibited scattering from optical phonons above the band gap.

10.3 CONCLUSION

Thermal conductivity of magnesium selenide (MgSe) with four crystalline phases; zincblende, rocksalt, wurtzite and nickel arsenic were computed by first principles calculations with phonon Boltzmann transport equations. Our first principles calculations show a low thermal conductivity of less than $\sim 20 \text{ Wm}^{-1}\text{K}^{-1}$ for all the crystalline phases of MgSe. Isotopic disorder scattering has minimal effect (less than 10%) to its overall thermal conductivity. We systematically investigated the phonon group velocity, phonon scattering rate and mode dependent thermal conductivity of MgSe. Our first principles calculations show that, NiAs and wurtzite has higher contributions from optical phonons than NiAs and rocksalt. At nanometer length scales such as 100 nm, thermal conductivity of less than $3.25 \text{ Wm}^{-1}\text{K}^{-1}$ for MgSe with NiAs crystalline phase shows a promising nature of MgSe for thermoelectric applications.

CHAPTER 12- THERMAL CONDUCTIVITY OF MAGNESIUM TELLURIDE(MgTe) – A FIRST PRINCIPLES STUDY

Magnesium chalcogenides-based semiconductors have attracted both scientific and technological applications^{199, 204, 227}. Magnesium^{206, 207, 209, 228} and Telluride^{208, 210, 217, 219, 229-231} based thermoelectric and photovoltaic materials are getting attention among the scientific community due to its ultra-low thermal conductivity and tunable electronic bandgap. Magnesium telluride(MgTe) is extensively studied for its structural^{198, 199, 203, 227}, electronic^{198, 199, 204, 227}, elastic¹⁹⁸, magnetic^{199, 227}, optical¹⁹⁸ and vibrational^{204, 205} properties. Despite these extensive studies, thermal conductivity of MgTe is unknown. Thermal conductivity of a material is critical for wide varieties of application such as thermal management system^{17, 68, 136, 154, 157, 212, 232, 233}, thermoelectrics²³⁴⁻²³⁶, opto-electronics²¹³ and solar cells^{218, 237} etc., MgTe are known to exist in four crystalline phases such as zinc-blende (ZB), rocksalt (RS), wurtzite (WZ)^{204, 238, 239} and nickel arsenic (NiAs). In this work²⁴⁰, we report bulk and nanoscale thermal conductivity of all the four crystalline phases of MgTe using density functional theory and phonon Boltzmann transport equation. We also report an ultra-low thermal conductivity of MgTe at nanometer length scales. We systematically investigated the elastic constants, phonon group velocity, phonon bandgap and phonon scattering rate (inverse of phonon lifetime) for all the crystalline phases. At 300 K, bulk thermal conductivity of 2.645 (NiAs), 6.26 (RS), 8.83 (WZ) and 10.05 (ZB) $\text{Wm}^{-1}\text{K}^{-1}$ shows that MgTe will be a promising thermoelectric material. These results have important implications for

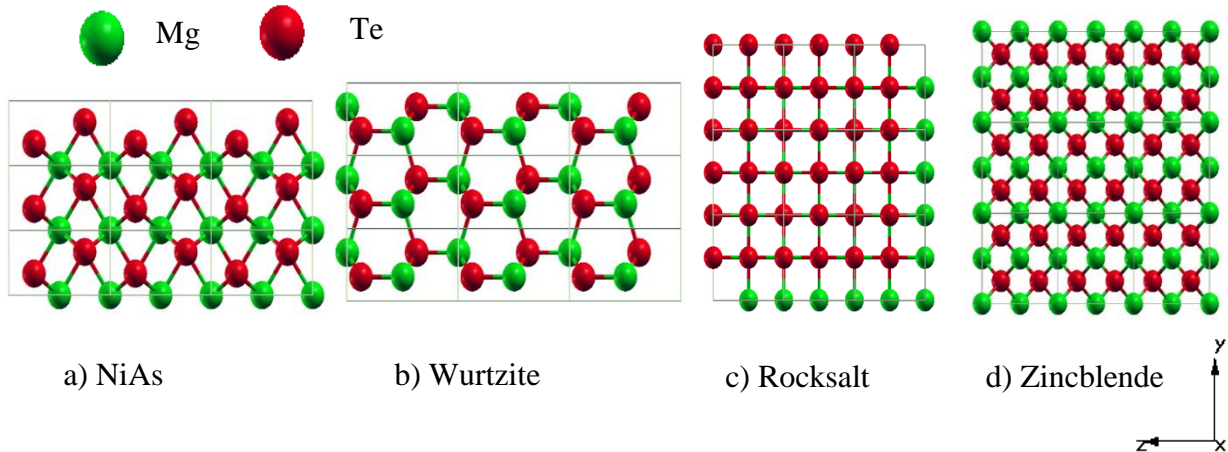


Figure 12.1 a-d): Crystal structure of MgTe with crystalline phases; NiAs ($a=7.8585$ bohr, $c/a=1.6281$), wurtzite ($a=8.5287$ bohr, $c/a=1.6286$), rocksalt ($a=11.0985$ bohr) and zincblende ($a=12.073$ bohr) respectively.

applications of MgTe in thermoelectric energy conversion techniques, solar-cells and other optoelectronics.

12.1 COMPUTATIONAL DETAILS

All the first principles calculations were performed using QUANTUM ESPRESSO⁸⁸ package. Norm-conserving pseudopotential with local density approximation (LDA)¹⁸⁷ exchange-correlation functional is used to approximate the MgTe. The geometry of the zinc-blende and rocksalt MgTe with 2 atoms (4 atoms for wurtzite and NiAs) unit cell were optimized until forces on all atoms were less than 10^{-6} Ry/bohr. Plane-wave energy cutoff of 80 Ry and $8 \times 8 \times 8$ ($12 \times 12 \times 8$) Monkhorst-Pack¹¹⁵ k -point mesh were used integrate over the Brillouin zone. Relaxed structure with equilibrium lattice constants of MgTe with different lattice crystal phases are shown

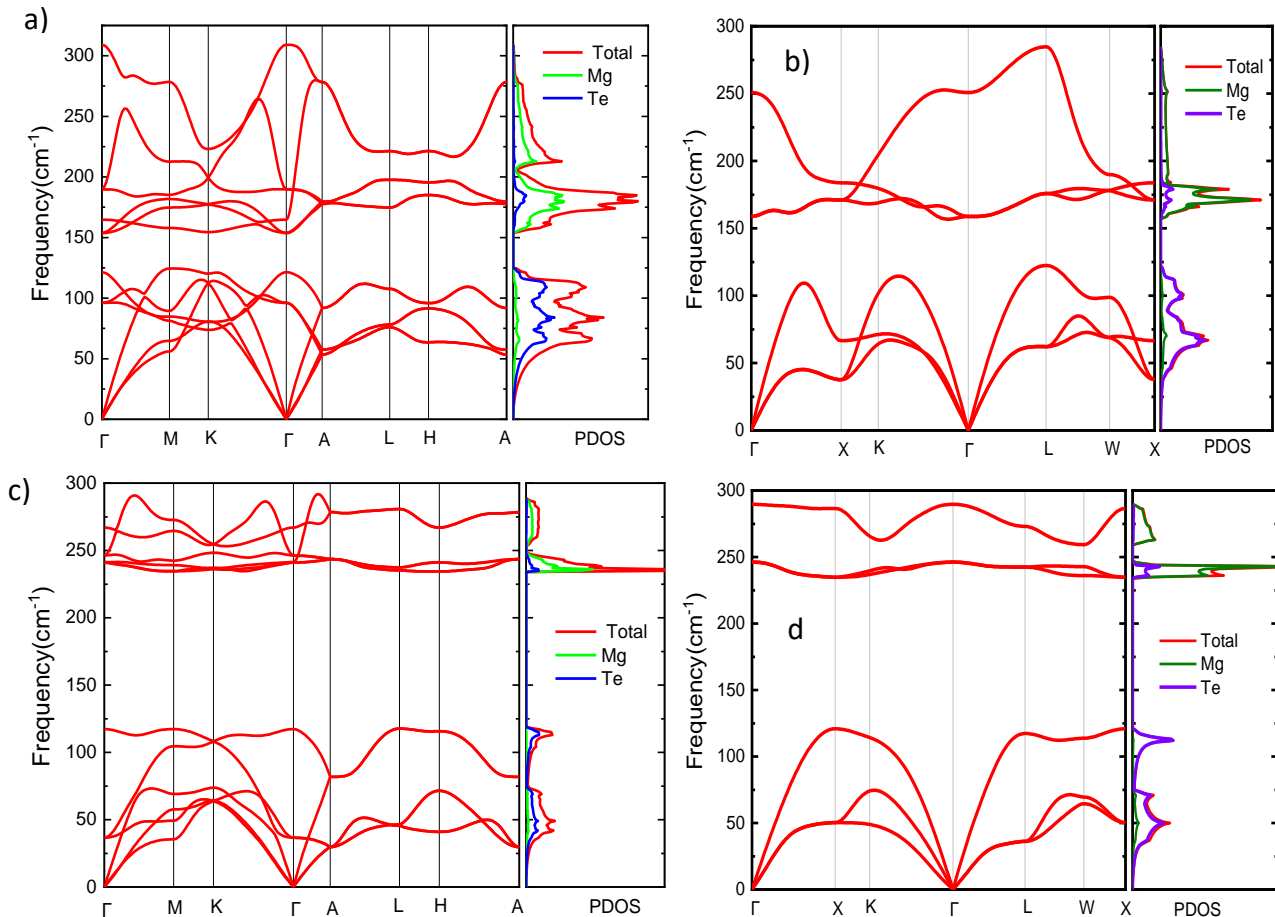


Figure 12.2: Phonon dispersion and phonon density of states for the MgTe with crystal phase a) nickel arsenic b) rocksalt c) wurtzite and d) zincblende

in Fig 12.1 and also listed in Table 12.1 which are in excellent agreement with previously published values G.P.Srivatsava *et.al*²⁰⁴.

Lattice thermal conductivity(k) was computed by solving phonon Boltzmann transport equation (PBTE)⁹¹ in both single mode relaxation approximation (SMRT) and iteratively using a variational method. Harmonic force constants for ZB and RS systems were calculated on $8 \times 8 \times 8$ ($9 \times 9 \times 6$ for WZ and NiAs) q-grid. Anharmonic force constants for ZB and RS were computed on a $4 \times 4 \times 4$ ($3 \times 3 \times 2$ for WZ and NiAs) q point grid using D3Q⁸⁹⁻⁹¹ package within QUANTUM-ESPRESSO. Acoustic sum rules were imposed on both harmonic and anharmonic interatomic force constants. Phonon linewidth and lattice thermal conductivity were calculated using ‘thermal2’ package within QUANTUM ESPRESSO. For these calculations, $30 \times 30 \times 30$ (for ZB and RS) and $30 \times 30 \times 20$ (for WZ and NiAs) q -mesh was used and iterations in the exact solution of the PBTE were performed until Δk between consecutive iterations diminished to below $1.0e^{-5}$. k values were converged after 5 iterations. Casimir scattering¹⁴⁵ is imposed to include the effect of boundary scattering for computing length dependent thermal conductivity in the nanoscales. Elastic constants were computed using ‘thermo_pw’ package in QUANTUM-ESPRESSO; Voigt-Reuss-Hill approximation¹⁴⁴ was used to calculate Bulk modulus, Shear modulus(G), Young’s Modulus(E) and Poisson’s ratio(ν).

12.2 RESULTS

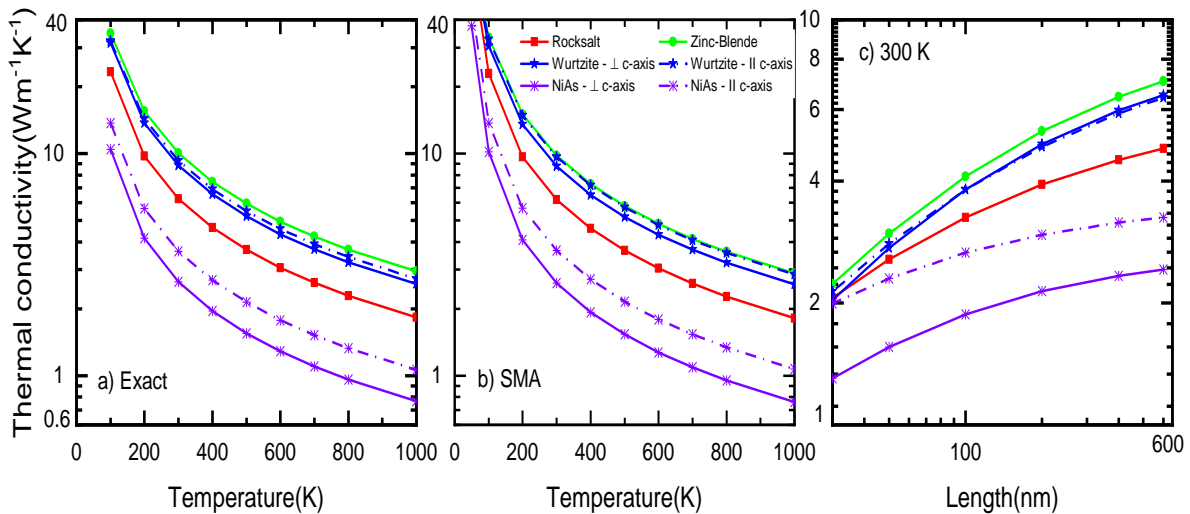


Figure 12.3 a) Temperature dependent lattice thermal conductivity by solving the PBTE iteratively b) at single mode relaxation time approximation (SMA) c) Length dependence thermal conductivity at room temperature (300 K) for MgTe with different crystalline phase.

12.2.1 Phonon dispersion and Lattice Constants

Phonon dispersion and phonon density of states for the four crystalline phases of MgTe is shown in Fig 12.1 which are in good agreement with previous work²⁰⁴. Structural parameters such as Young's modulus(E), Bulk modulus(B), Shear modulus(G) and Poisson's ratio computed based on Voigt-Ruess-Hill approximation are listed in Table 12.1 which are also in excellent agreement with the previously published work^{204, 205} for all the four crystalline phases of MgTe.

Table 12.3: Lattice constants, Bulk modulus(B), Youngs modulus(E), Shear modulus(G) and poisson's(ν) ratio of MgTe with different crystal phase.

S. No	Crystal phase	a (bohr)	c/a	B (GPa)	E(GPa)	G(GPa)	ν
1.	Nickel arsenic (NiAs)	7.8585	1.6281	52.82	63.97	24.64	0.2981
2.	Wurtzite (WZ)	8.5287	1.6286	38.97	44.92	17.18	0.3076
3.	Rocksalt (RS)	11.0985		52.7	86.12	35.07	0.2276
4.	Zincblende (ZB)	12.073		38.39	37.1	13.88	0.3367

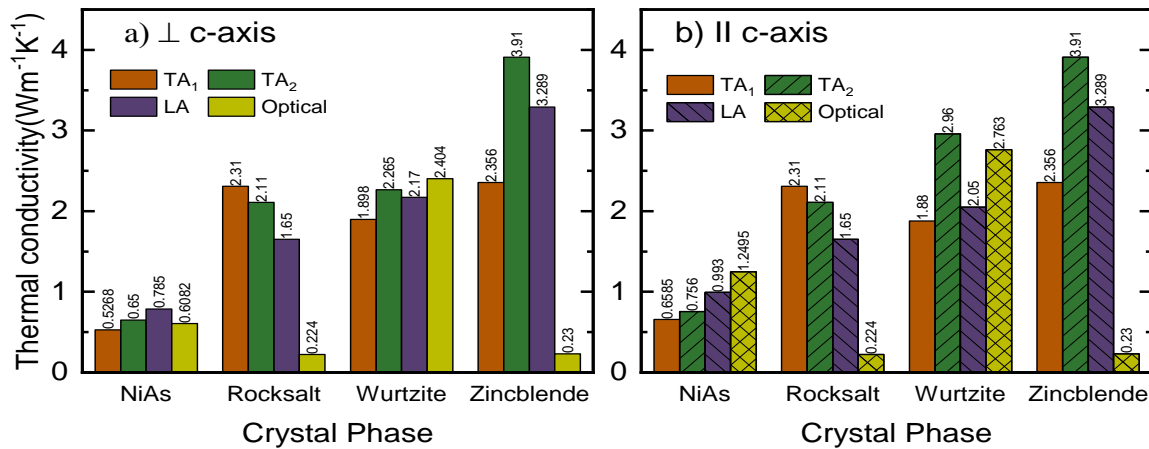


Figure 12.4: Thermal conductivity contribution from TA₁, TA₂, LA and optical phonon modes of MgTe with different crystalline phase along different directions.

12.2.2 Lattice Thermal Conductivity

Lattice thermal conductivity(k) calculated by solving the phonon Boltzmann transport equation (PBTE) is shown in Fig 12.3. Fig 12.3a and b represents the temperature dependent lattice thermal conductivity of MgTe with different crystalline phase by solving the PBTE iteratively and at SMA. SMA results are just 5% less than that of the iterative solutions. At 300 K, full iterated thermal conductivity(k) of MgTe is as follows: $k_{NiAs}(2.645 \text{ Wm}^{-1}\text{K}^{-1}) < k_{RS}(6.26 \text{ Wm}^{-1}\text{K}^{-1}) < k_{WZ}(8.83 \text{ Wm}^{-1}\text{K}^{-1})$

$^1\text{K}^{-1}) < k_{\text{ZB}} (10.05 \text{ Wm}^{-1}\text{K}^{-1})$. These low thermal conductivity of less than $\sim 10 \text{ Wm}^{-1}\text{K}^{-1}$ shows the promising nature of MgTe in thermoelectric applications. k of $10.05 \text{ Wm}^{-1}\text{K}^{-1}$ for the zincblende phase MgTe is 3.8 times of the k of NiAs phase. This is due to the large phonon bandgap ($\sim 100 \text{ cm}^{-1}$) which eliminates the phonon scattering rates. Whereas ultra-low thermal conductivity of $2.645 \text{ Wm}^{-1}\text{K}^{-1}$ for the NiAs phase is due to the

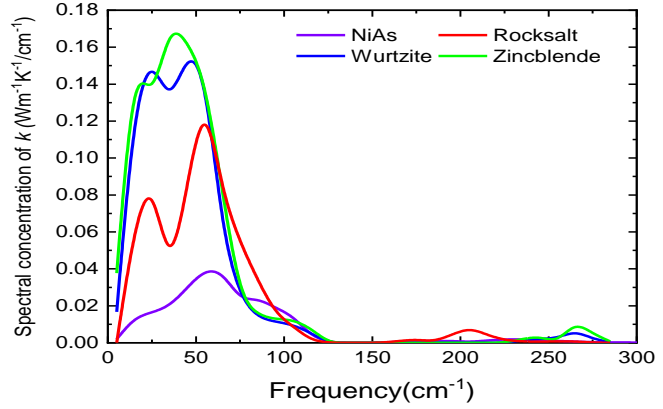


Figure 12.5: Spectral distributions of thermal conductivity in MgTe with different crystalline phase.

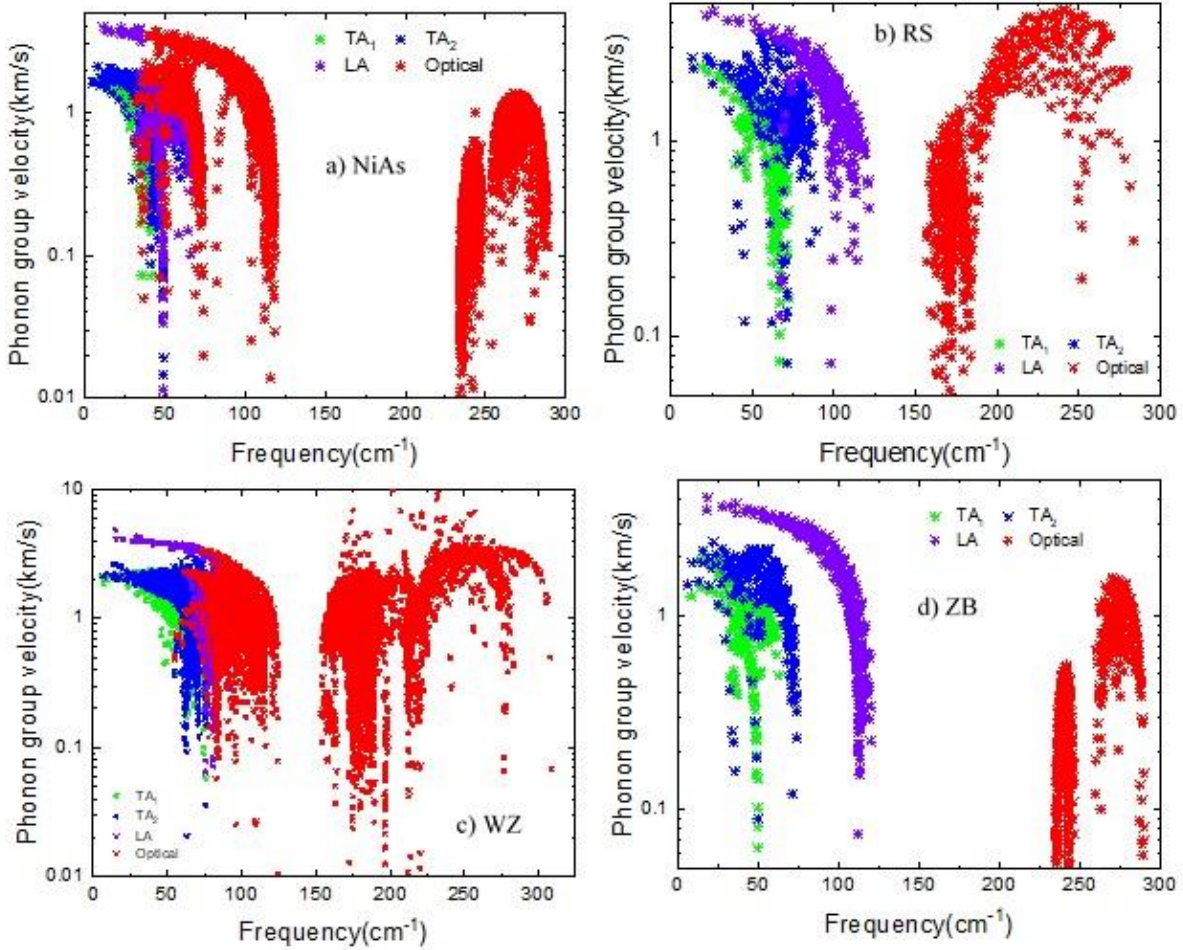


Figure 12.6: Phonon group velocity of MgTe with crystalline phase a) nickel arsenic (NiAs) b) rocksalt (RS) c) wurtzite (WZ) d) zinblende (ZB) at 300K

acoustic phonons are scattered by low frequency optical phonons because of the less phonon bandgap ($\sim 25 \text{ cm}^{-1}$). To explain this, we have analyzed the mode contributions thermal conductivity of transverse acoustic (TA_1 , TA_2), longitudinal acoustic (LA) and optical phonon modes, phonon group velocities, phonon linewidths (scattering rates) and its spectral distribution.

Figure 12.4 represents the thermal conductivity contribution from each phonon mode along \perp and \parallel to the c-axis (For cubic MgTe k along \perp - c-axis and \parallel - c-axis are same) at single-mode relaxation time approximation. For the cubic systems, optical phonon contributions are less than $\sim 3.5 \%$. Whereas optical phonons has a major contributions in both wurtzite and NiAs crystal phase due to the low frequency optical phonons. For an example, $1.245 \text{ Wm}^{-1}\text{K}^{-1}$ along the c-axis for with NiAs phase is 34.2% to its overall thermal conductivity and is higher than both TA and LA phonon modes. Likewise, $2.404 \text{ Wm}^{-1}\text{K}^{-1}$ along \perp -c-axis is 27.5 % to its overall thermal

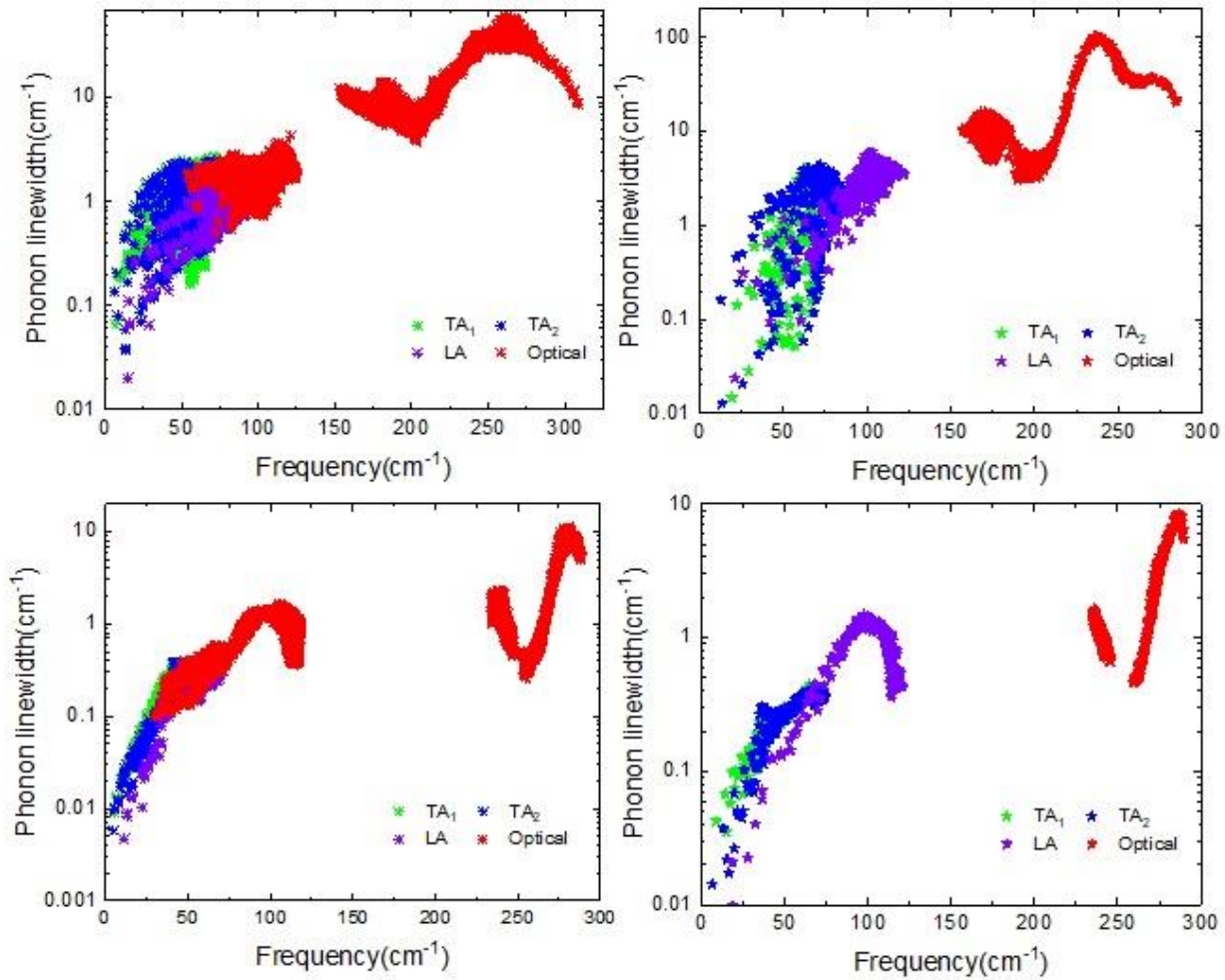


Figure 12.7: Phonon linewidth of MgTe with crystalline phase a) nickel arsenic (NiAs) b) rocksalt (RS) b) wurtzite (WZ) d) zincblende (ZB) at 300K

conductivity in wurtzite MgTe. To understand this, we plotted a spectral distribution of thermal conductivity over the entire frequency (Fig. 12.5) and we can observe that, low frequency optical phonons has significant contributions to its overall thermal conductivity. Whereas in cubic (NiAs and ZB) MgTe, TA modes between 25 - 75 cm^{-1} has a major contribution to its overall thermal conductivity. To illustrate this further, we have plotted the phonon group velocities and

Fig 12.6 a-d represents the phonon group velocities of MgTe with different crystalline phase. We can observe that, low frequency optical phonons (less than 130 cm^{-1}) has a considerable phonon group velocities to that of the acoustic phonons in NiAs and wurtzite phase. Fig 12.7 a-d shows the phonon linewidth for MgTe with different crystalline phase. In cubic systems, zincblende has the lowest phonon linewidth (less than 2 cm^{-1}) for acoustic modes due to large phonon bandgap and has the highest thermal conductivity ($\sim 10 \text{ Wm}^{-1}\text{K}^{-1}$) whereas TA phonons in rocksalt has one order of magnitude higher scattering rate than of the zincblende and has low thermal conductivity. Likewise, TA and LA phonons in NiAs has 8 times scattering rate than its counterpart wurtzite structure. Optical phonons in NiAs has considerable phonon lifetime (inverse of scattering rate) and hence has a significant contribution to its overall thermal conductivity.

For the nanostructures, length dependent thermal conductivity of MgTe between 30 nm and 1000 nm is computed by introducing the boundary/Casimir scattering and is shown in Fig 12.3c. At 300K and at 100 nm, zincblende has a maximum thermal conductivity of $\sim 4 \text{ Wm}^{-1}\text{K}^{-1}$ shows the promising nature of MgTe for the thermoelectric applications.

12.3 CONCLUSION

Thermal conductivity of magnesium telluride (MgTe) with four crystalline phases; zincblende, rocksalt, wurtzite and nickel arsenic were computed by first principles calculations with phonon Boltzmann transport equations. Our first principles calculations shows a low thermal conductivity of less than $\sim 10 \text{ Wm}^{-1}\text{K}^{-1}$ for all the crystalline phase of MgTe. We systematically investigated the phonon group velocity, phonon scattering rate and mode dependent thermal conductivity of MgTe. Our first principles calculations shows that, NiAs and wurtzite has significant contributions from optical phonons than ZB and rocksalt. At nanometer length scales such as 50 nm for NiAs phase, thermal conductivity of less than $1.4 \text{ Wm}^{-1}\text{K}^{-1}$ shows a promising nature of MgTe for thermoelectric applications.

CHAPTER 13- EQUI-BIAXIAL STRAIN TUNED HIGH THERMAL CONDUCTIVITY IN MONOLAYER GERMANIUM CARBIDE(2D-GeC) - A FIRST PRINCIPLES STUDY

Ever since the invention of monolayer graphene with ultra-high thermal conductivity, two dimensional materials with high thermal conductivity have attracted great attention for thermal management in micro/nano electronics. Cubic germanium carbide is known to have an ultrahigh thermal conductivity of $1750 \text{ Wm}^{-1}\text{K}^{-1}$, however, thermal conductivity of monolayer germanium carbide (2D-GeC) is unknown. In this work, we report a high thermal conductivity of $125 \text{ Wm}^{-1}\text{K}^{-1}$ for the unstrained 2D-GeC. To fine tune the thermal conductivity, we also study the effect of strain engineering as it shows a promising trend to achieve higher thermal conductivity. Our first principles calculations report 725% enhancement in lattice thermal conductivity (k) in monolayer germanium carbide (2D-GeC) through 6% equi-biaxial tensile strain. At room temperature, k of $125 \text{ Wm}^{-1}\text{K}^{-1}$ for the unstrained monolayer germanium carbide(2D-GeC) increased to $906 \text{ Wm}^{-1}\text{K}^{-1}$ through 6% equi-biaxial tensile strain. We analyzed the mode contribution from out-of-plane acoustic (ZA), in-plane acoustic (TA and LA) and optical phonons (ZO, TO and LO) with strain. First principles calculations reveal that, k monotonically increases with strain upto 6% and dropping down at higher strain rate (>6%). The underlying mechanism is explained with interplay between the vibrational frequency and the phonon lifetime. We also report the thermal conductivity enhancement at nanometer length scales. At 50 nm and at room temperature, thermal conductivity of $30 \text{ Wm}^{-1}\text{K}^{-1}$ for unstrained 2D-GeC increased to $100 \text{ Wm}^{-1}\text{K}^{-1}$ with 6% equi-biaxial tensile strain. This high thermal conductivity of $100 \text{ Wm}^{-1}\text{K}^{-1}$ for the strained 2D-GeC at nanometer length scales ($L=50 \text{ nm}$) shows that, strained 2D-GeC will be a promising material for thermal management applications.

Thermal management in modern electronic devices is a critical issue in integrating millions of transistors into a single chip due to its hot spots^{3, 232, 233, 241}. Hence, materials with high thermal conductivity have attracted remarkable attraction for efficient heat dissipation to improve the system reliability. Ever since the monolayer graphene was reported as an ultra-high thermal conductivity of $3000\text{-}5000 \text{ Wm}^{-1}\text{K}^{-1}$,^{180, 242-244} tremendous work has been invested in exploring other two-dimensional materials such as $h\text{-BN}$ ^{245, 246}, $h\text{-BP}$ ²⁴⁷, $h\text{-BAs}$ ^{78, 247}, $h\text{-GaN}$ ²⁴⁸, $h\text{-AlN}$ ²⁴⁹, $h\text{-SiC}$ ²⁵⁰ (where B,N, P, As, Ga, Al, Si,C represents boron, nitrogen, phosphorous, arsenic, gallium, aluminum, silicon and carbon respectively) etc.,

Cubic Germanium Carbide (c-GeC) has an ultra-high thermal conductivity of $1517 \text{ Wm}^{-1}\text{K}^{-1}$.¹³⁹ Nevertheless, k of monolayer Germanium Carbide is unknown. In this work, we report a high thermal conductivity of $125 \text{ Wm}^{-1}\text{K}^{-1}$ for the unstrained 2D-GeC. This high thermal conductivity is mainly due to the high phonon frequency and velocity as well as large phonon bandgap. To fine tune the thermal conductivity, we also introduce strain engineering as it shows a promising trend to achieve higher thermal conductivity. Our first principles calculations show a maximum of 725% enhancement in lattice thermal conductivity(k) at room temperature in monolayer germanium carbide(2D-GeC) through 6% equi-biaxial tensile strain and started dropping down due to the interplay between phonon scattering rate and phonon velocity. At room temperature, k of $125 \text{ Wm}^{-1}\text{K}^{-1}$ for the unstrained monolayer germanium carbide(2D-GeC) increased to $906 \text{ Wm}^{-1}\text{K}^{-1}$ through 6% equi-biaxial tensile strain and started dropping down beyond that. To understand the interplay between the phonon group velocity and phonon scattering rate, we keep the velocity term constant and studied the change in k due to the scattering rate. Increase in phonon group velocity is explained with elastic constants and increase in scattering rate beyond 6% strain is analyzed with phonon band gap.

13.1 COMPUTATIONAL

METHODS: First principles computations were performed using local density approximations¹⁸⁷ with norm-conserving pseudopotentials using QUANTUM ESPRESSO⁸⁸ package. The geometry of the monolayer GeC with 2 atoms unit cell is optimized until the forces on all atoms are less than $10^{-5} \text{ eV \AA}^{-1}$ and the energy difference is converged to 10^{-15} Ry . We maintained a vacuum of 20 \AA to avoid the interaction between the neighboring layers. A plane-wave cutoff energy of 120 Ry was used. Monkhorst-Pack¹¹⁵ k -point mesh of $24 \times 24 \times 1$ is used during the variable cell optimization. Optimized monolayer GeC structure is shown in Fig. 13.1;

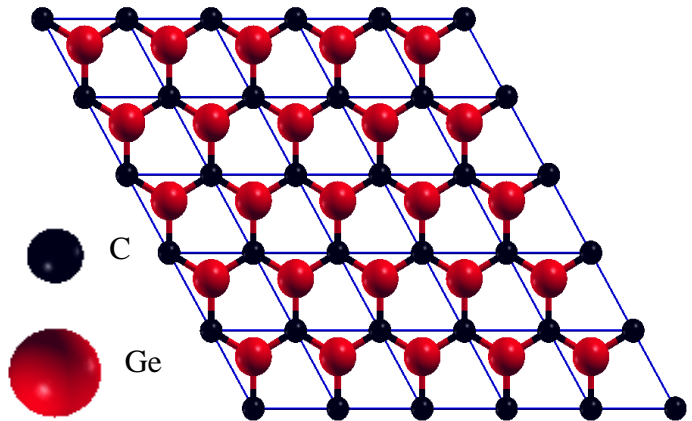


Figure 13.1: Atomic configuration of monolayer germanium carbide. Black and red color represents the Carbon and Germanium respectively.

obtained lattice constants of $a=3.192 \text{ \AA}$ and are in good agreement with the previous first principles calculations. The relaxed structure is equibiaxially strained along x and y direction by changing the lattice constants. Elastic constants were computed using QUANTUM ESPRESSO thermo_pw package. Dynamical matrix and harmonic force constants were calculated using $24 \times 24 \times 1$ q-grid. $8 \times 8 \times 1$ q-points were used to compute the anharmonic force constants using QUANTUM ESPRESSO D3Q⁸⁹⁻⁹¹ package. Acoustic sum rules were imposed on both harmonic and anharmonic interatomic force constants. Phonon linewidth and lattice thermal conductivity were calculated iteratively using QUANTUM ESPRESSO thermal2 code with $140 \times 140 \times 1$ q-mesh and 0.1 cm^{-1} smearing until the Δk values are converged to $1.0e^{-5}$.

13.2 RESULTS

13.2.1 Phonon dispersion and density of states: Phonon dispersion along the high symmetry points and phonon density for the monolayer germanium carbide(2D-GeC) with equibiaxial strain upto 8% is shown in Fig 13.2. The results showing positive frequencies indicating the system is

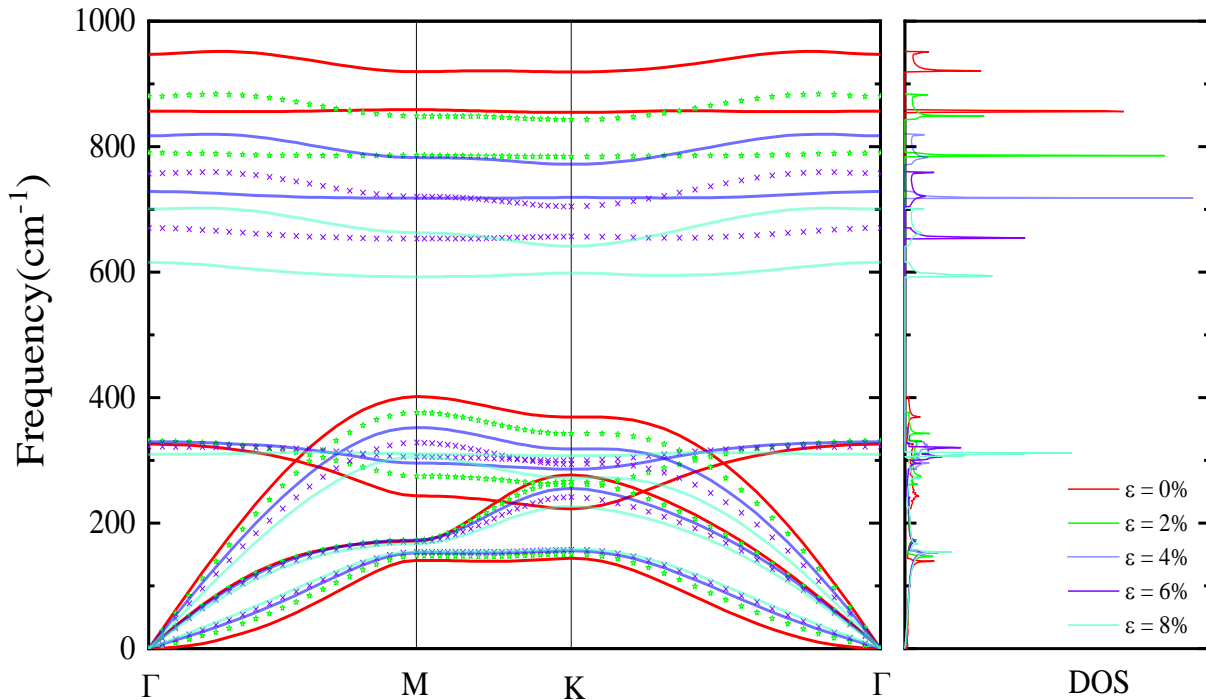


Figure 13.2: Phonon dispersion and phonon density of states for the monolayer germanium carbide with strain between 0% and 8%

dynamically stable under equi-biaxial tensile strain. We can also observe a quadratic ZA phonon

branch²⁵¹ and linear TA and LA phonons near Γ point which are commonly observed in 2D materials. We can observe that, out-of-plane vibration mode (ZA) is increasing with strain and is observed in other monolayer materials as well^{252, 253}. The high acoustic frequency of upto ~ 400 cm^{-1} is mainly due to the strong bonding between the germanium and carbon atoms and light atomic mass. It is also clearly seen that, there is a bandgap between acoustic and optical phonon branches and are known as phonon bandgap (457.26 cm^{-1} for the unstrained 2D-GeC) which is mainly due to the mass difference between the atoms^{254, 255}.

Young's modulus(E) and Shear modulus(G) for a 2D system can be calculated²⁵⁶ from their elastic constants using $E^{2D} = (C_{11}^2 - C_{12}^2)/C_{11}$ and $G^{2D} = C_{66} = (C_{11} - C_{12})/2$. Elastic constants, Young's modulus (E) and shear modulus(G) for monolayer germanium carbide with equi-biaxial tensile strain are shown in table 1 and Fig 3 and are in good agreement²⁵⁷ with the unstrained 2D-GeC.

Table 13.1: Elastic constants, Young's modulus, Shear modulus and phonon bandgap with equibiaxial tensile strain for 2D-GeC

Strain	C_{11} (GPa)	C_{12} (GPa)	C_{66} (GPa)	Young's Modulus (GPa)	Shear Modulus (GPa)	Phonon bandgap (cm^{-1})
0	485.78	154.00	165.71	436.95	165.71	457.26
2	494.07	155.88	169.01	444.89	169.01	409.66
4	483.44	138.64	173.56	443.89	173.56	368.50
6	421.72	78.977	171.37	406.93	171.37	324.913
8	357.47	37.7	159.88	353.494	159.88	286.699

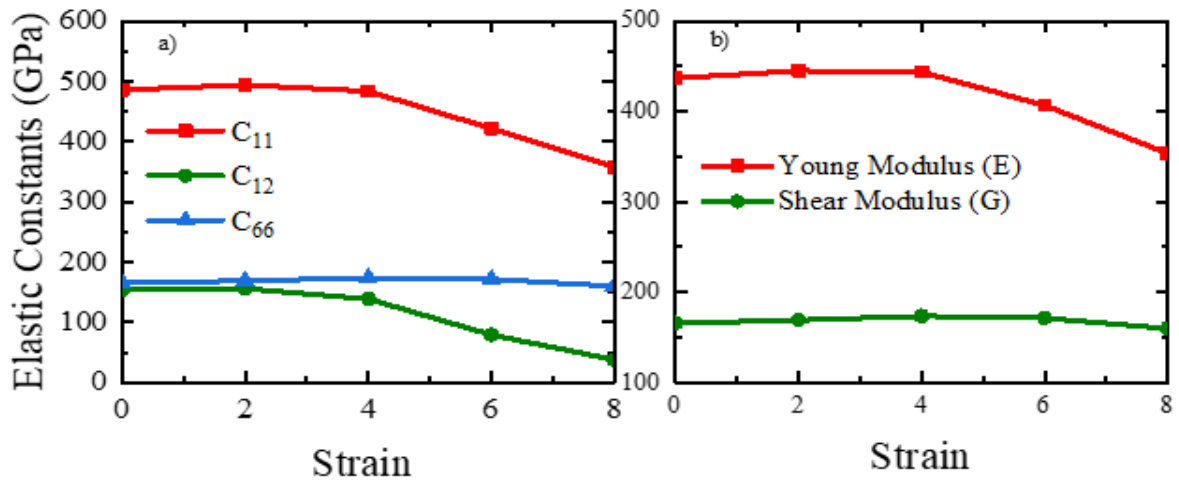


Figure 13.3: Elastic constants of monolayer germanium carbide with strain

13.2.2 Lattice thermal conductivity: Temperature dependent lattice thermal conductivity along arm-chair (k_{xx}) and zig-zag(k_{yy}) direction is shown in Fig 13.4 a and b. At room temperature ($T=300$ K), 2D-GeC has a high thermal conductivity of $127.79 \text{ Wm}^{-1}\text{K}^{-1}$ ($59.65 \text{ Wm}^{-1}\text{K}^{-1}$) and

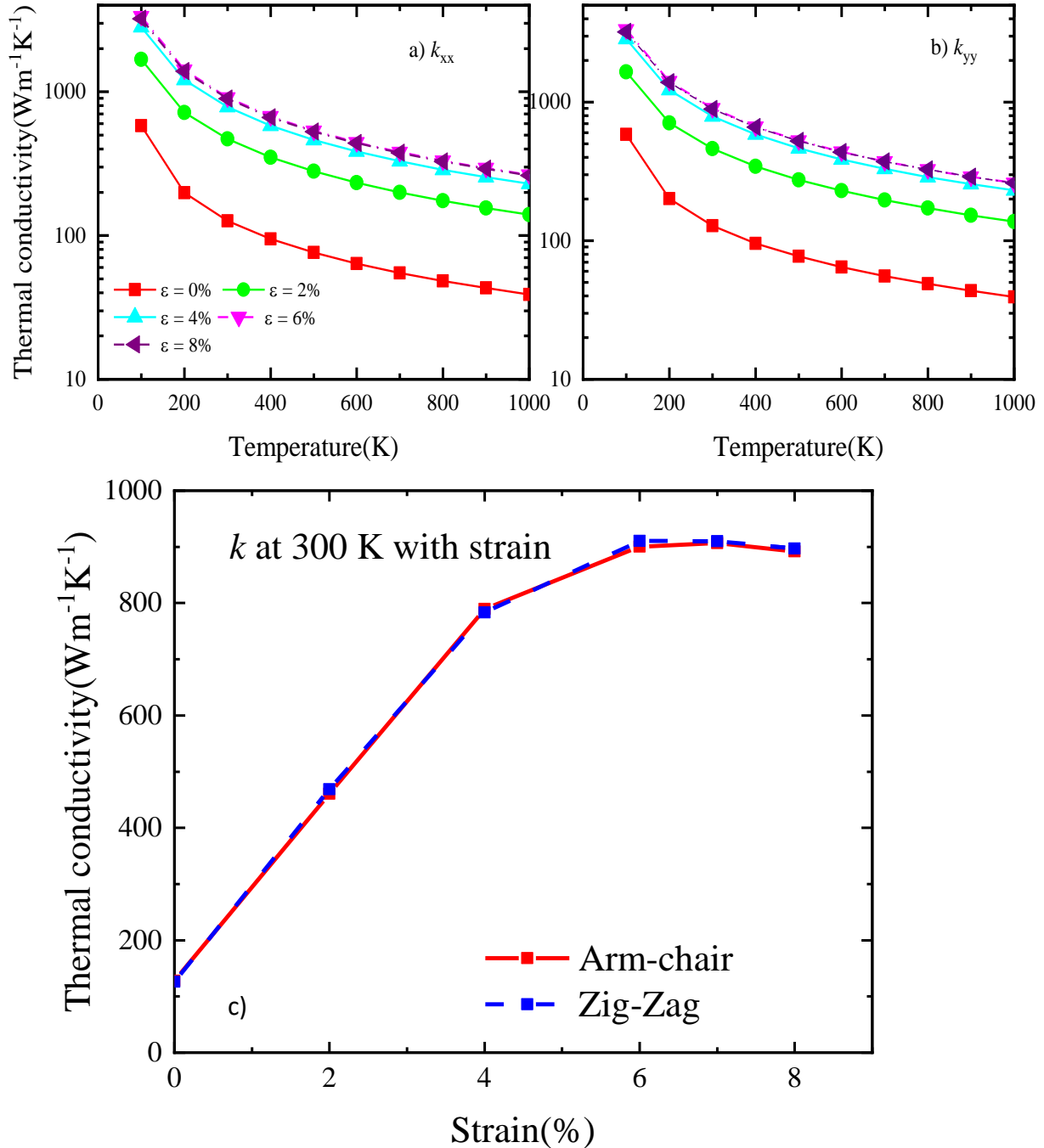


Figure 13.4a and b) Temperature dependent lattice thermal conductivity along arm-chair and zig-zag direction with strain for a pure monolayer germanium carbide(2D-GeC) c) Lattice thermal conductivity of monolayer germanium carbide with strain at 300 K.

126.23 $\text{Wm}^{-1}\text{K}^{-1}$ (58.47 $\text{Wm}^{-1}\text{K}^{-1}$) along arm-chair and zig-zag direction respectively for the

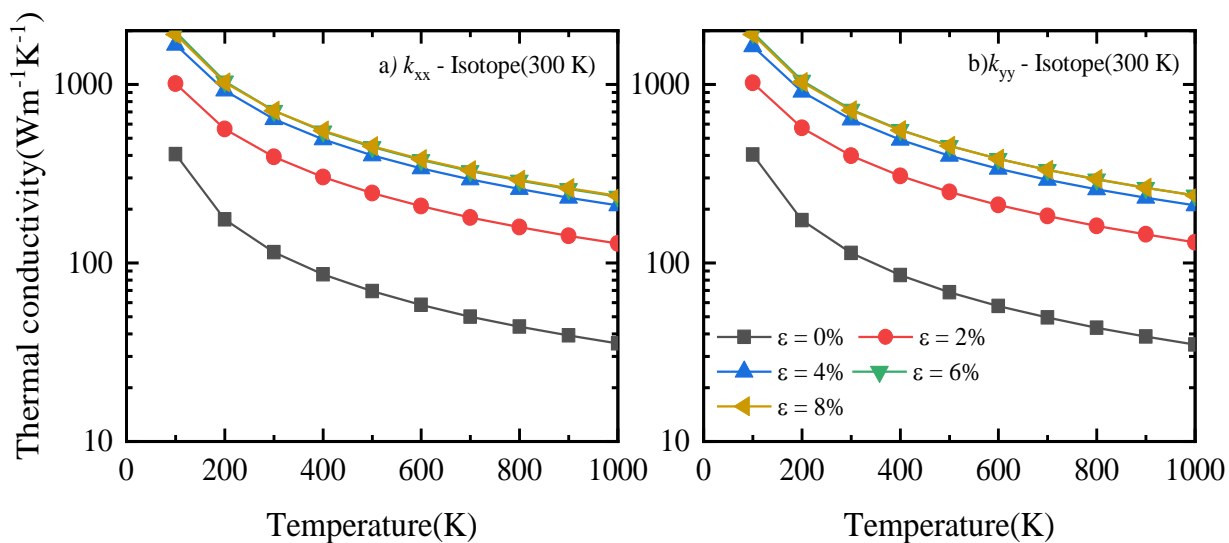


Figure 13.5: Lattice thermal conductivity of monolayer germanium carbide(2D-GeC) with isotopic scattering for strains between 0% and 8%.

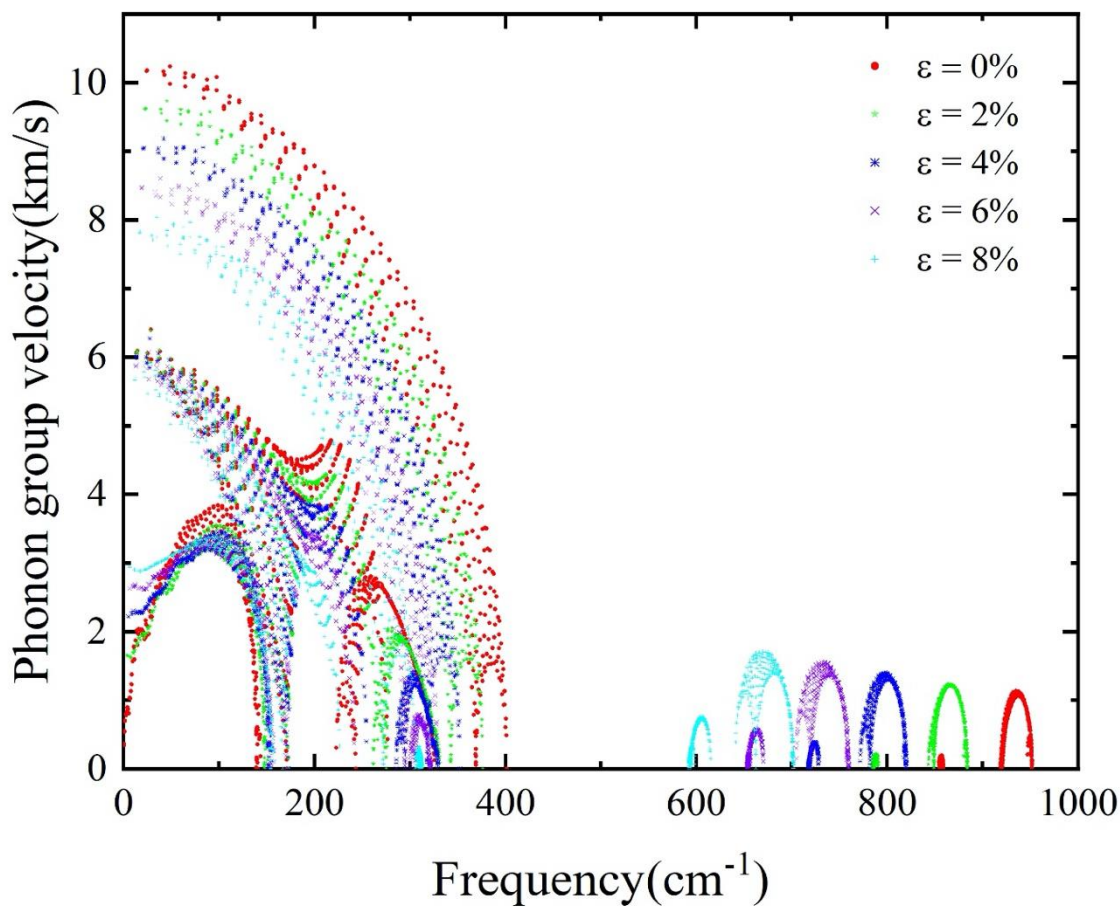


Figure 13.6: Phonon group velocity of monolayer germanium carbide with strain

iterative(SMA) solution of the Boltzmann transport equation. With isotope scattering, $115 \text{ Wm}^{-1}\text{K}^{-1}$ and $113.64 \text{ Wm}^{-1}\text{K}^{-1}$ indicates that, Isotope scattering has a minimal effect ($\sim 10\%$) on its over thermal conductivity as shown in Fig 13.5.

Room temperature lattice thermal conductivity of 2D-GeC with equibiaxial strain is shown in Fig 13.4c. It is clearly seen that, k is increasing with strain upto 6% and starts decreasing beyond that. With 6% equi-biaxial strain, k value of $900 \text{ Wm}^{-1}\text{K}^{-1}$ ($910.84 \text{ Wm}^{-1}\text{K}^{-1}$) is $\sim 708\%$ higher than that of unstrained 2D-GeC k of $127.79 \text{ Wm}^{-1}\text{K}^{-1}$ ($126.23 \text{ Wm}^{-1}\text{K}^{-1}$) along the armn-chair(zig-zag) direction. This increase in k is analyzed with phonon group velocity, phonon scattering rate (inverse of lifetime), phonon bandgap and elastic constants.

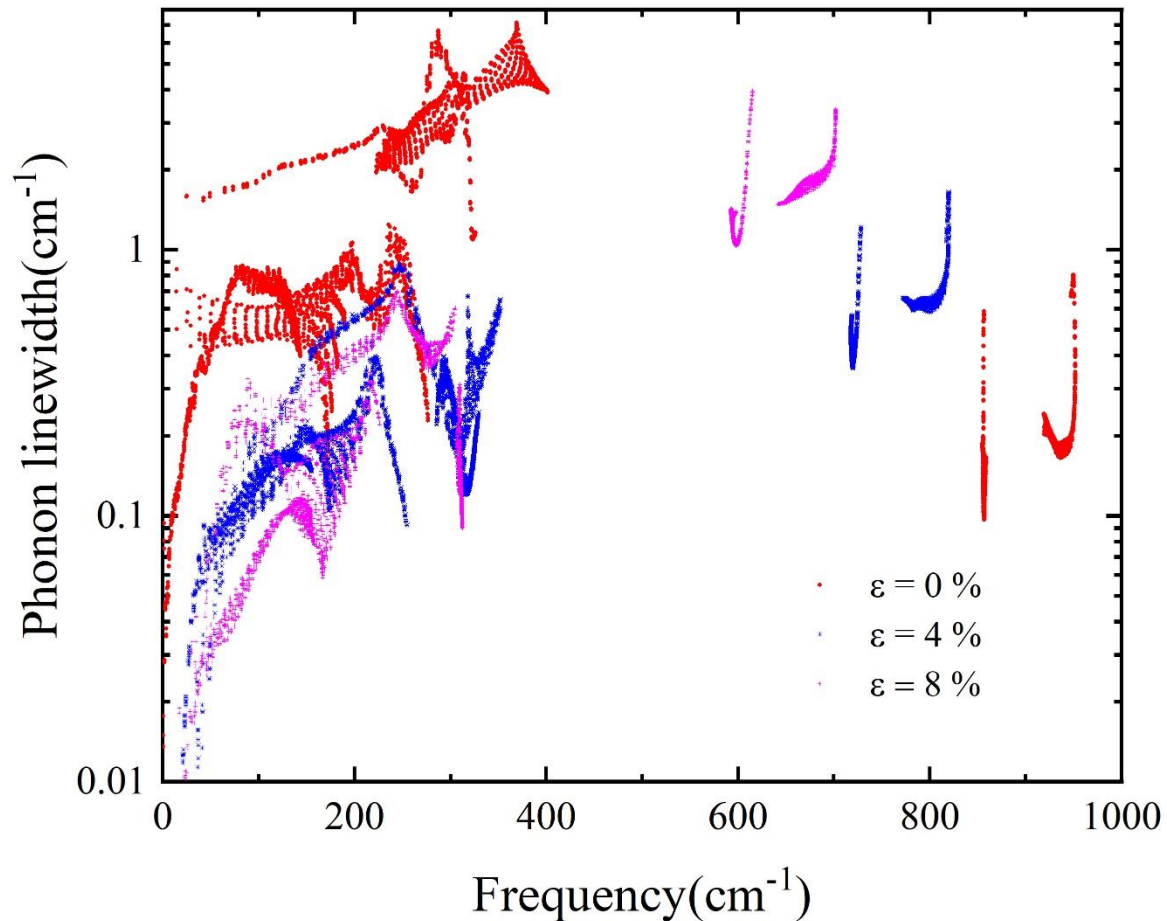


Figure 13.7: Phonon linewidth of monolayer germanium carbide with strain

Fig 13.6 and 13.7 shows the phonon group velocity and phonon linewidth of 2D-GeC with strain. From Fig 6, We can clearly see that, phonon group velocity of ZA mode increases with strain. This is due to the stiffening of ZA mode with strain. Whereas, phonon group velocity of TA

and LA mode decreases and is due to the softening of TA and LA modes with strain. After 6%, k value decreases, due to a reduction in phonon bandgap as shown in Fig 8 which allows for an increase in scattering of acoustic branches through absorption processes.

13.3 CONCLUSION: By solving Phonon Boltzmann Transport equation within the density functional theory, we

report a high thermal conductivity (k) of $\sim 127 \text{ Wm}^{-1}\text{K}^{-1}$ ($126 \text{ Wm}^{-1}\text{K}^{-1}$) for the monolayer germanium carbide (2d-GeC) along the arm-chair and zig-zag direction. With 6% equi-biaxial strain, k reaches a peak of $\sim 900 \text{ Wm}^{-1}\text{K}^{-1}$ and starts decreasing due to a reduction in phonon bandgap. This increase in thermal conductivity is mainly attributed to an increase in phonon group velocity of ZA phonons due to stiffening of ZA modes. This study provides an avenue for modulating the k of a 2D materials for thermal management applications.

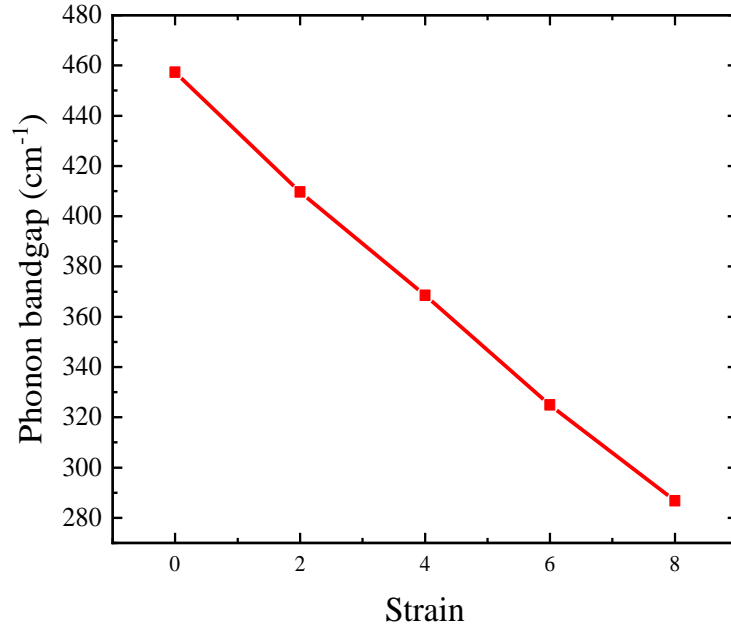


Figure 13.8: Phonon bandgap for a monolayer germanium carbide with strain

REFERENCES

1. Cahill, D. G.; Braun, P. V.; Chen, G.; Clarke, D. R.; Fan, S.; Goodson, K. E.; Keblinski, P.; King, W. P.; Mahan, G. D.; Majumdar, A.; Maris, H. J.; Phillpot, S. R.; Pop, E.; Shi, L., Nanoscale thermal transport. II. 2003–2012. *Applied Physics Reviews* **2014**, *1* (1), 011305.
2. Sobhan, C. B.; Peterson, G. P., *Microscale and nanoscale heat transfer: fundamentals and engineering applications*. CRC Press: 2008.
3. Moore, A. L.; Shi, L., Emerging challenges and materials for thermal management of electronics. *Materials Today* **2014**, *17* (4), 163-174.
4. Mallik, S.; Ekere, N.; Best, C.; Bhatti, R., Investigation of thermal management materials for automotive electronic control units. *Applied Thermal Engineering* **2011**, *31* (2), 355-362.
5. Lee, J.-K.; Lee, Y.-J.; Chae, W.-S.; Sung, Y.-M., Enhanced ionic conductivity in PEO-LiClO₄ hybrid electrolytes by structural modification. *Journal of Electroceramics* **2006**, *17* (2), 941-944.
6. Lu, X.; Xu, G., Thermally conductive polymer composites for electronic packaging. *Journal of Applied Polymer Science* **1997**, *65* (13), 2733-2738.
7. Huynh, W. U.; Dittmer, J. J.; Alivisatos, A. P., Hybrid Nanorod-Polymer Solar Cells. *Science* **2002**, *295* (5564), 2425-2427.
8. Liu, W.; Davidson, J.; Mantell, S., Thermal Analysis of Polymer Heat Exchangers for Solar Water Heating: A Case Study. *Journal of Solar Energy Engineering* **2000**, *122* (2), 84-91.
9. Dreiser, C.; Bart, H.-J., Mineral scale control in polymer film heat exchangers. *Applied Thermal Engineering* **2014**, *65* (1), 524-529.
10. Bassett, D., Ciliation and lamellae in crystalline polymers. *Macromolecular Symposia* **1997**, *114* (1), 121-126.
11. Yoshihara, S.; Ezaki, T.; Nakamura, M.; Watanabe, J.; Matsumoto, K., Enhanced Thermal Conductivity of Thermoplastics by Lamellar Crystal Alignment of Polymer Matrices. *Macromolecular Chemistry and Physics* **2012**, *213* (21), 2213-2219.
12. Gelpí, J.; Hospital, A.; Goñi, R.; Orozco, M., *Molecular dynamics simulations: Advances and applications*. 2015; Vol. 10, p 37.
13. Martínez, L.; Andrade, R.; Birgin, E. G.; Martínez, J. M., PACKMOL: A package for building initial configurations for molecular dynamics simulations. *Journal of Computational Chemistry* **2009**, *30* (13), 2157-2164.
14. Plimpton, S., Fast Parallel Algorithms for Short-Range Molecular Dynamics. *Journal of Computational Physics* **1995**, *117* (1), 1-19.
15. Sun, H., COMPASS: An ab Initio Force-Field Optimized for Condensed-Phase Applications Overview with Details on Alkane and Benzene Compounds. *The Journal of Physical Chemistry B* **1998**, *102* (38), 7338-7364.
16. Müller-Plathe, F., A simple nonequilibrium molecular dynamics method for calculating the thermal conductivity. *The Journal of Chemical Physics* **1997**, *106* (14), 6082-6085.
17. Muthaiah, R.; Garg, J., Temperature effects in the thermal conductivity of aligned amorphous polyethylene—A molecular dynamics study. *Journal of Applied Physics* **2018**, *124* (10), 105102.
18. Balandin, A. A., Thermal properties of graphene and nanostructured carbon materials. *Nature Materials* **2011**, *10*, 569.
19. Shangchao, L.; Markus, J. B., The effect of non-covalent functionalization on the thermal conductance of graphene/organic interfaces. *Nanotechnology* **2013**, *24* (16), 165702.
20. Wang, M.; Hu, N.; Zhou, L.; Yan, C., Enhanced interfacial thermal transport across graphene-polymer interfaces by grafting polymer chains. *Carbon* **2015**, *85*, 414-421.
21. Garg, J., Relative effect of edge versus basal plane functionalization on graphene/polymer interfacial thermal conductance - Role of in-plane phonons. *Applied Physics Letters* **2017**, *110* (9), 093112.

22. Mei, S.; Knezevic, I., Thermal conductivity of III-V semiconductor superlattices. *Journal of Applied Physics* **2015**, *118* (17), 175101.
23. Dreiser, C.; Kratz, L. J.; Bart, H.-J., Polymer Film Heat Exchanger for Seawater Desalination: Prevention and Cleaning of fouling deposits. In *International Conference on Heat exchanger fouling and cleaning*, M.R. Malayeri, H. M.-S. a. A. P. W., Ed. Budapest, Hungary, 2013; p 296.
24. Liu, W.; Davidson, J.; Mantell, S., Thermal analysis of polymer heat exchangers for solar water heating: A case study. *Journal of solar energy engineering* **2000**, *122*, 84.
25. Mallik, S.; Ekere, N.; Best, C.; Bhatti, R., Investigation of thermal management materials for automotive electronic control units. *Applied Thermal Engineering* **2011**, *31*, 355.
26. Lu, X.; Xu, G., Thermally Conductive Polymer Composites for Electronic Packaging. *Journal of Applied Polymer Science* **1997**, *65*, 2733.
27. Chen, X.; Su, Y.; Reay, D.; Riffat, S., Recent Research developments in polymer heat exchangers- A review. *Renewable and Sustainable Energy Reviews* **2016**, *60*, 1367.
28. Shen, S.; Henry, A.; Tong, J.; Zheng, R.; Chen, G., Polyethylene nanofibres with very high thermal conductivities *Nature Nanotechnology* **2010**, *5*, 251-255.
29. Saeidijavash, M.; Garg, J.; Grady, B.; Smith, B.; Li, Z.; Young, R. J.; Tarannum, F.; BelBekri, N., High thermal conductivity through simultaneously aligned polyethylene lamellae and graphene nanoplatelets. *Nanoscale* **2017**, *9*, 12867-12873.
30. Ghasemi, H.; Thoppey, N.; Huang, X.; Loomis, J.; Li, X.; Tong, J.; Wang, J.; Chen, G., High thermal conductivity Ultra-High Molecular Weight Polyethylene (UHMWPE) Films. In *14th IEEE ITherm Conference*, Orlando, FL, 2014.
31. Choy, C. L.; Chen, F. C.; Luk, W. H., Thermal conductivity of oriented crystalline polymers. *Journal of Polymer Science: Polymer Physics Edition* **1980**, *18*, 1187-1207.
32. Singh, V.; Bougher, T. L.; Weathers, A.; Cai, Y.; Bi, K.; Pettes, M. T.; McMenamin, S. A.; Lv, W.; Resler, D. P.; Gattuso, T. R.; Altman, D. H.; Sandhage, K. H.; Shi, L.; Henry, A.; Cola, B. A., High thermal conductivity of chain-oriented amorphous polythiophene. *Nature Nanotechnology* **2014**, *9*, 384.
33. Oilgshleger, C.; Schon, J. C., Simulation of thermal conductivity and heat transport in solids. *Phys. Rev. B* **1999**, *59*, 4125.
34. Schelling, P. K.; Phillpot, S. R.; Keblinski, P., Comparison of atomic-level simulation methods for computing thermal conductivity. *Phys. Rev. B* **2002**, *65*, 144306.
35. Zhang, T.; T.Luo, Role of chain morphology and stiffness in thermal conductivity of amorphous polymers. *The Journal of Physical Chemistry B* **2016**, *120*, 803-812.
36. Liu, J.; Yang, R., Tuning the thermal conductivity of polymers with mechanical strains. *Phys. Rev. B* **2010**, *81*, 174122.
37. Algaer, E. A.; Alaghemandi, M.; Bohm, M. C.; Muller-Plathe, F., Anisotropy of the Thermal Conductivity of stretched Amorphous Polystyrene in Supercritical Carbon Dioxide studied by reverse nonequilibrium molecular-dynamics simulations. *J. Phys. Chem. B* **2009**, *113*, 14596.
38. Muthaiah, R.; Garg, J. In *Effect of temperature on thermal conductivity of aligned amorphous polyethylene-Molecular Dynamics study*, APS March Meeting Abstracts, 2019; p F49. 013.
39. Hinze, M.; Ranfit, F.; Drummer, D.; Schweiger, W., Reduction of the heat capacity in low temperature adsorption chillers using thermally conductive polymers as heat-exchanger materials. *Energy management and conversion* **2017**, *145*, 378.
40. Patel, A. B.; Brisson, J. G., Design, construction and performance of plastic heat exchangers for sub-Kelvin use. *Cryogenics* **2000**, *40*, 91.
41. Plimpton, S., Fast parallel algorithms for short-range molecular dynamics *J. Comp. Phys.* **1995**, *117*, 1-9.
42. Sun, H., COMPASS: An ab Initio Force-Field Optimized for Condensed-Phase Applications - Overview with Details on Alkane and Benzene Compounds. *J. Phys. Chem B* **1998**, *102*, 7338.

43. Muller-Plathe, F., A simple non-equilibrium molecular dynamics method for calculating the thermal conductivity. *J. Chem. Phys.* **1997**, *106*, 6082-6085.
44. Srivastava, G. P., *Physics of Phonons*. Taylor and Francis Group: New York, NY 10016, 1990.
45. Hennig, J., Anisotropy and structure in uniaxially stretched amorphous high polymers. *Journal of polymer science: polymer symposia* **1967**, *16*, 2751-2761.
46. Eiermann, K., Thermal conductivity of high polymers. *Journal of polymer science: Part C* **1964**, *6*, 157-165.
47. Kreitmeier, S. N.; Liang, G. L.; Noid, D. W.; Sumpter, B. G., Thermal analysis via molecular dynamics simulation. *Journal of thermal analysis* **1996**, *46* (3), 853-869.
48. Santos, W. N. d.; Sousa, J. A. d.; Jr, R. G., Thermal conductivity behavior of polymers around glass transition and crystalline melting temperatures. *Polymer Testing* **2013**, *32*, 987-994.
49. Song, S. H.; Park, K. H.; Kim, B. H.; Choi, Y. W.; Jun, G. H.; Lee, D. J.; Kong, B. S.; Paik, K. W.; Jeon, S., Enhanced thermal conductivity of epoxy-graphene composites by using non-oxidized graphene flakes with non-covalent functionalization. *Adv Mater* **2013**, *25* (5), 732-7.
50. Shahil, K. M. F.; Balandin, A. A., Graphene–Multilayer Graphene Nanocomposites as Highly Efficient Thermal Interface Materials. *Nano Letters* **2012**, *12* (2), 861-867.
51. Winey, K. I.; Kashiwagi, T.; Mu, M., Improving Electrical Conductivity and Thermal Properties of Polymers by the Addition of Carbon Nanotubes as Fillers. *MRS Bulletin* **2007**, *32* (4), 348-353.
52. Su, Y.; Li, J. J.; Weng, G. J., Theory of thermal conductivity of graphene-polymer nanocomposites with interfacial Kapitza resistance and graphene-graphene contact resistance. *Carbon* **2018**, *137*, 222-233.
53. Qin, S.; Qin, D.; Ford, W. T.; Resasco, D. E.; Herrera, J. E., Functionalization of Single-Walled Carbon Nanotubes with Polystyrene via Grafting to and Grafting from Methods. *Macromolecules* **2004**, *37* (3), 752-757.
54. Lin, S.; Buehler, M. J., The effect of non-covalent functionalization on the thermal conductance of graphene/organic interfaces. *Nanotechnology* **2013**, *24* (16), 165702.
55. Konatham, D.; Striolo, A., Thermal boundary resistance at the graphene-oil interface. *Applied Physics Letters* **2009**, *95* (16), 163105.
56. Mungse, H. P.; Kumar, N.; Khatri, O. P., Synthesis, dispersion and lubrication potential of basal plane functionalized alkylated graphene nanosheets. *RSC advances* **2015**, *5* (32), 25565-25571.
57. Mungse, H. P.; Khatri, O. P., Chemically functionalized reduced graphene oxide as a novel material for reduction of friction and wear. *The Journal of Physical Chemistry C* **2014**, *118* (26), 14394-14402.
58. Rezvani Moghaddam, A.; Kamkar, M.; Ranjbar, Z.; Sundararaj, U.; Jannesari, A.; Ranjbar, B., Tuning the network structure of graphene/epoxy nanocomposites by controlling edge/basal localization of functional groups. *Industrial & Engineering Chemistry Research* **2019**, *58* (47), 21431-21440.
59. Xiang, Z.; Dai, Q.; Chen, J. F.; Dai, L., Edge functionalization of graphene and two-dimensional covalent organic polymers for energy conversion and storage. *Advanced Materials* **2016**, *28* (29), 6253-6261.
60. Yang, H.; Li, J.-S.; Zeng, X., Correlation between molecular structure and interfacial properties of edge or basal plane modified graphene oxide. *ACS Applied Nano Materials* **2018**, *1* (6), 2763-2773.
61. Wan, Y.-J.; Gong, L.-X.; Tang, L.-C.; Wu, L.-B.; Jiang, J.-X., Mechanical properties of epoxy composites filled with silane-functionalized graphene oxide. *Composites Part A: Applied Science and Manufacturing* **2014**, *64*, 79-89.
62. Martinez, L.; Andrade, R.; Birgin, E. G.; Martinez, J. M., PACKMOL: a package for building initial configurations for molecular dynamics simulations. *J Comput Chem* **2009**, *30* (13), 2157-64.
63. Humphrey, W.; Dalke, A.; Schulten, K., VMD: Visual molecular dynamics. *Journal of Molecular Graphics* **1996**, *14* (1), 33-38.
64. Ikeshoji, T.; Hafskjold, B., Non-equilibrium molecular dynamics calculation of heat conduction in liquid and through liquid-gas interface. *Molecular Physics* **1994**, *81* (2), 251-261.

65. Robbins, A. B.; Minnich, A. J., Crystalline polymers with exceptionally low thermal conductivity studied using molecular dynamics. *Applied Physics Letters* **2015**, *107* (20), 201908.
66. Shen, X.; Lin, X.; Jia, J.; Wang, Z.; Li, Z.; Kim, J.-K., Tunable thermal conductivities of graphene oxide by functionalization and tensile loading. *Carbon* **2014**, *80*, 235-245.
67. Gang, C., Nanoscale heat transfer and nanostructured thermoelectrics. *IEEE Transactions on Components and Packaging Technologies* **2006**, *29* (2), 238-246.
68. Chen, G.; Shakouri, A., Heat Transfer in Nanostructures for Solid-State Energy Conversion. *Journal of Heat Transfer* **2001**, *124* (2), 242-252.
69. Takenaka, T.; Takigawa, M.; Shohno, K., Hardness of Boron Monophosphide. *Japanese Journal of Applied Physics* **1976**, *15* (11), 2235-2236.
70. Kang, J. S.; Wu, H.; Hu, Y., Thermal Properties and Phonon Spectral Characterization of Synthetic Boron Phosphide for High Thermal Conductivity Applications. *Nano Letters* **2017**, *17* (12), 7507-7514.
71. Kumashiro, Y., Refractory semiconductor of boron phosphide. *Journal of Materials Research* **1990**, *5* (12), 2933-2947.
72. Manjanath, A.; Samanta, A.; Pandey, T.; Singh, A. K., Semiconductor to metal transition in bilayer phosphorene under normal compressive strain. *Nanotechnology* **2015**, *26* (7), 075701.
73. Meng, X.; Pandey, T.; Jeong, J.; Fu, S.; Yang, J.; Chen, K.; Singh, A.; He, F.; Xu, X.; Zhou, J.; Hsieh, W.-P.; Singh, A. K.; Lin, J.-F.; Wang, Y., Thermal Conductivity Enhancement in MoS_2 under Extreme Strain. *Physical Review Letters* **2019**, *122* (15), 155901.
74. Pesquera, D.; Herranz, G.; Barla, A.; Pellegrin, E.; Bondino, F.; Magnano, E.; Sánchez, F.; Fontcuberta, J., Surface symmetry-breaking and strain effects on orbital occupancy in transition metal perovskite epitaxial films. *Nature Communications* **2012**, *3* (1), 1189.
75. Xiao, P.; Fan, X.-L.; Liu, L.-M.; Lau, W.-M., Band gap engineering of FeS₂ under biaxial strain: a first principles study. *Physical Chemistry Chemical Physics* **2014**, *16* (44), 24466-24472.
76. Conley, H. J.; Wang, B.; Ziegler, J. I.; Haglund, R. F.; Pantelides, S. T.; Bolotin, K. I., Bandgap Engineering of Strained Monolayer and Bilayer MoS₂. *Nano Letters* **2013**, *13* (8), 3626-3630.
77. Saeidijavash, M.; Garg, J.; Grady, B.; Smith, B.; Li, Z.; Young, R. J.; Tarannum, F.; Bel Bekri, N., High thermal conductivity through simultaneously aligned polyethylene lamellae and graphene nanoplatelets. *Nanoscale* **2017**, *9* (35), 12867-12873.
78. Raeisi, M.; Ahmadi, S.; Rajabpour, A., Modulated thermal conductivity of 2D hexagonal boron arsenide: a strain engineering study. *Nanoscale* **2019**, *11* (45), 21799-21810.
79. Tang, D.-S.; Qin, G.-Z.; Hu, M.; Cao, B.-Y., Thermal transport properties of GaN with biaxial strain and electron-phonon coupling. *Journal of Applied Physics* **2020**, *127* (3), 035102.
80. Yang, Z.; Feng, R.; Su, F.; Hu, D.; Ma, X., Isotope and strain effects on thermal conductivity of silicon thin film. *Physica E: Low-dimensional Systems and Nanostructures* **2014**, *64*, 204-210.
81. Muthaiah, R.; Garg, J., Strain tuned high thermal conductivity in boron phosphide at nanometer length scales – a first-principles study. *Physical Chemistry Chemical Physics* **2020**.
82. Deinzer, G.; Birner, G.; Strauch, D., Ab initio calculation of the linewidth of various phonon modes in germanium and silicon. *Physical Review B* **2003**, *67* (14), 144304.
83. Lazzeri, M.; Piscanec, S.; Mauri, F.; Ferrari, A. C.; Robertson, J., Phonon linewidths and electron-phonon coupling in graphite and nanotubes. *Physical Review B* **2006**, *73* (15), 155426.
84. Li, W.; Carrete, J.; Mingo, N., Thermal conductivity and phonon linewidths of monolayer MoS₂ from first principles. *Applied Physics Letters* **2013**, *103* (25), 253103.
85. Garg, J.; Bonini, N.; Marzari, N., First-Principles Determination of Phonon Lifetimes, Mean Free Paths, and Thermal Conductivities in Crystalline Materials: Pure Silicon and Germanium. In *Length-Scale Dependent Phonon Interactions*, Shindé, S. L.; Srivastava, G. P., Eds. Springer New York: New York, NY, 2014; pp 115-136.

86. Broido, D. A.; Malorny, M.; Birner, G.; Mingo, N.; Stewart, D. A., Intrinsic lattice thermal conductivity of semiconductors from first principles. *Applied Physics Letters* **2007**, *91* (23), 231922.
87. Garg, J.; Bonini, N.; Kozinsky, B.; Marzari, N., Role of Disorder and Anharmonicity in the Thermal Conductivity of Silicon-Germanium Alloys: A First-Principles Study. *Physical Review Letters* **2011**, *106* (4), 045901.
88. Giannozzi, P.; Baroni, S.; Bonini, N.; Calandra, M.; Car, R.; Cavazzoni, C.; Ceresoli, D.; Chiarotti, G. L.; Cococcioni, M.; Dabo, I.; Dal Corso, A.; de Gironcoli, S.; Fabris, S.; Fratesi, G.; Gebauer, R.; Gerstmann, U.; Gougoussis, C.; Kokalj, A.; Lazzeri, M.; Martin-Samos, L.; Marzari, N.; Mauri, F.; Mazzarello, R.; Paolini, S.; Pasquarello, A.; Paulatto, L.; Sbraccia, C.; Scandolo, S.; Sclauzero, G.; Seitsonen, A. P.; Smogunov, A.; Umari, P.; Wentzcovitch, R. M., QUANTUM ESPRESSO: a modular and open-source software project for quantum simulations of materials. *Journal of Physics: Condensed Matter* **2009**, *21* (39), 395502.
89. Paulatto, L.; Errea, I.; Calandra, M.; Mauri, F., First-principles calculations of phonon frequencies, lifetimes, and spectral functions from weak to strong anharmonicity: The example of palladium hydrides. *Physical Review B* **2015**, *91* (5), 054304.
90. Paulatto, L.; Mauri, F.; Lazzeri, M., Anharmonic properties from a generalized third-order ab initio approach: Theory and applications to graphite and graphene. *Physical Review B* **2013**, *87* (21), 214303.
91. Fugallo, G.; Lazzeri, M.; Paulatto, L.; Mauri, F., Ab initio variational approach for evaluating lattice thermal conductivity. *Physical Review B* **2013**, *88* (4), 045430.
92. Setyawan, W.; Curtarolo, S., High-throughput electronic band structure calculations: Challenges and tools. *Computational Materials Science* **2010**, *49* (2), 299-312.
93. Alves, H. W. L.; Kunc, K., Lattice dynamics of boron phosphide. *Journal of Physics: Condensed Matter* **1992**, *4* (31), 6603-6612.
94. Tan, G.; Ohta, M.; Kanatzidis, M. G., Thermoelectric power generation: from new materials to devices. *Philosophical Transactions of the Royal Society A: Mathematical, Physical and Engineering Sciences* **2019**, *377* (2152), 20180450.
95. He, J.; Tritt, T. M., Advances in thermoelectric materials research: Looking back and moving forward. *Science* **2017**, *357* (6358), eaak9997.
96. Zhang, X.; Zhao, L.-D., Thermoelectric materials: Energy conversion between heat and electricity. *Journal of Materiomics* **2015**, *1* (2), 92-105.
97. Snyder, G. J.; Snyder, A. H., Figure of merit ZT of a thermoelectric device defined from materials properties. *Energy & Environmental Science* **2017**, *10* (11), 2280-2283.
98. Liu, W.; Tan, X.; Yin, K.; Liu, H.; Tang, X.; Shi, J.; Zhang, Q.; Uher, C., Convergence of Conduction Bands as a Means of Enhancing Thermoelectric Performance of $\text{Mg}_2\text{Si}_{1-x}\text{Sn}_x$ Solid Solutions. *Physical Review Letters* **2012**, *108* (16), 166601.
99. Pei, Y.; Shi, X.; LaLonde, A.; Wang, H.; Chen, L.; Snyder, G. J., Convergence of electronic bands for high performance bulk thermoelectrics. *Nature* **2011**, *473* (7345), 66-69.
100. Biswas, K.; He, J.; Zhang, Q.; Wang, G.; Uher, C.; Dravid, V. P.; Kanatzidis, M. G., Strained endotaxial nanostructures with high thermoelectric figure of merit. *Nature Chemistry* **2011**, *3* (2), 160-166.
101. Poudel, B.; Hao, Q.; Ma, Y.; Lan, Y.; Minnich, A.; Yu, B.; Yan, X.; Wang, D.; Muto, A.; Vashaee, D.; Chen, X.; Liu, J.; Dresselhaus, M. S.; Chen, G.; Ren, Z., High-Thermoelectric Performance of Nanostructured Bismuth Antimony Telluride Bulk Alloys. *Science* **2008**, *320* (5876), 634-638.
102. Hu, X.; Jood, P.; Ohta, M.; Kunii, M.; Nagase, K.; Nishiate, H.; Kanatzidis, M. G.; Yamamoto, A., Power generation from nanostructured PbTe-based thermoelectrics: comprehensive development from materials to modules. *Energy & Environmental Science* **2016**, *9* (2), 517-529.

103. Zhao, L.-D.; Tan, G.; Hao, S.; He, J.; Pei, Y.; Chi, H.; Wang, H.; Gong, S.; Xu, H.; Dravid, V. P.; Uher, C.; Snyder, G. J.; Wolverton, C.; Kanatzidis, M. G., Ultrahigh power factor and thermoelectric performance in hole-doped single-crystal SnSe. *Science* **2016**, *351* (6269), 141-144.
104. Yang, L.; Chen, Z.-G.; Hong, M.; Han, G.; Zou, J., Enhanced Thermoelectric Performance of Nanostructured Bi₂Te₃ through Significant Phonon Scattering. *ACS Applied Materials & Interfaces* **2015**, *7* (42), 23694-23699.
105. Bathula, S.; Jayasimhadri, M.; Singh, N.; Srivastava, A. K.; Pulikkotil, J.; Dhar, A.; Budhani, R. C., Enhanced thermoelectric figure-of-merit in spark plasma sintered nanostructured n-type SiGe alloys. *Applied Physics Letters* **2012**, *101* (21), 213902.
106. Xiao, Y.; Zhao, L.-D., Charge and phonon transport in PbTe-based thermoelectric materials. *npj Quantum Materials* **2018**, *3* (1), 55.
107. Jiang, B.; Liu, X.; Wang, Q.; Cui, J.; Jia, B.; Zhu, Y.; Feng, J.; Qiu, Y.; Gu, M.; Ge, Z.; He, J., Realizing high-efficiency power generation in low-cost PbS-based thermoelectric materials. *Energy & Environmental Science* **2020**, *13* (2), 579-591.
108. Grant, I. R., III–V Compound Semiconductors: Growth. In *Encyclopedia of Materials: Science and Technology*, Buschow, K. H. J.; Cahn, R. W.; Flemings, M. C.; Ilshner, B.; Kramer, E. J.; Mahajan, S.; Veyssière, P., Eds. Elsevier: Oxford, 2001; pp 1441-1452.
109. Milnes, A. G.; Polyakov, A. Y., Indium arsenide: a semiconductor for high speed and electro-optical devices. *Materials Science and Engineering: B* **1993**, *18* (3), 237-259.
110. Kaiwa, N.; Yamazaki, J.; Matsumoto, T.; Saito, M.; Yamaguchi, S.; Yamamoto, A., Thermoelectric properties and a device based on n-InSb and p-InAs. *Applied Physics Letters* **2007**, *90* (5), 052107.
111. Bowers, R.; Jr., R. W. U.; Bauerle, J. E.; Cornish, A. J., InAs and InSb as Thermoelectric Materials. *Journal of Applied Physics* **1959**, *30* (6), 930-934.
112. Wu, P. M.; Gooth, J.; Zianni, X.; Svensson, S. F.; Gluschke, J. G.; Dick, K. A.; Thelander, C.; Nielsch, K.; Linke, H., Large Thermoelectric Power Factor Enhancement Observed in InAs Nanowires. *Nano Letters* **2013**, *13* (9), 4080-4086.
113. Muthaiah, R.; Garg, J., Strain tuned thermal conductivity reduction in Indium Arsenide (InAs)—A first-principles study. *Computational Materials Science* **2021**, *196*, 110531.
114. Garg, J.; Sellers, I. R., Phonon linewidths in InAs/AlSb superlattices derived from first-principles—application towards quantum well hot carrier solar cells. *Semiconductor Science and Technology* **2020**, *35* (4), 044001.
115. Monkhorst, H. J.; Pack, J. D., Special points for Brillouin-zone integrations. *Physical Review B* **1976**, *13* (12), 5188-5192.
116. Omini, M.; Sparavigna, A., Beyond the isotropic-model approximation in the theory of thermal conductivity. *Physical Review B* **1996**, *53* (14), 9064-9073.
117. Zhou, F.; Moore, A. L.; Bolinsson, J.; Persson, A.; Fröberg, L.; Pettes, M. T.; Kong, H.; Rabenberg, L.; Caroff, P.; Stewart, D. A.; Mingo, N.; Dick, K. A.; Samuelson, L.; Linke, H.; Shi, L., Thermal conductivity of indium arsenide nanowires with wurtzite and zinc blende phases. *Physical Review B* **2011**, *83* (20), 205416.
118. Cheng, Y.; Yang, J.; Jiang, Q.; He, D.; He, J.; Luo, Y.; Zhang, D.; Zhou, Z.; Ren, Y.; Xin, J., New insight into InSb-based thermoelectric materials: from a divorced eutectic design to a remarkably high thermoelectric performance. *Journal of Materials Chemistry A* **2017**, *5* (10), 5163-5170.
119. Wang, K.; Qin, P.; Ge, Z.-H.; Feng, J., Synthesis and thermoelectric properties of InSb alloys by solid reaction. *Materials Letters* **2017**, *209*, 373-375.
120. Du, Z.; Chen, X.; Zhu, J.; Cui, J., Effect of Ga alloying on thermoelectric properties of InSb. *Current Applied Physics* **2018**, *18* (8), 893-897.
121. Rode, D. L., Electron Transport in InSb, InAs, and InP. *Physical Review B* **1971**, *3* (10), 3287-3299.

122. Liu, W.; Tan, X.; Yin, K.; Liu, H.; Tang, X.; Shi, J.; Zhang, Q.; Uher, C., Convergence of Conduction Bands as a Means of Enhancing Thermoelectric Performance of N-Type Mg₂Si(1-x)Sn(x) Solid Solutions. *Physical Review Letters* **2012**, *108* (16), 166601.
123. Poudel, B.; Hao, Q.; Ma, Y.; Lan, Y.; Minnich, A.; Yu, B.; Yan, X.; Wang, D.; Muto, A.; Vashaee, D.; Chen, X.; Liu, J.; Dresselhaus, M. S.; Chen, G.; Ren, Z., High-Thermoelectric Performance of Nanostructured Bismuth Antimony Telluride Bulk Alloys. *Science* **2008**, *320* (5876), 634.
124. Mukherjee, S.; Givan, U.; Senz, S.; de la Mata, M.; Arbiol, J.; Moutanabbir, O., Reduction of Thermal Conductivity in Nanowires by Combined Engineering of Crystal Phase and Isotope Disorder. *Nano Letters* **2018**, *18* (5), 3066-3075.
125. Nakamura, Y., Nanostructure design for drastic reduction of thermal conductivity while preserving high electrical conductivity. *Sci Technol Adv Mater* **2018**, *19* (1), 31-43.
126. Perumal, S.; Roychowdhury, S.; Biswas, K., Reduction of thermal conductivity through nanostructuring enhances the thermoelectric figure of merit in Ge_{1-x}BixTe. *Inorganic Chemistry Frontiers* **2016**, *3* (1), 125-132.
127. Stern, R.; Wang, T.; Carrete, J.; Mingo, N.; Madsen, G. K. H., Influence of point defects on the thermal conductivity in FeSi. *Physical Review B* **2018**, *97* (19), 195201.
128. Ren, G.-K.; Lan, J.-L.; Ventura, K. J.; Tan, X.; Lin, Y.-H.; Nan, C.-W., Contribution of point defects and nano-grains to thermal transport behaviours of oxide-based thermoelectrics. *npj Computational Materials* **2016**, *2* (1), 16023.
129. Muthaiah, R.; Tarannum, F.; Garg, J., Strain tuned low thermal conductivity in Indium Antimonide (InSb) through increase in anharmonic phonon scattering-A first-principles study. *Solid State Communications* **2021**, *334*, 114378.
130. Holland, M. G., Phonon Scattering in Semiconductors From Thermal Conductivity Studies. *Physical Review* **1964**, *134* (2A), A471-A480.
131. Clavel, M.; Goley, P.; Jain, N.; Zhu, Y.; Hudait, M. K., Strain-Engineered Biaxial Tensile Epitaxial Germanium for High-Performance Ge/InGaAs Tunnel Field-Effect Transistors. *IEEE Journal of the Electron Devices Society* **2015**, *3* (3), 184-193.
132. Chen, G., Particularities of Heat Conduction in Nanostructures. *Journal of Nanoparticle Research* **2000**, *2* (2), 199-204.
133. Li, D.; Wu, Y.; Kim, P.; Shi, L.; Yang, P.; Majumdar, A., Thermal conductivity of individual silicon nanowires. *Applied Physics Letters* **2003**, *83* (14), 2934-2936.
134. Liang, L. H.; Li, B., Size-dependent thermal conductivity of nanoscale semiconducting systems. *Physical Review B* **2006**, *73* (15), 153303.
135. Shiomi, J.; Maruyama, S., Non-Fourier heat conduction in a single-walled carbon nanotube: Classical molecular dynamics simulations. *Physical Review B* **2006**, *73* (20), 205420.
136. Muthaiah, R.; Tarannum, F.; Annam, R. S.; Nayal, A. S.; Danayat, S.; Garg, J., Thermal conductivity of hexagonal BC2P – a first-principles study. *RSC Advances* **2020**, *10* (70), 42628-42632.
137. Nayeb Sadeghi, S.; Vaez Allaei, S. M.; Zebarjadi, M.; Esfarjani, K., Ultra-high lattice thermal conductivity and the effect of pressure in superhard hexagonal BC2N. *Journal of Materials Chemistry C* **2020**.
138. Tian, Z.; Esfarjani, K.; Shiomi, J.; Henry, A. S.; Chen, G., On the importance of optical phonons to thermal conductivity in nanostructures. *Applied Physics Letters* **2011**, *99* (5), 053122.
139. Lindsay, L.; Broido, D. A.; Reinecke, T. L., Phonon-isotope scattering and thermal conductivity in materials with a large isotope effect: A first-principles study. *Physical Review B* **2013**, *88* (14), 144306.
140. Mahmood, A.; Sansores, L. E., Band structure and bulk modulus calculations of germanium carbide. *Journal of Materials Research* **2005**, *20* (5), 1101-1106.
141. Ersan, F.; Gökçe, A. G.; Aktürk, E., Point defects in hexagonal germanium carbide monolayer: A first-principles calculation. *Applied Surface Science* **2016**, *389*, 1-6.

142. Muthaiah, R.; Garg, J., First principles investigation of high thermal conductivity in hexagonal germanium carbide (2H-GeC). *arXiv preprint arXiv:2107.04596* **2021**.
143. Protik, N. H.; Katre, A.; Lindsay, L.; Carrete, J.; Mingo, N.; Broido, D., Phonon thermal transport in 2H, 4H and 6H silicon carbide from first principles. *Materials Today Physics* **2017**, *1*, 31-38.
144. Chung, D. H.; Buessem, W. R., The Voigt-Reuss-Hill (VRH) Approximation and the Elastic Moduli of Polycrystalline ZnO, TiO₂ (Rutile), and α -Al₂O₃. *Journal of Applied Physics* **1968**, *39* (6), 2777-2782.
145. Casimir, H. B. G., Note on the conduction of heat in crystals. *Physica* **1938**, *5* (6), 495-500.
146. Meija, J.; Coplen, T. B.; Berglund, M.; Brand, W. A.; Bièvre, P. D.; Gröning, M.; Holden, N. E.; Irrgeher, J.; Loss, R. D.; Walczyk, T.; Prohaska, T., Atomic weights of the elements 2013 (IUPAC Technical Report). *Pure and Applied Chemistry* **2016**, *88* (3), 265-291.
147. Mouhat, F.; Coudert, F.-X., Necessary and sufficient elastic stability conditions in various crystal systems. *Physical Review B* **2014**, *90* (22), 224104.
148. Nuruzzaman, M.; Islam, M.; Alam, A.; Shah, M.; Karim, A. M. M. T., Structural, elastic and electronic properties of 2H- and 4H-SiC. *Int. Journal of Engineering Research and Applications* **2015**, *5*, 48-52.
149. Pizzagalli, L., Stability and mobility of screw dislocations in 4H, 2H and 3C silicon carbide. *Acta Materialia* **2014**, *78*, 236-244.
150. Wei, L.; Kuo, P. K.; Thomas, R. L.; Anthony, T. R.; Banholzer, W. F., Thermal conductivity of isotopically modified single crystal diamond. *Physical Review Letters* **1993**, *70* (24), 3764-3767.
151. Burgemeister, E., Thermal conductivity of natural diamond between 320 and 450 K. *Physica B+ C* **1978**, *93* (2), 165-179.
152. Broido, D. A.; Lindsay, L.; Ward, A., Thermal conductivity of diamond under extreme pressure: A first-principles study. *Physical Review B* **2012**, *86* (11), 115203.
153. Chakraborty, P.; Xiong, G.; Cao, L.; Wang, Y., Lattice thermal transport in superhard hexagonal diamond and wurtzite boron nitride: A comparative study with cubic diamond and cubic boron nitride. *Carbon* **2018**, *139*, 85-93.
154. Muthaiah, R.; Garg, J., Strain tuned high thermal conductivity in boron phosphide at nanometer length scales – a first-principles study. *Physical Chemistry Chemical Physics* **2020**, *22* (36), 20914-20921.
155. Yuan, C.; Li, J.; Lindsay, L.; Cherns, D.; Pomeroy, J. W.; Liu, S.; Edgar, J. H.; Kuball, M., Modulating the thermal conductivity in hexagonal boron nitride via controlled boron isotope concentration. *Communications Physics* **2019**, *2* (1), 43.
156. Shafique, A.; Shin, Y.-H., Ultrahigh and anisotropic thermal transport in the hybridized monolayer (BC₂N) of boron nitride and graphene: a first-principles study. *Physical Chemistry Chemical Physics* **2019**, *21* (31), 17306-17313.
157. Lindsay, L.; Broido, D. A.; Reinecke, T. L., First-Principles Determination of Ultrahigh Thermal Conductivity of Boron Arsenide: A Competitor for Diamond? *Physical Review Letters* **2013**, *111* (2), 025901.
158. Lindsay, L.; Broido, D. A.; Reinecke, T. L., Ab initio thermal transport in compound semiconductors. *Physical Review B* **2013**, *87* (16), 165201.
159. Zheng, Q.; Li, S.; Li, C.; Lv, Y.; Liu, X.; Huang, P. Y.; Broido, D. A.; Lv, B.; Cahill, D. G., High Thermal Conductivity in Isotopically Enriched Cubic Boron Phosphide. *Advanced Functional Materials* **2018**, *28* (43), 1805116.
160. Mortazavi, B.; Shahrokhi, M.; Raeisi, M.; Zhuang, X.; Pereira, L. F. C.; Rabczuk, T., Outstanding strength, optical characteristics and thermal conductivity of graphene-like BC₃ and BC₆N semiconductors. *Carbon* **2019**, *149*, 733-742.
161. Muthaiah, R.; Garg, J., Ultrahigh thermal conductivity in hexagonal BC₆N-An efficient material for nanoscale thermal management-A first principles study. *arXiv preprint arXiv:2107.04079* **2021**.

162. Meija, J.; Coplen, T. B.; Berglund, M.; Brand, W. A.; De Bièvre, P.; Gröning, M.; Holden, N. E.; Irrgeher, J.; Loss, R. D.; Walczyk, T.; Prohaska, T., Atomic weights of the elements 2013 (IUPAC Technical Report). *Pure and Applied Chemistry* **2016**, *88* (3), 265-291.
163. Ward, A.; Broido, D. A., Intrinsic phonon relaxation times from first-principles studies of the thermal conductivities of Si and Ge. *Physical Review B* **2010**, *81* (8), 085205.
164. Esfarjani, K.; Chen, G.; Stokes, H. T., Heat transport in silicon from first-principles calculations. *Physical Review B* **2011**, *84* (8), 085204.
165. Senturk, A. E.; Oktem, A. S.; Konukman, A. E. S., Thermal conductivity and mechanical properties of graphene-like BC₂, BC₃ and B₄C₃. *Molecular Simulation* **2020**, *46* (12), 879-888.
166. Solozhenko, V. L.; Godec, Y. L., A Hunt for Ultrahard Materials. *Journal of Applied Physics* **2019**, *126* (23), 230401.
167. Chang, H.; Tu, K.; Zhang, X.; Zhao, J.; Zhou, X.; Zhang, H., B₄C₃ Monolayer with Impressive Electronic, Optical, and Mechanical Properties: A Potential Metal-Free Photocatalyst for CO₂ Reduction under Visible Light. *The Journal of Physical Chemistry C* **2019**, *123* (41), 25091-25101.
168. Guo, X.; He, J.; Xu, B.; Liu, Z.; Yu, D.; Tian, Y., First-Principles Investigation of Dense B₄C₃. *The Journal of Physical Chemistry C* **2007**, *111* (37), 13679-13683.
169. Gao, F.; Klug, D. D.; Tse, J. S., Theoretical study of new superhard materials: B₄C₃. *Journal of Applied Physics* **2007**, *102* (8), 084311.
170. Zhao, W. J.; Wang, Y. X., Mechanical properties of superhard diamondlike BC₅. *Solid State Communications* **2011**, *151* (6), 478-481.
171. Lazar, P.; Podloucky, R., Mechanical properties of superhard BC₅. *Applied Physics Letters* **2009**, *94* (25), 251904.
172. Muthaiah, R.; Garg, J.; Arafin, S., Ultrahard BC₅--an efficient nanoscale heat conductor through dominant contribution of optical phonons. *arXiv preprint arXiv:2107.04083* **2021**.
173. Calandra, M.; Mauri, F., High- T_c Superconductivity in Superhard Diamondlike BC_5 . *Physical Review Letters* **2008**, *101* (1), 016401.
174. Jain, A.; McGaughey, A. J. H., Effect of exchange–correlation on first-principles-driven lattice thermal conductivity predictions of crystalline silicon. *Computational Materials Science* **2015**, *110*, 115-120.
175. Valentin, A.; Sée, J.; Galdin-Retailleau, S.; Dollfus, P., Study of phonon modes in silicon nanocrystals using the adiabatic bond charge model. *Journal of Physics: Condensed Matter* **2008**, *20* (14), 145213.
176. Alp, I. O.; Ciftci, Y. O., Physical Properties of Superhard Diamond-Like BC₅ from a First-Principles Study. *Journal of Electronic Materials* **2018**, *47* (1), 272-284.
177. Olson, J. R.; Pohl, R. O.; Vandersande, J. W.; Zoltan, A.; Anthony, T. R.; Banholzer, W. F., Thermal conductivity of diamond between 170 and 1200 K and the isotope effect. *Physical Review B* **1993**, *47* (22), 14850-14856.
178. Onn, D. G.; Witek, A.; Qiu, Y. Z.; Anthony, T. R.; Banholzer, W. F., Some aspects of the thermal conductivity of isotopically enriched diamond single crystals. *Physical Review Letters* **1992**, *68* (18), 2806-2809.
179. Ward, A.; Broido, D. A.; Stewart, D. A.; Deinzer, G., Ab initio theory of the lattice thermal conductivity in diamond. *Physical Review B* **2009**, *80* (12), 125203.
180. Seol, J. H.; Jo, I.; Moore, A. L.; Lindsay, L.; Aitken, Z. H.; Pettes, M. T.; Li, X.; Yao, Z.; Huang, R.; Broido, D.; Mingo, N.; Ruoff, R. S.; Shi, L., Two-Dimensional Phonon Transport in Supported Graphene. *Science* **2010**, *328* (5975), 213-216.
181. Lindsay, L.; Broido, D. A.; Mingo, N., Flexural phonons and thermal transport in graphene. *Physical Review B* **2010**, *82* (11), 115427.
182. Nika, D.; Pokatilov, E.; Askerov, A.; Balandin, A., Phonon Thermal Conduction in Graphene. **2008**.

183. Balandin, A.; Nika, D.; Pokatilov, E.; Askerov, A., Comment on 'First principles calculation of lattice thermal conductivity in mono- and bi-layer graphene' (arXiv:0902.0642). **2009**.
184. Chen, K.; Song, B.; Ravichandran, N. K.; Zheng, Q.; Chen, X.; Lee, H.; Sun, H.; Li, S.; Udalamatta Gamage, G. A. G.; Tian, F.; Ding, Z.; Song, Q.; Rai, A.; Wu, H.; Koirala, P.; Schmidt, A. J.; Watanabe, K.; Lv, B.; Ren, Z.; Shi, L.; Cahill, D. G.; Taniguchi, T.; Broido, D.; Chen, G., Ultrahigh thermal conductivity in isotope-enriched cubic boron nitride. *Science* **2020**, *367* (6477), 555-559.
185. Tian, F.; Song, B.; Chen, X.; Ravichandran, N. K.; Lv, Y.; Chen, K.; Sullivan, S.; Kim, J.; Zhou, Y.; Liu, T.-H.; Goni, M.; Ding, Z.; Sun, J.; Udalamatta Gamage, G. A. G.; Sun, H.; Ziyadee, H.; Huyan, S.; Deng, L.; Zhou, J.; Schmidt, A. J.; Chen, S.; Chu, C.-W.; Huang, P. Y.; Broido, D.; Shi, L.; Chen, G.; Ren, Z., Unusual high thermal conductivity in boron arsenide bulk crystals. *Science* **2018**, *361* (6402), 582-585.
186. Muthaiah, R.; Tarannum, F.; Annam, R. S.; Nayal, A. S.; Danayat, S.; Garg, J., Thermal conductivity of hexagonal BC₂P—a first-principles study. *RSC Advances* **2020**, *10* (70), 42628-42632.
187. Ceperley, D. M.; Alder, B. J., Ground State of the Electron Gas by a Stochastic Method. *Physical Review Letters* **1980**, *45* (7), 566-569.
188. Etxebarria, I.; Perez-Mato, J. M.; Madariaga, G., Lattice dynamics, structural stability, and phase transitions in incommensurate and commensurate $\sqrt{2}\sqrt{A}\times\sqrt{2}\sqrt{B}\times\sqrt{4}\sqrt{C}$ materials. *Physical Review B* **1992**, *46* (5), 2764-2774.
189. Vanhellemont, J.; Swarnakar, A. K.; Van der Biest, O., Temperature Dependent Young's Modulus of Si and Ge. *ECS Transactions* **2014**, *64* (11), 283-292.
190. SCHREIBER, E.; SOGA, N., Elastic Constants of Silicon Carbide. *Journal of the American Ceramic Society* **1966**, *49* (6), 342-342.
191. Baliga, B. J., 1 - Introduction. In *Wide Bandgap Semiconductor Power Devices*, Baliga, B. J., Ed. Woodhead Publishing: 2019; pp 1-19.
192. di Forte-Poisson, M. A.; Magis, M.; Tordjmann, M.; di Persio, J., Chapter 5 - MOCVD Growth of Group III Nitrides for High-power, High-frequency Applications. In *Optoelectronic Devices: III Nitrides*, Razeghi, M.; Henini, M., Eds. Elsevier: Oxford, 2005; pp 69-94.
193. Millán, J.; Godignon, P. In *Wide Band Gap power semiconductor devices*, 2013 Spanish Conference on Electron Devices, 12-14 Feb. 2013; 2013; pp 293-296.
194. Xiao, Y.; Zhao, L.-D., Seeking new, highly effective thermoelectrics. *Science* **2020**, *367* (6483), 1196.
195. Kucukgok, B. THERMOELECTRIC PHENOMENA FOR WASTE HEAT HARVESTING USING WIDE BANDGAP SEMICONDUCTORS. The University of North Carolina at Charlotte, 2015.
196. Kucukgok, B.; He, Q.; Carlson, A.; Melton, A. G.; Ferguson, I. T.; Lu, N., Investigation of Wide Bandgap Semiconductors for Thermoelectric Applications. *MRS Proceedings* **2013**, *1490*, 161-166.
197. Liu, M.-L.; Huang, F.-Q.; Chen, L.-D.; Chen, I.-W., A wide-band-gap p-type thermoelectric material based on quaternary chalcogenides of Cu₂ZnSnQ₄ (Q=S,Se). *Applied Physics Letters* **2009**, *94* (20), 202103.
198. Drief, F.; Tadjer, A.; Mesri, D.; Aourag, H., First principles study of structural, electronic, elastic and optical properties of MgS, MgSe and MgTe. *Catalysis Today* **2004**, *89* (3), 343-355.
199. Sajjad, M.; Zhang, H. X.; Noor, N. A.; Alay-e-Abbas, S. M.; Younas, M.; Abid, M.; Shaukat, A., Theoretical Investigation of Structural, Electronic, and Magnetic Properties of V-Doped MgSe and MgTe Semiconductors. *Journal of Superconductivity and Novel Magnetism* **2014**, *27* (10), 2327-2336.
200. Rached, D.; Benkhattou, N.; Soudini, B.; Abbar, B.; Sekkal, N.; Driz, M., Electronic structure calculation of magnesium chalcogenides MgS and MgSe. *physica status solidi (B)* **2003**, *240* (3), 565-573.
201. Lee, S.-G.; Chang, K. J., First-principles study of the structural properties of MgS-, MgSe-, ZnS-, and ZnSe-based superlattices. *Physical Review B* **1995**, *52* (3), 1918-1925.
202. Parker, S. G.; Reinberg, A. R.; Pinnell, J. E.; Holton, W. C., Preparation and Properties of Mg_xZn_{1-x}Te. *Journal of The Electrochemical Society* **1971**, *118* (6), 979.
203. Kuhn, A.; Chevy, A.; Naud, M.-J., Preparation and some physical properties of magnesium telluride single crystals. *Journal of Crystal Growth* **1971**, *9*, 263-265.

204. Duman, S.; Bağcı, S.; Tütüncü, H. M.; Srivastava, G. P., First-principles studies of ground-state and dynamical properties of MgS, MgSe, and MgTe in the rocksalt, zinc blende, wurtzite, and nickel arsenide phases. *Physical Review B* **2006**, *73* (20), 205201.
205. Gökoğlu, G., First principles vibrational dynamics of magnesium telluride. *Journal of Physics and Chemistry of Solids* **2010**, *71* (9), 1388-1392.
206. Zhang, F.; Chen, C.; Yao, H.; Bai, F.; Yin, L.; Li, X.; Li, S.; Xue, W.; Wang, Y.; Cao, F.; Liu, X.; Sui, J.; Zhang, Q., High-Performance N-type Mg₃Sb₂ towards Thermoelectric Application near Room Temperature. *Advanced Functional Materials* **2020**, *30* (5), 1906143.
207. Li, J.; Zheng, S.; Fang, T.; Yue, L.; Zhang, S.; Lu, G., Computational prediction of a high ZT of n-type Mg₃Sb₂-based compounds with isotropic thermoelectric conduction performance. *Physical Chemistry Chemical Physics* **2018**, *20* (11), 7686-7693.
208. Dmitriev, A. V., High doping effect on the thermoelectric properties of p-type lead telluride. *Journal of Applied Physics* **2018**, *123* (16), 165707.
209. Zhang, J.; Song, L.; Pedersen, S. H.; Yin, H.; Hung, L. T.; Iversen, B. B., Discovery of high-performance low-cost n-type Mg₃Sb₂-based thermoelectric materials with multi-valley conduction bands. *Nature Communications* **2017**, *8* (1), 13901.
210. Dughaish, Z. H., Lead telluride as a thermoelectric material for thermoelectric power generation. *Physica B: Condensed Matter* **2002**, *322* (1), 205-223.
211. Waag, A.; Heinke, H.; Scholl, S.; Becker, C. R.; Landwehr, G., Growth of MgTe and Cd_{1-x}Mg_xTe thin films by molecular beam epitaxy. *Journal of Crystal Growth* **1993**, *131* (3), 607-611.
212. Tarannum, F.; Muthaiah, R.; Annam, R. S.; Gu, T.; Garg, J., Effect of Alignment on Enhancement of Thermal Conductivity of Polyethylene–Graphene Nanocomposites and Comparison with Effective Medium Theory. *Nanomaterials* **2020**, *10* (7), 1291.
213. Oh, S. K.; Lundh, J. S.; Shervin, S.; Chatterjee, B.; Lee, D. K.; Choi, S.; Kwak, J. S.; Ryou, J.-H., Thermal Management and Characterization of High-Power Wide-Bandgap Semiconductor Electronic and Photonic Devices in Automotive Applications. *Journal of Electronic Packaging* **2019**, *141* (2).
214. Thakare, J. G.; Pandey, C.; Mahapatra, M. M.; Mulik, R. S., Thermal Barrier Coatings—A State of the Art Review. *Metals and Materials International* **2020**.
215. Clarke, D. R.; Phillpot, S. R., Thermal barrier coating materials. *Materials Today* **2005**, *8* (6), 22-29.
216. Padture, N. P.; Gell, M.; Jordan, E. H., Thermal Barrier Coatings for Gas-Turbine Engine Applications. *Science* **2002**, *296* (5566), 280-284.
217. Başol, B.; McCandless, B., Brief review of cadmium telluride-based photovoltaic technologies. *Journal of Photonics for Energy* **2014**, *4* (1), 040996.
218. Saadah, M. In *Thermal Management of Solar Cells*, 2013.
219. Zweibel, K., The Impact of Tellurium Supply on Cadmium Telluride Photovoltaics. *Science* **2010**, *328* (5979), 699-701.
220. Muthaiah, R.; Garg, J., Thermal conductivity of magnesium selenide (MgSe)—A first principles study. *Computational Materials Science* **2021**, *198*, 110679.
221. Muthaiah, R.; Garg, J., First principles investigation of thermal conductivity in Magnesium Selenide (MgSe) with different crystalline phase. *arXiv preprint arXiv:2101.12647* **2021**.
222. Chakrabarti, A., Role of NiAs phase in pressure-induced structural phase transitions in IIA-VI chalcogenides. *Physical Review B* **2000**, *62* (3), 1806-1814.
223. Van Camp, P. E.; Van Doren, V. E.; Martins, J. L., High-pressure phases of magnesium selenide and magnesium telluride. *Physical Review B* **1997**, *55* (2), 775-779.
224. Okuyama, H.; Nakano, K.; Miyajima, T.; Akimoto, K., Epitaxial growth of ZnMgSSe on GaAs substrate by molecular beam epitaxy. *Journal of Crystal Growth* **1992**, *117* (1), 139-143.
225. Srivastava, G. P., The physics of phonons. **2019**.

226. Coplen, T. B., Atomic Weights of the Elements 1995. *Journal of Physical and Chemical Reference Data* **1997**, 26 (5), 1239-1253.
227. Akinlami, J. O., Electronic, structural and paramagnetic properties of magnesium telluride. *Semiconductor physics, quantum electronics and optoelectronics* **2019**, 22, 5-10.
228. Condrón, C. L.; Kauzlarich, S. M.; Gascoin, F.; Snyder, G. J., Thermoelectric properties and microstructure of Mg₃Sb₂. *Journal of Solid State Chemistry* **2006**, 179 (8), 2252-2257.
229. Khusainov, A. K., Cadmium telluride detectors with thermoelectric cooling. *Nuclear Instruments and Methods in Physics Research Section A: Accelerators, Spectrometers, Detectors and Associated Equipment* **1992**, 322 (3), 335-340.
230. Hossain, M. S.; Islam, R.; Shahjahan, M.; Khan, K. A., Studies on the thermoelectric effect in semiconducting ZnTe thin films. *Journal of Materials Science: Materials in Electronics* **2008**, 19 (11), 1114-1121.
231. Bhaskar, A.; Pai, Y.-H.; Wu, W.-M.; Chang, C.-L.; Liu, C.-J., Low thermal conductivity and enhanced thermoelectric performance of nanostructured Al-doped ZnTe. *Ceramics International* **2016**, 42 (1, Part B), 1070-1076.
232. Bar-Cohen, A.; Wang, P.; Rahim, E., Thermal management of high heat flux nanoelectronic chips. *Microgravity Science and Technology* **2007**, 19 (3), 48-52.
233. Anandan, S. S.; Ramalingam, V. In *Thermal management of electronics: A review of literature*, 2008.
234. Yang, B.; Li, S.; Li, X.; Liu, Z.; Zhong, H.; Feng, S., Ultralow thermal conductivity and enhanced thermoelectric properties of SnTe based alloys prepared by melt spinning technique. *Journal of Alloys and Compounds* **2020**, 837, 155568.
235. Malhotra, A.; Maldovan, M., Phononic pathways towards rational design of nanowire heat conduction. *Nanotechnology* **2019**, 30 (37), 372002.
236. Hori, T.; Shiomi, J., Tuning phonon transport spectrum for better thermoelectric materials. *Sci Technol Adv Mater* **2019**, 20 (1), 10-25.
237. Chauhan, A.; Tyagi, V. V.; Anand, S., Futuristic approach for thermal management in solar PV/thermal systems with possible applications. *Energy Conversion and Management* **2018**, 163, 314-354.
238. Yanagisawa, S.; Tashiro, M.; Anzai, S., Crystal structure of magnesium ditelluride. *Journal of Inorganic and Nuclear Chemistry* **1969**, 31 (4), 943-946.
239. Klemm, W.; Wahl, K., Notiz Über das Magnesiumtellurid. *Zeitschrift für anorganische und allgemeine Chemie* **1951**, 266 (6), 289-292.
240. Muthaiah, R.; Garg, J., Thermal conductivity of magnesium telluride (MgTe) - A first principles study. *Solid State Communications* **2021**, 337, 114414.
241. Bar-Cohen, A. In *Thermal management of on-chip hot spots and 3D chip stacks*, 2009 IEEE International Conference on Microwaves, Communications, Antennas and Electronics Systems, 9-11 Nov. 2009; 2009; pp 1-8.
242. Fugallo, G.; Cepellotti, A.; Paulatto, L.; Lazzeri, M.; Marzari, N.; Mauri, F., Thermal Conductivity of Graphene and Graphite: Collective Excitations and Mean Free Paths. *Nano Letters* **2014**, 14 (11), 6109-6114.
243. Ghosh, S.; Calizo, I.; Teweldebrhan, D.; Pokatilov, E. P.; Nika, D. L.; Balandin, A. A.; Bao, W.; Miao, F.; Lau, C. N., Extremely high thermal conductivity of graphene: Prospects for thermal management applications in nanoelectronic circuits. *Applied Physics Letters* **2008**, 92 (15), 151911.
244. Bonini, N.; Garg, J.; Marzari, N., Acoustic Phonon Lifetimes and Thermal Transport in Free-Standing and Strained Graphene. *Nano Letters* **2012**, 12 (6), 2673-2678.
245. Li, S.; Chen, Y., Thermal transport and anharmonic phonons in strained monolayer hexagonal boron nitride. *Scientific Reports* **2017**, 7 (1), 43956.

246. Cai, Q.; Scullion, D.; Gan, W.; Falin, A.; Zhang, S.; Watanabe, K.; Taniguchi, T.; Chen, Y.; Santos, E. J. G.; Li, L. H., High thermal conductivity of high-quality monolayer boron nitride and its thermal expansion. *Science Advances* **2019**, *5* (6), eaav0129.
247. Shi, C.; Luo, X., Characterization of lattice thermal transport in two-dimensional BAs, BP, and BSb: A first-principles study. *arXiv preprint arXiv:1811.05597* **2018**.
248. Qin, Z.; Qin, G.; Zuo, X.; Xiong, Z.; Hu, M., Orbitaly driven low thermal conductivity of monolayer gallium nitride (GaN) with planar honeycomb structure: a comparative study. *Nanoscale* **2017**, *9* (12), 4295-4309.
249. Wang, H.; Yu, L.; Xu, J.; Wei, D.; Qin, G.; Yao, Y.; Hu, M., Intrinsically low lattice thermal conductivity of monolayer hexagonal aluminum nitride (h-AlN) from first-principles: A comparative study with graphene. *International Journal of Thermal Sciences* **2021**, *162*, 106772.
250. Guo, S.-D.; Dong, J.; Liu, J.-T., Nonmonotonic strain dependence of lattice thermal conductivity in monolayer SiC: a first-principles study. *Physical Chemistry Chemical Physics* **2018**, *20* (34), 22038-22046.
251. Mariani, E.; von Oppen, F., Flexural Phonons in Free-Standing Graphene. *Physical Review Letters* **2008**, *100* (7), 076801.
252. Zhang, A.-X.; Liu, J.-T.; Guo, S.-D.; Li, H.-C., Strain effects on phonon transport in antimonene investigated using a first-principles study. *Physical Chemistry Chemical Physics* **2017**, *19* (22), 14520-14526.
253. Guo, S.-D.; Dong, J., Biaxial tensile strain tuned up-and-down behavior on lattice thermal conductivity in β -AsP monolayer. *Journal of Physics D: Applied Physics* **2018**, *51* (26), 265307.
254. Lindsay, L.; Broido, D.; Reinecke, T., First-principles determination of ultrahigh thermal conductivity of boron arsenide: A competitor for diamond? *Physical review letters* **2013**, *111* (2), 025901.
255. Broido, D.; Lindsay, L.; Reinecke, T., Ab initio study of the unusual thermal transport properties of boron arsenide and related materials. *Physical Review B* **2013**, *88* (21), 214303.
256. Andrew, R. C.; Mapasha, R. E.; Ukpog, A. M.; Chetty, N., Mechanical properties of graphene and boronitrene. *Physical Review B* **2012**, *85* (12), 125428.
257. Peng, Q.; Liang, C.; Ji, W.; De, S., A first-principles study of the mechanical properties of g-GeC. *Mechanics of Materials* **2013**, *64*, 135-141.